



PERGAMON

Available online at www.sciencedirect.com

SCIENCE @ DIRECT®

PROGRESS IN
AEROSPACE
SCIENCES

Progress in Aerospace Sciences 39 (2003) 185–248

www.elsevier.com/locate/paerosci

The unsteady aerodynamics of slender wings and aircraft undergoing large amplitude maneuvers

Robert C. Nelson*, Alain Pelletier

Department of Aerospace and Mechanical Engineering, Hessert Center for Aerospace Research, University of Notre Dame, Notre Dame, IN 46556, USA

Abstract

Aircraft that maneuver through large angles of attack will experience large regions of flow separation over the wing and fuselage. The separated flow field is characterized by unsteadiness and strong vortical flow structures that can interact with various components of the aircraft. These complicated flow interactions are the primary cause of most flight dynamic instabilities, airload nonlinearities and flow field time lags.

The aerodynamic and the vortical flow structure over simple delta wings undergoing either a pitching or rolling motion is presented. This article reviews experimental information on the flow structure over delta wings and complete aircraft configurations. First, the flow structure of leading-edge vortices and their influence on delta wing aerodynamics for stationary models is presented. This is followed by a discussion of the effect of large amplitude motion on the vortex structure and aerodynamic characteristic of pitching and rolling delta wings. The relationship between the flow structure and the unsteady airloads is reviewed.

The unsteady motion of the delta wing results in a modification of the flow field. Delays in flow separation, vortex formation, vortex position and the onset of vortex breakdown are all affected by the model motion. These flow changes cause a corresponding modification in the aerodynamic loads. Data is presented which shows the importance of flow field hysteresis in either vortex position or breakdown and the influence on the aerodynamic characteristics of a maneuvering delta wing.

The free-to-roll motion of a double-delta wing is also presented. The complicated flow structure over a double-delta wing gives rise to damped, chaotic and wing rock motions as the angle of attack is increased. The concept of a critical state is discussed and it is shown that crossing a critical state produces large transients in the dynamic airloads.

Next, several aircraft configurations are examined to show the importance of unsteady aerodynamics on the flight dynamics of aircraft maneuvering at large angles of attack. The rolling characteristics of the F-18 and X-31 configurations are examined. The influence of the vortical flow structure on the rolling motion is established.

Finally, a brief discussion of nonlinear aerodynamic modeling is presented. The importance of critical states and the transient aerodynamics associated with crossing a critical state are examined.

© 2003 Elsevier Science Ltd. All rights reserved.

Abbreviations: AUTO, autorotation; PCS, predicted canard schedule; WDO, weakly divergent oscillation; WR, wing rock; SCS, simulated canard schedule; SDO, strongly divergent oscillation.

*Corresponding author.

E-mail addresses: robert.c.nelson1@nd.edu (R.C. Nelson), apelletti@alumni.nd.edu (A. Pelletier).

2.	Leading-edge vortical flows on static delta wings	193
2.1.	Flow features of leading-edge vortices	194
2.1.1.	Vorticity and circulation	196
2.1.2.	Vortex strength correlation	197
2.1.3.	Vortex breakdown	198
2.1.4.	Pressure gradient	201
2.1.5.	Pressure fields after breakdown	203
2.2.	Aerodynamic characteristics	204
2.3.	Reynolds number effects	207
2.4.	Mach number effects	207
2.5.	Summary	209
3.	Unsteady slender wing aerodynamics	209
3.1.	Aerodynamics of a pitching delta wing	210
3.1.1.	Vortex breakdown	210
3.1.2.	Summary	212
3.2.	Wing rock motion of slender delta wings	212
3.2.1.	Plain delta wing	212
3.2.2.	Vortex breakdown results	217
3.3.	Computational model of wing rock	219
3.3.1.	Summary	225
3.4.	Double-delta wing	225
3.4.1.	No critical state encounter	228
3.4.2.	Critical state encounters	228
3.4.3.	Summary	230
3.5.	Remarks	230
4.	Aircraft dynamic characteristics and unsteady aerodynamics	232
4.1.	F-18 HARV	232
4.2.	X-31 Aircraft	237
4.3.	Summary	241
5.	Nonlinear aerodynamic modeling	242
5.1.	Nonlinear indicial response model	242
5.2.	Summary	243
6.	Concluding remarks	243
	Acknowledgements	244
	References	244

1. Introduction

The desire for increased speed, maneuverability and efficiency has dominated the evolution of military aircraft. These goals have resulted in aircraft designs that incorporate swept wings and highly swept wing leading-edge extensions (LEX). This trend has currently reached a point where typical flight envelopes encompass very high angles of attack; and it is in the high angle-of-attack regime that swept wings have unique characteristics. High angle-of-attack flight is frequently encountered during landing and takeoff phases of a flight, and during combat maneuvering. Maneuvers such as nose pointing and velocity vector turning involve high angles of attack and successful execution

would necessitate the ability to anticipate the dynamic reaction of the airloads to the maneuver. These types of maneuvers are typically referred to as “supermaneuverability” [1], a term that implies control of an airframe at and beyond stall angles. The Sukhoi 27 fighter made supermaneuverability a hot topic when it performed the “Cobra Maneuver” at the Paris airshow in 1989 [2]. This low speed maneuver involves pitching the aircraft to a very high angle of attack, of the order of 100° , and bringing it back down to a level flight in a matter of seconds, without any appreciable change in the altitude. The ability to rapidly change “maneuver state” is a measure of the “agility” of the airplane. Being able to perform the Cobra Maneuver is a sign of agility, but not a prerequisite.

With the continued emphasis on extending aircraft flight regimes, an improved understanding of the influence of unsteady motions on slender forebodies and swept wing performance is essential in order to predict the flight dynamic behavior of modern high performance aircraft. The flow field surrounding slender aircraft at large angles of incidence is dominated by the vortices generated on the forebody, leading-edge extensions, wing and control surfaces. Fig. 1 is a sketch illustrating the flow field surrounding a fighter aircraft at large angles of attack. The leeward wake structure can be extremely complicated due to the interactions between the various vortices. The aerodynamic forces created by such complicated flows are nonlinearly related to the instantaneous angle of attack, sideslip angle or roll angle, as well as their rates of change and furthermore are likely to depend on the history of these quantities. To understand and predict the motion of aircraft in this nonlinear region, new mathematical formulations for the aerodynamic models must be developed and an improved understanding of the relationship between the separated flow field and the aerodynamic loads needs to be established. For small changes in the states of an aircraft, linear theory is used with the concept of constant stability derivatives to predict the motion. When the motion involves large angles of attack and separated flows, the concept of constant stability derivatives can no longer be used and there are discontinuities, hysteresis and strong dynamic cross-coupling effects between the longitudinal and lateral/directional modes of motion [3–5]. Table 1 indicates major differences between low angle-of-attack and high angle-of-attack flight regimes.

The unsteady motion of a forebody or delta wing results in a modification of the flow field in response to the maneuver. The model motion can result in delays of flow separation and vortex formation at low angles of attack, and changes in vortex location at higher angles

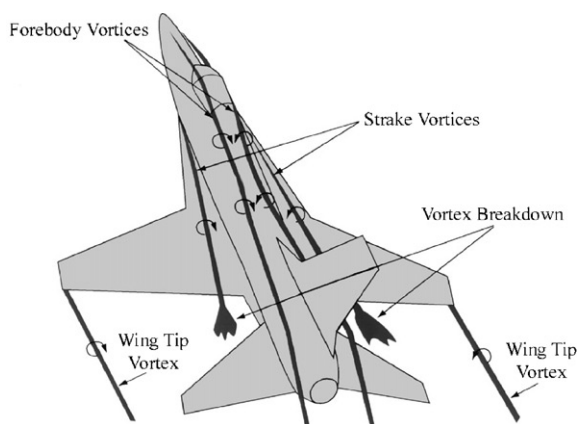


Fig. 1. Sketch of separated flow field dominated by vortical flow structures.

of attack. At high angles of attack, the vortices can undergo a transition process known as vortex breakdown. When vortex breakdown occurs over a lifting surface, the aerodynamic loading can change abruptly. More dramatic changes in loading occur when breakdown reaches the apex of the lifting surface and the flow becomes fully separated. The nonlinear lift created by the vortex is reduced in the region aft of vortex breakdown [7–12]. This leads to changes in both the longitudinal and lateral aerodynamic forces and moments, and in the stability derivatives [13].

Much of what is known about the flow structure surrounding a maneuvering aircraft comes from studies of simple aerodynamic shapes such as delta wings and forebodies undergoing large amplitude motions. Unsteady swept-wing aerodynamics at very high angles of attack is characterized by flow hysteresis; while for ranges of incidence where there is no vortex breakdown, hysteresis effects are not as pronounced. For a pitching wing, it is possible to delay the detrimental effects of breakdown. A substantial overshoot in the aerodynamic forces is typically seen for oscillatory or transient pitching maneuvers. During oscillatory or periodic motions, a delay occurs in the positions of the vortex core and the vortex breakdown relative to the static locations. Due to this hysteresis in the flow field, there is a corresponding modification of the aerodynamic loads on the delta wing. Similar features have also been noted on slender forebody shapes. The location of vortex breakdown on delta wings can be controlled by various blowing techniques [14–22]. For instance, Mitchell et al. [23] showed that asymmetric blowing along the surface on the leeward side of a delta wing near the apex affects vortex breakdown. On the side of the wing with blowing, vortex breakdown was delayed, while the vortex breakdown on the other side of the wing was not affected. This was observed for several blowing rates. For symmetric blowing, both vortices exhibited a delay in vortex breakdown location.

Forebody vortex manipulation to provide aerodynamic control at large angles of attack has been studied extensively [24–29]. In most of these studies, the forebody vortices are manipulated using flow control schemes such as suction or blowing to control the asymmetry of the vortices. In addition to blowing and suction, various mechanical devices have also been investigated. For example, deployable forebody strakes have been successfully demonstrated to be effective in providing yaw control at large angles of attack. A detailed review of forebody vortex control is presented by Malcolm [24].

1.1. Flight dynamic phenomena

Fighter aircraft maneuvering at high subsonic or transonic speeds can experience uncommanded nonlinear

Table 1
Interest in dynamic derivatives [6]

	Low α	High α
Flow	Mainly linear, often well known	Strong nonlinear effects (separation, transition vortex shedding, etc.)
Analytical prediction of dynamic derivatives	Easy (linear potential methods and various approximations often acceptable) Small (x)	Very difficult (highly nonlinear, often speculative, approximations risky)
Magnitude of dynamic derivatives		Sometimes large, varying sign ($\pm 100x$)
Variation of dynamic derivatives with α	Small	Sometimes very rapid
Effect of dynamic derivatives on flight trajectory and on stability and control	Insignificant or at least constant and well known	Sometimes very large, may often be significant
Interest in dynamic derivatives	Low	High

dynamic behavior involving separated flows and time-dependent effects. Flow separation and unsteady aerodynamics are the underlying causes of unwanted flight dynamic behavior that can limit the operational capability of modern fighter aircraft. In addition to limiting the maneuvering capability of the aircraft, flow separation can lead to flight dynamic phenomena that can compromise flight safety. Flight dynamic phenomena such as wing rock, wing drop, heavy wing, nose slice, and buffet may limit the maneuvering capability of an aircraft. Unfortunately, it is not possible to predict the onset and severity of these phenomena early in the design phase. Therefore, most flight dynamic problems are only discovered during flight testing. In most cases when one or more phenomena become an issue during flight-testing, the designer is placed in a position of having to come up with a quick fix to prevent delays in production or a possible program cancellation. The “quick fix approach” tends to be a cut and try procedure that may provide a solution to the problem at hand without providing any understanding of the flow physics associated with such phenomena. In general, this quick fix solution also results in a degradation of the vehicle’s performance.

1.1.1. Wing rock

One of the most common dynamic phenomena experienced by slender wing aircraft flying at high angles of attack is the phenomenon known as wing rock. Wing rock is a complicated motion that typically affects several degrees of freedom simultaneously; however, as the name implies, the primary motion is an oscillation in roll. At some critical angle of attack, a roll oscillation starts to grow in amplitude until it reaches a maximum amplitude, at which time the airplane continues to rock back and forth. The rolling motion is self-induced and represents a classic limit cycle behavior. The onset of wing rock is often associated with a loss of damping in roll at high angles of attack [5].

Aircraft most susceptible to this oscillatory phenomenon typically have highly swept planforms and/or long slender forebodies that produce vortical flows during excursions into the high angle-of-attack regime. The wing rock motion arises from the unsteady behavior of the vortical flow fields associated with these planforms, coupled with the rolling degree-of-freedom of the aircraft. The unsteady loads created by the flow field produce a rolling oscillation that exhibits the classic limit cycle behavior. The motion can be quite complex and, in many cases, is the result of the coupling of several degrees of freedom.

There are, however, cases where the motion is primarily a rolling motion. The wing rock motion can adversely affect the maneuvering envelope of combat fighter aircraft, and limit the approach angles of attack of commercial aircraft configurations, such as the high-speed civil transport. The Handley Page 115 [30,31] research aircraft was designed to study the aerodynamic and handling qualities of slender wing aircraft at low speed flight conditions. This airplane experience a wing rock motion when the angle of attack exceeded approximately 20° , as shown in Fig. 2. The motion was essentially a rolling oscillation about the longitudinal axis. The maximum bank angle was $+40^\circ$ at an angle of attack of 30° . The yaw oscillations were found to be less than $\pm 3^\circ$. The pilot was able to suppress the motion by aileron input or reducing the angle of attack. It should be pointed out that wing rock is not limited to a few aircraft; rather, it is a phenomenon which can be traced back to some of the early swept-wing fighter airplanes. In fact, over 13 modern aircraft have been documented to exhibit the phenomenon.

1.1.2. Wing drop

Wing drop is an abrupt uncommanded rolling motion that can occur during a high-g turn or pitch-up maneuver [32]. The most likely cause of this unexpected motion is a premature flow separation on one wing.

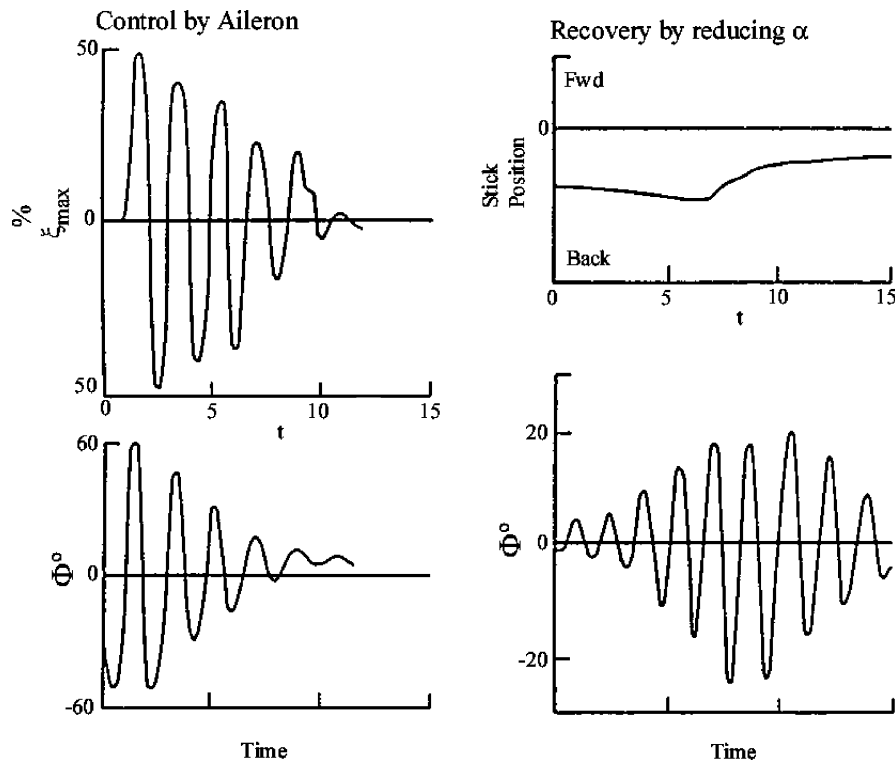


Fig. 2. Wing rock behavior of the Handley Page 115 aircraft [31].

Flow separation can be very sensitive to small local changes in Reynolds number, Mach number, angle of attack and sideslip angle. As the angle of attack is increased during a maneuver, flow conditions may occur where some portion of the wing is on the verge of separating. If the flow separates asymmetrically on one wing, as shown in Fig. 3, then a rolling moment is created. The history of the maneuver up to the point of flow separation will govern whether the motion results in a wing drop. The magnitude of the rolling moment will depend upon the location of the flow separation; the farther outboard on the wing the asymmetric separation occurs, the larger the rolling moment.

One of the perplexing features of wing drop is the random nature of its occurrence during what appears to be identical flight maneuvers. One may have to fly the same maneuver several times before a wing drop occurs. Since asymmetric flow separation can occur on either wing section, the direction of the wing drop is not known a priori. Another factor that enters into the severity of the wing drop besides the location of the separation is the time difference between when separation occurs on both wings. If the asymmetric separation exists for only a very short time before a similar separation occurs on the other wing, then the asymmetric loading will not have time to cause a significant roll excursion.

A recent example of wing drop was reported in the aviation press in 1999. The F-18 E/F aircraft encountered problems with wing drop during the flight test program. A significant amount of additional testing and engineering support was required to find a successful solution to the wing drop problem. It should be noted that wing drop is not unique to the F-18 and has been experienced by a number of aircraft. Although wing rock and wing drop have occurred during the development of many fighter aircraft, the basic understanding of the flow mechanisms that cause these unwanted rolling behaviors is still rather limited.

1.1.3. Heavy wing

The flight characteristic called heavy wing occurs when an aircraft experiences a gradual roll-off from the trimmed flight condition. To eliminate the roll-off, the pilot must apply a corrective control input. From the pilot's perspective, the aircraft feels as though one wing is heavier than the other, thus the name heavy wing.

The heavy wing problem is not as common as wing rock or wing drop, but it has been observed on the F-84 and other airplanes. For the F-84, the heavy wing problem was believed to be caused by a loss of aileron effectiveness [33], probably caused by shock-induced separation. Another possible theory for heavy wing

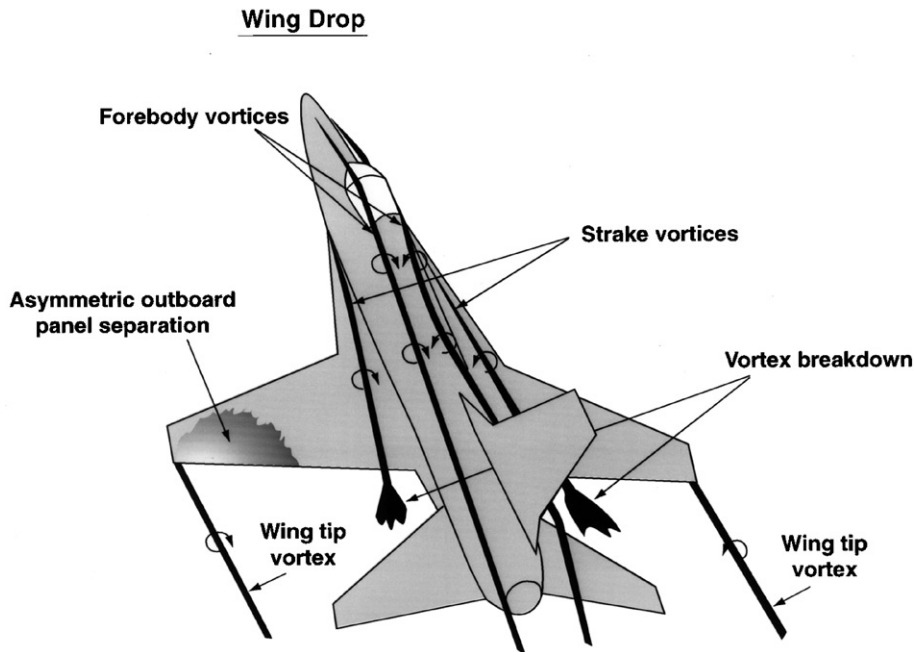


Fig. 3. Asymmetric wing stall.

would be asymmetric wing stall. If the stall is inboard, the rolling moment will be small and the airplane will have a mild roll-off. Thus, it is possible that wing drop and heavy wing are the results of asymmetric wing stall. Whether one gets wing drop or heavy wing depends upon the spanwise location of asymmetric stall.

1.1.4. Nose slice

Nose slice is defined as a rapid yaw divergence that may lead to a spin departure [34–36]. Factors that contribute to the yaw divergence are loss of directional stability, asymmetric yawing moments and adverse yaw. The directional stability and control of a fighter aircraft diminishes with increasing angle of attack. This is due primarily to the influence of the fuselage wake on the vertical tail surface. As the angle of attack is increased, more and more of the vertical tail is immersed in the separated flow field coming off the fuselage. This flow field reduces the effectiveness of the vertical tail as well as the rudder. The ailerons also begin to lose their effectiveness due to stall over the outboard wing panels. The loss of directional stability can lead to yaw divergence.

The nose portion of the fuselage on many modern fighter aircraft consists of a long slender pointed forebody. As the angle of attack of the aircraft is increased, the flow around the forebody separates, as shown in Fig. 4. The forebody vortices are initially symmetric but become asymmetric at some critical angle of attack. When the vortices are symmetric, they

influence the normal force and pitching moment contribution of the fuselage to the airplane aerodynamics. When the vortices become asymmetric, a side force and yawing moment are created, as illustrated in Fig. 5. Because of the reduction of directional stability in this regime, the yaw moment created by the asymmetric vortices can cause the airplane to slice (i.e. to yaw rapidly) to the right or left. The direction of motion depends upon the orientation of the asymmetric vortices.

The nonlinear aerodynamic phenomena that contribute to yaw divergence are configuration dependent. Small changes in the configuration can result in either a significant improvement or degradation in the divergence phenomena.

1.1.5. Buffet

Buffet can be defined as an aerodynamic excitation created by flow separation. The unsteady aerodynamic loads can come from a number of sources, for example wing flow separation, flow interaction between aircraft components, spoilers, etc. Buffet is important because it can affect the structural safety and can also limit the maneuverability of the aircraft [32,37,38].

From a flight mechanics point of view, the pilot perceives buffet as a vertical vibration. The buffet intensity is measured in terms of the acceleration normal to the flight path. The severity of the buffeting is classified by the magnitude of the normal acceleration, as shown in Table 2.

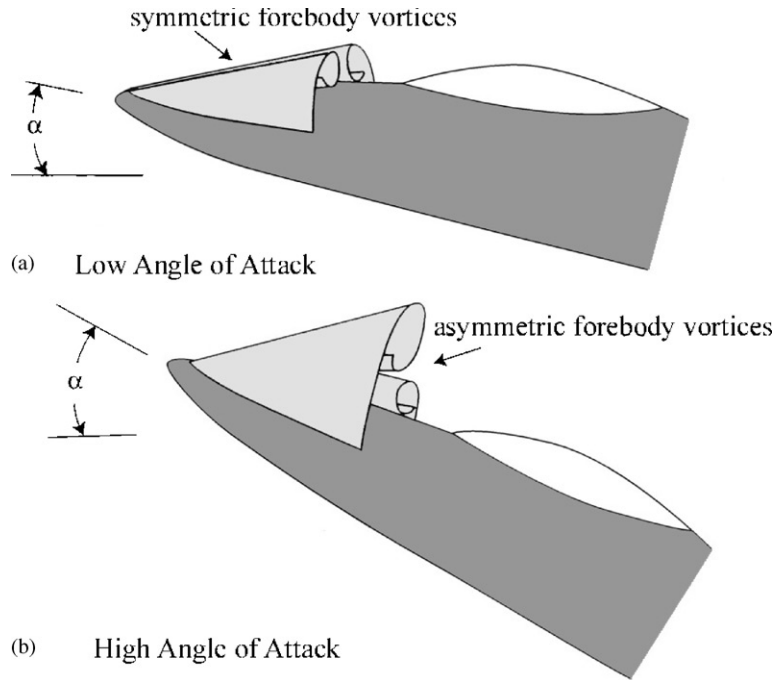


Fig. 4. Forebody flow separation.

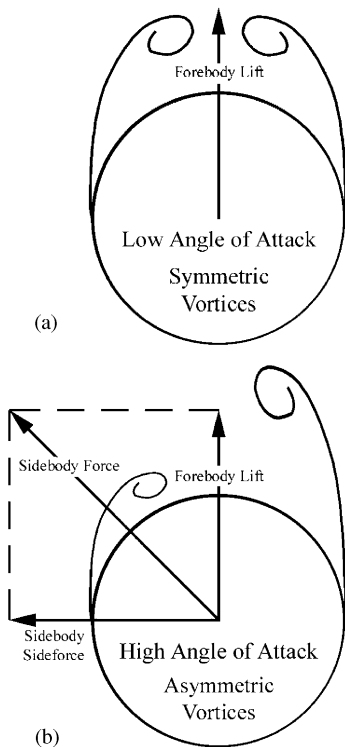


Fig. 5. Cross-sectional flow patterns on a slender forebody.

Table 2
Buffet intensity and pilot perception [32]

Intensity	Acceleration N_z (g)	Effect on pilot
Onset	± 0.035 to ± 0.1	Just barely perceptible to the pilot
Light	± 0.1 to ± 0.2	Definitely perceptible
Moderate	± 0.2 to ± 0.6	Very annoying, precision tracking may be impossible, maneuverability is restricted
Severe	± 0.6 to ± 1.0	Unacceptable and can only be tolerated for a few minutes

Although most fighter aircraft experience buffeting during transonic maneuvers, it is extremely important that the level of buffet does not interfere with the pilot's ability to perform precision tracking.

1.2. Summary

This article presents a review of the aerodynamic characteristics of slender delta wings at large angles of attack under static and dynamic conditions. Flying at

high angles of attack is intrinsically an unsteady flight regime, and as such an understanding of the unsteady aerodynamics of swept wings is of value. The discussion will emphasize the fluid mechanic mechanisms governing the nonlinear aerodynamic loads. Emphasis will be given to showing the relationship between the force and moment coefficients, surface pressures and the flow field structure. The examples of unsteady motion include single degree-of-freedom large amplitude pitching or rolling motions. The article will also include several examples of the dynamic phenomena experienced by high performance aircraft such as the F-18 HARV (High-Alpha Research Vehicle) and the X-31 and how the unsteady aerodynamic characteristics affect the flight dynamics of these vehicles. Finally, the article will conclude with an assessment of aerodynamic modeling techniques that are suitable for predicting maneuvers where unsteady aerodynamics is important.

2. Leading-edge vortical flows on static delta wings

The leading-edge vortices generated by slender wings have been the subject of numerous experimental studies starting in the mid-1950s and continuing to today. Refs. [39–47] are some of the more frequently cited references of the earlier research efforts.

The flow structure on the upper side of a delta wing at angle of attack is extremely complex. At moderate angles of attack, the leeward flow field for these planforms is dominated by a highly organized vortical flow structure emanating from the sharp leading edges. The contribution of the vortical flow to the aerodynamic characteristics of the delta wing is a function of the leading-edge geometry. Chu and Luckring [48] showed that the characteristics of a 65° swept delta wing were slightly different for different leading-edge geometries, from sharp to elliptical. A sketch of the classic leading-edge flow field above a delta wing is shown in Fig. 6. The vortex sheet shed from the leading edge rolls up into a pair of leading-edge or primary vortices. The leading-edge vortices induce a flow in the spanwise direction on the upper surface. This outward flow separates from the surface forming a smaller secondary vortex outboard and below the leading-edge vortex. It is possible that there are additional vortices near the surface in this region. The surface flow patterns can be equally complex, as also illustrated in the sketch in Fig. 6. The surface patterns reveal the attachment and separation lines of the primary and secondary vortices. The interpretation of surface and off-surface visualization patterns can be, at times, very difficult. However, flow topology methods have been used by Perry and Chong [49], Peake and Tobak [50], and Délerly [51,52] to explain the flow structure around various aerodynamic shapes.

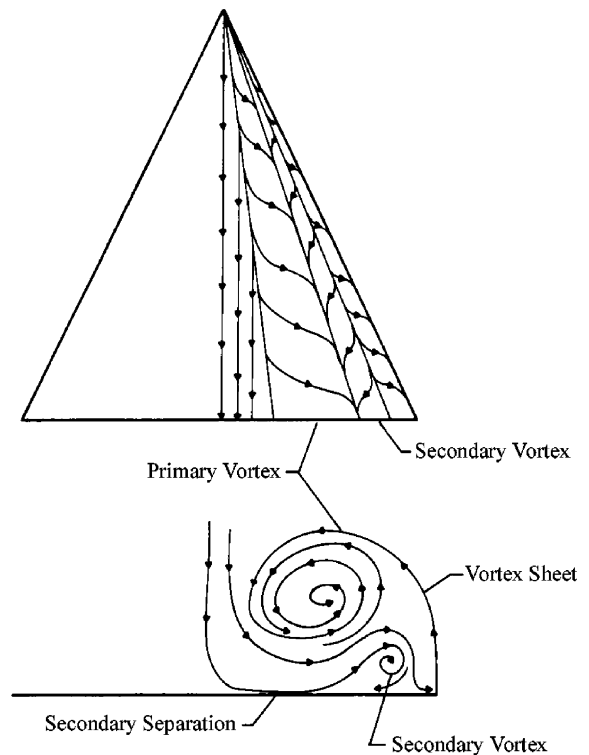


Fig. 6. Sketch of the leading-edge flow structure above a sharp-edge delta wing.

The flow topology rules provide a fundamentally sound basis for constructing detailed flow topology images.

Earnshaw [46] proposed that the leading-edge vortex on a delta wing could be divided into three regions: the shear layer, rotational core and viscous subcore. The shear layer, or vortex sheet, is generated at the wing's leading edge and feeds vorticity into the vortex core. The thickness of the shear layer increases with increasing distance from the leading edge. The rotational core is approximately 30% of the local semi span in diameter, wherein the traces of the vortex sheet produce only minor perturbations on the circumferential or longitudinal velocity distribution. The vorticity inside the core is assumed to be distributed continuously. The viscous subcore, approximately 5% local semi span in diameter, is a region in which the gradients of local head, static pressure and velocity are very high. The subcore rotates as a solid body and the axial velocity can exceed three times the freestream value. Fig. 7 is a sketch illustrating the various regions of the vortex as described by Earnshaw.

The leading-edge vortices above a slender, flat-plate delta wing can be visualized by introducing a marking material into the flow. The vortices are marked by the entrainment of marking material, and can be illuminated

at locations along the wing by a laser light sheet that is normal to the wing surface [53,54]. Fig. 8 is a photograph of the laser light sheet illumination of the crossflow section through the leading-edge vortices made visible by smoke. The smoke patterns clearly show the vortical nature of the flow field. The vortical flow field on the leeward side of the delta wing is characterized by large velocity variations. As the angle of attack of a delta wing is increased, the leading-edge vortices grow in strength and at some point along the vortex, breakdown occurs. The change in the flow structure after breakdown is shown in Fig. 9. In this photograph, the vortex is breaking down at approximately 50% of the root chord [53]. It is interesting to notice how rapidly the core region expands after breakdown. For very large sweep angles, vortex break-

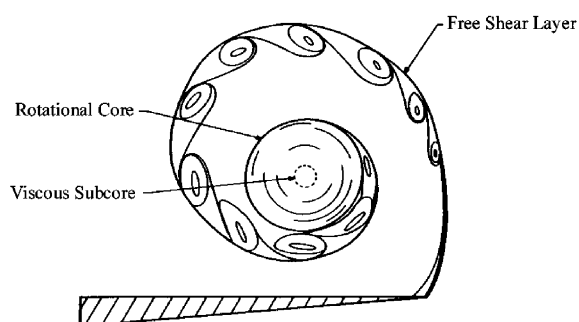


Fig. 7. Three regions within a leading-edge vortex.

down has been found to occur asymmetrically due to a possible interaction between the vortices. When the sweep angle is less than 80° , breakdown tends to be symmetric. It should also be noted that the position of the vortex breakdown is not stationary, even for a stationary model. The breakdown position is unsteady and typically oscillates about some mean position [55,56].

2.1. Flow features of leading-edge vortices

The velocity field associated with the leading-edge vortices of simple delta wing planforms has been studied using pressure probes, hot-wire, PIV (particle image velocimetry) and Laser Doppler Anemometry. Non-intrusive measurements of the velocity distribution through a leading-edge vortex above a slender delta wing is presented in Fig. 10. These measurements were made by Pagan and Solignac [57]. The flow surveys were obtained using laser anemometry in the wake of a 75° swept delta wing. The measurements were made just aft of the wing trailing edge (at $x = 0.27c$ behind trailing edge) in the wake.

Prior to breakdown, the leading-edge vortex can best be described as a swirling jet flow, as illustrated in Fig. 10. These measurements show the variation of the velocity distribution through the leading-edge vortex as a function of angle of attack. As the angle of attack is increased, both the maximum axial velocity at the vortex center and the maximum tangential velocity increase. The jetting along the vortex center line can be up to



Fig. 8. Laser light sheet illumination of the crossflow and longitudinal axis of the leading-edge vortices above an 85° swept delta wing ($\alpha = 20^\circ$ without vortex breakdown) [53].

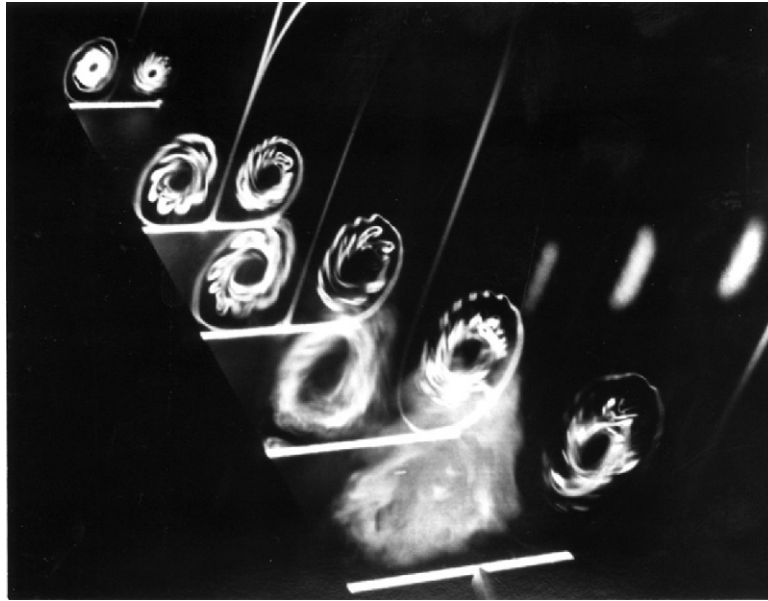


Fig. 9. Laser light sheet illumination of the crossflow and longitudinal axis of the leading-edge vortices above an 85° swept delta wing ($\alpha = 40^\circ$, vortex breakdown) [53].

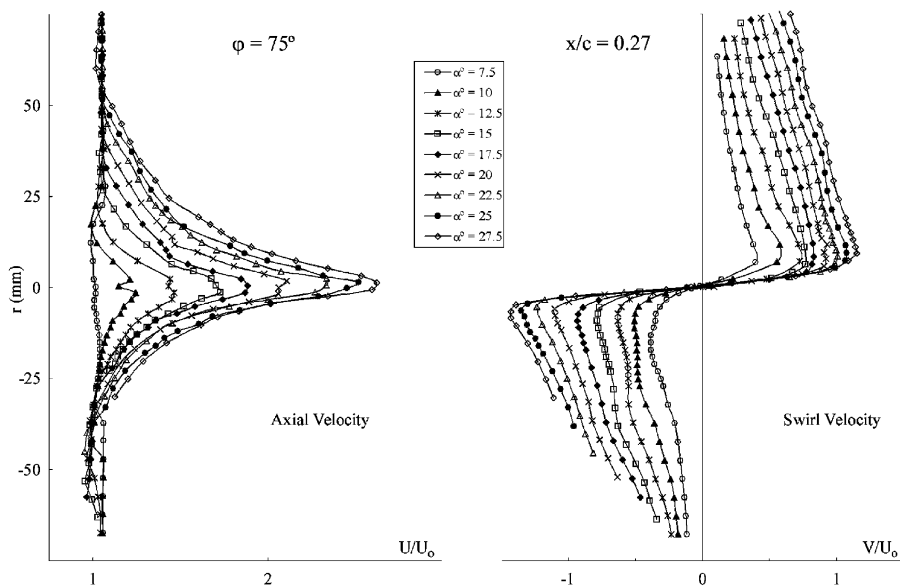


Fig. 10. Velocity distribution through a vortex prior to breakdown [57] (measured at $x = 0.27c$ behind trailing edge).

three or more times the freestream velocity depending upon the wing sweep angle. Erickson [58] explains the large axial velocity within the leading-edge vortex by means of a spiraling vortex sheet. The vortex sheet, originating at the wing leading edge, spirals around the vortex axis as it convects downstream. The spiraling vortex lines are inclined to the vortex axis and induce an

axial flow in the downstream direction. For this particular wing, the maximum axial velocity is over 2.5 times the freestream velocity. The other noticeable feature is the relative size of the jet core vs. the core associated with the maximum tangential velocity. The jet core increases with angle of attack and for the largest angle of attack shown in Fig. 10, the jet core is

approximately 50% of the wing semi span, whereas the core based upon the distance between the maximum and minimum tangential velocities is approximately 5–10% of the semi span. The smaller core region remains essentially the same size as the angle of attack is increased. These two core structures are similar to those proposed by Earnshaw [46].

2.1.1. Vorticity and circulation

The vorticity distribution and circulation provide additional understanding of the overall structure of the leading-edge vortices. Several investigators have put forth ideas specifically concerned with aspects of vorticity and circulation. Lee and Ho [59] state that “a stationary leading-edge vortex is achieved only when the convection of vorticity along the core axis balances the vorticity generation from the boundary layer of the leading edge” and the swirl angle is an indicator of this balance. A reduction in the axial convection, via the adverse pressure gradient downstream and at the trailing edge of the planform, is concluded to cause vortex breakdown.

The argument of a critical vorticity distribution can be substantiated in light of the work by Pagan and Solignac [57] and Détery et al. [60]. They examined the effects of an adverse pressure gradient on a vortex generated by a 75° swept delta wing at $\alpha = 27.5^\circ$. The vortex was allowed to enter a two-dimensional duct with movable flaps at the aft end enabling various pressure distributions to be created in the duct. Their results indicate that maximum vortex strength, as given by the maximum swirl velocity ratio, is strongly dependent on the local

freestream pressure gradient. This can also be interpreted that the maximum amount of vorticity or circulation at a given station is limited by the ability of the flow to move downstream, which in turn is regulated by the pressure gradient.

A hypothesis by Brown and Lopez [61], based on the physics governing a stagnant recirculating flow region in confined cylindrical flows, argues that breakdown mechanisms rely on the production of negative azimuthal vorticity. This results from a tilting and stretching of the predominantly axial vorticity vector, ω_x . Vorticity diffusion leads to a radial redistribution of the circulation and a stretching and tilting of vortex lines due to a local increase of the tangential velocity, V_θ . A reduction in the initially positive azimuthal component of vorticity occurs with axial distance and the subsequent “inviscid breakdown” process develops.

Unfortunately, the information on the vorticity distribution within the leading-edge vortices is quite limited. In a study by Visser and Nelson reported in Refs. [62–64], hot-wire anemometry was used to examine the vorticity and circulation distributions above a 75° swept delta wing. The axial, radial and azimuthal vorticity components were measured. The majority of the axial vorticity components were found to be confined to 10% of the span on either side of the vortex core center location. The azimuthal vorticity was smaller in magnitude. Fig. 11 is a plot of the axial vorticity at numerous stations along the wing. The axial vorticity has been nondimensionalized and results are overlaid for each of the measured x/c locations; similar profiles are seen to exist at each station.

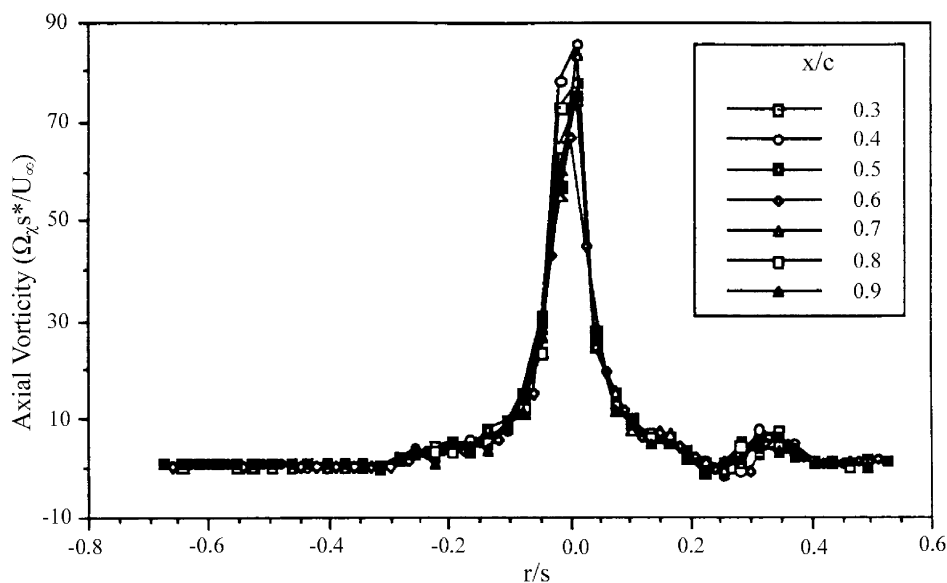


Fig. 11. Axial vorticity distribution [62].

The circulation, Γ , is also calculated using the definition given below.

$$\Gamma = \int_c V \cdot dr = \int_A (\nabla \times V) \cdot dA = \int_A \Omega \times dA. \quad (1)$$

The circulation is shown in Fig. 12; the values are plotted outward from the core center ($r = 0$) where the radial distance has been nondimensionalized by the local semi span. Each curve represents a chordwise location and the circulation is seen to grow in a chordwise manner. This is what one would expect, as the feeding sheet is continually being wrapped into the vortex. The circulation increases at a decreasing rate from the vortex center and reaches a maximum near the wing leading edge.

2.1.2. Vortex strength correlation

Parameters can be defined to incorporate external conditions, such as the sweep angle and angle of attack, along with the measured flow field properties in an effort to determine what, if any, interaction occurs near breakdown. This approach has already been utilized, to a certain extent, by scaling the field properties by the local semi-span. A more direct line of reasoning was incorporated by Hemsch and Luckring [65] in a correlation for the measured vortex circulation. Their relation utilized a parameter derived by Sychev [66] in his Euler analysis of flow about an arbitrary slender body. Sychev assumed

$$d = s/c \ll 1 \quad (2)$$

and obtained an approximate set of equations for the inner region of the flow involving only the parameter $k_1 = d \cot(\alpha)$. Hemsch and Luckring [65] used this Sychev parameter to correlate the strength of a vortex at the trailing edge of sharp leading-edge delta wing in the form of

$$g = \frac{\Gamma}{U_\infty c \tan^2 \epsilon \cos \alpha} = AK^n, \quad (3)$$

where

$$K = \tan \alpha / \tan \epsilon = 1/k_1 \quad (4)$$

for some constant values of n and A , and with the apex half-angle ϵ . By plotting g and K in a log-log format, they demonstrated that a fit of the form $g = AK^{1.2}$ was seen for data obtained from Wentz and MacMahon [67], and that of Détery et al. [60]. Values of g and K ranged from 0.5 to 10.0 and 0.2 to 2.0, respectively. A value of $n = 1.2$ was seen to accurately fit the numerical conical slender body theory of Smith [68].

Visser [62] applied this technique to his circulation measurements. Experiments by Visser et al. [62–64] were conducted at locations above the wing surface, a further scaling of g by the local chord ratio x/c was found to bring the data into line with theory for $A = 4.63$, as shown in Fig. 13. The seven-hole probe data of Payne [53] were also scaled by x/c and are presented in Fig. 13 along with that of Wentz and MacMahon [67]. Payne’s data represent sweep angles of 70°, 75°, 80°, and 85° at various chord locations. It is seen to extend the theoretical line of Smith [68] to a g of 100 and a K of

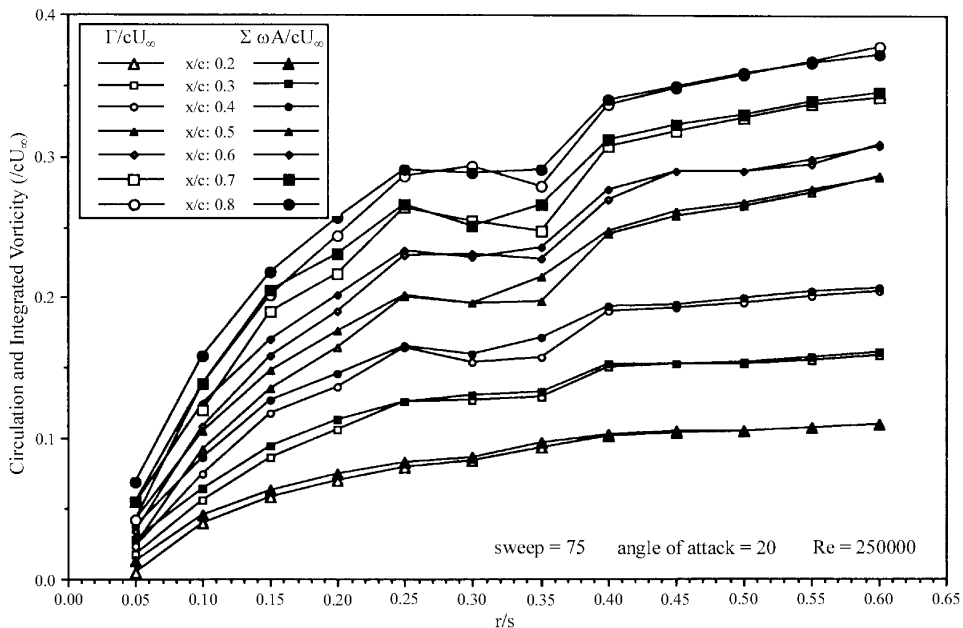


Fig. 12. Radial distribution of circulation and integrated vorticity [62].

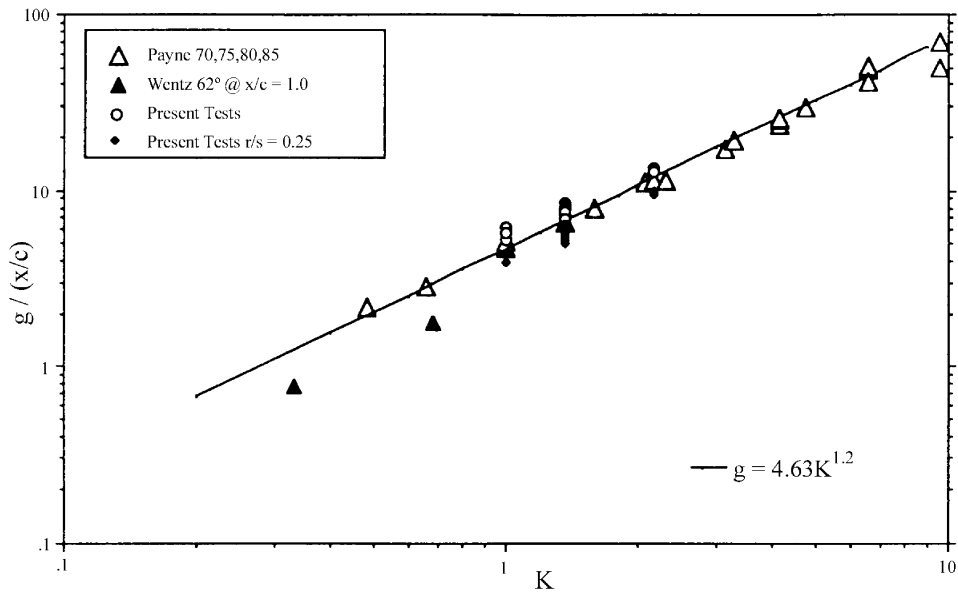


Fig. 13. Sychev parameter based on correlation of Hemsch and Luckring as presented by Visser [62].

10. Thus, it would appear that the relationship developed by Hemsch and Luckring is effective in correlating the vortex strength with the angle of attack and the wing geometry.

2.1.3. Vortex breakdown

Vortex breakdown represents a limiting condition for slender wings. Once vortex breakdown reaches the wing, the surface pressure field begins to be altered and the lift curve slope is reduced. As the breakdown progresses toward the apex of the wing, the maximum lift coefficient is reached. Stall occurs when the leeward flow completely separates from the wing. There are a number of theories for vortex breakdown, however, at this time no one theory has been widely accepted. A detailed discussion of vortex breakdown theories can be found in the references by Leibovich [69–71], Wedemeyer [72], Benjamin [73], Hall [74,75], Ludwig [76,77] and Déléry [78].

Much of what we know about vortex breakdown comes to us from experiments conducted on an isolated vortex created inside a tube [79–87]. Many different types of breakdown have been identified in vortex tube experiments. For slender wings at angle of attack, only two types of breakdown are generally identified: the bubble and the spiral types, although in reality, they may just represent the extremes in a continuum of breakdown forms. Examples of either a bubble or spiral breakdown are shown in the following photographs. In Fig. 14, the core flow seems to expand around an oval-shaped recirculation zone. At the exit of this recirculation zone, the core flow appears to shed in the form of

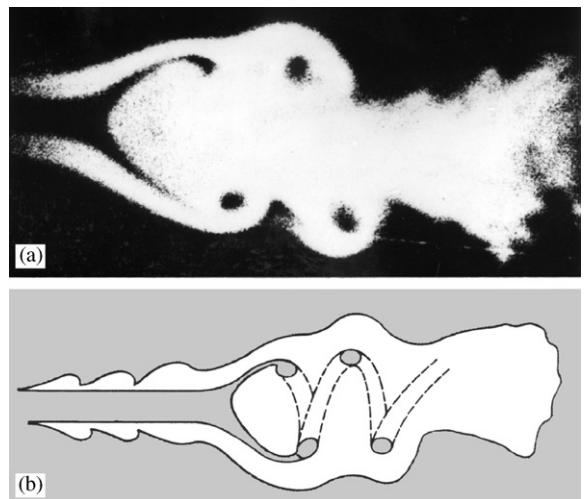


Fig. 14. Schematic of bubble type breakdown from enlargement of 16 mm movie frame (longitudinal cross section) [53].

vortex rings which are then convected downstream. The cross section of these doughnut shaped vortex rings appears as a pair of holes in the smoke.

Fig. 15 shows a transversal cross section of the recirculation zone which is surrounded by a ring of core flow. The breakdown process occurring above was occasionally observed to change into what might be interpreted as a spiral mode. When this occurred, the mean location of the breakdown moved downstream and took the form depicted in Fig. 16. The large

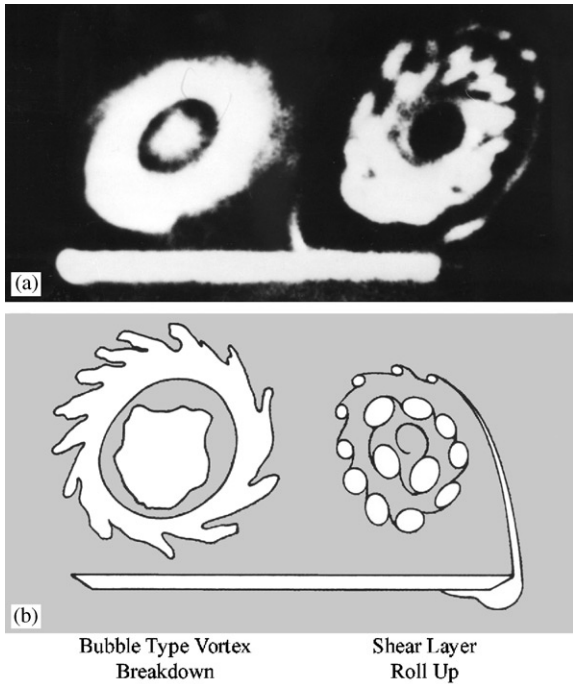


Fig. 15. Schematic of bubble type vortex breakdown from enlargement of 16 mm movie frame (transversal cross section [53]).

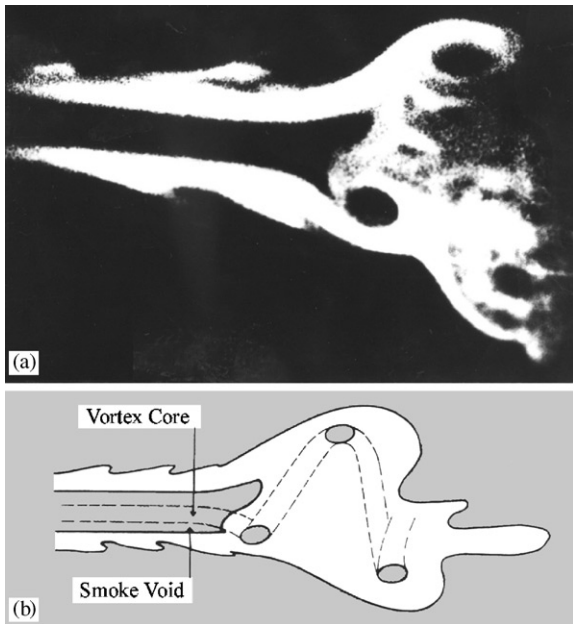


Fig. 16. Schematic of spiral type breakdown from enlargement of 16 mm movie frame (longitudinal cross section) [53].

recirculation zone has disappeared and the core flow now appears to corkscrew downstream. In this case, the holes in the flow are assumed to be the cross section of the spiraling core flow. This type of result was also

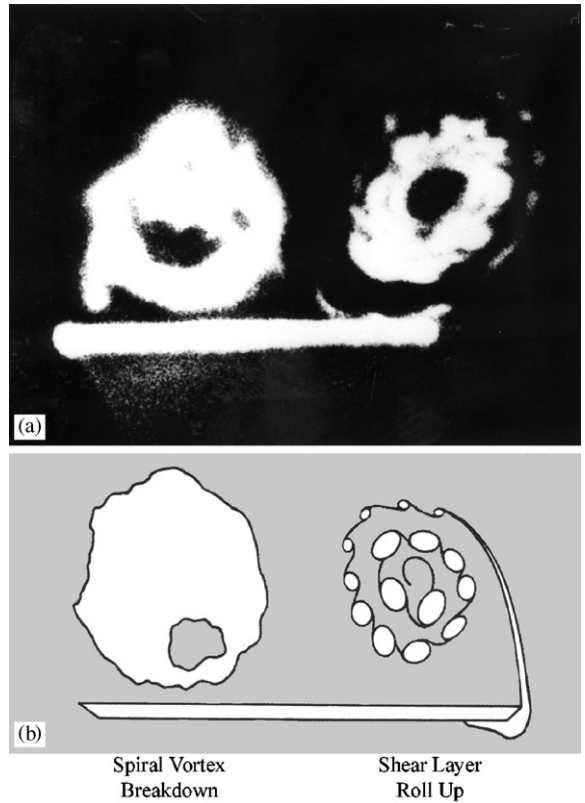


Fig. 17. Schematic of spiral type breakdown from enlargement of 16 mm movie frame (transversal cross section [53]).

obtained in wind tunnel tests at ONERA using the laser light sheet technique [57,60]. In that study, “holes” appearing in the wake of a breakdown were also observed and interpreted to be cross section of the spiraling vortex core. Fig. 17 shows a transversal cross section which appears to show a rotating core. After a short time, this spiral mode would transform back into the “bubble” form and move upstream.

The position of breakdown has been measured by numerous investigators. Fig. 18 shows the effect of sweep angle and angle of attack on vortex position [88]. For a given sweep angle, the breakdown position moves from the wake onto the wing toward the wing apex with increasing angle of attack. Sweep angle affects the onset angle of vortex breakdown. The higher the leading-edge sweep angle the higher the onset angle. Fig. 19 shows the effect of sideslip angle on the position of breakdown. When a slender wing at angle of attack is given a sideslip angle, the leading-edge vortex on the upwind side (with respect to the sideslip angle) breaks down closer to the apex while the other vortex breaks down farther away from the apex. This is consistent with the effective change in sweep created by the sideslip. The upwind side of the wing has an effective decrease in

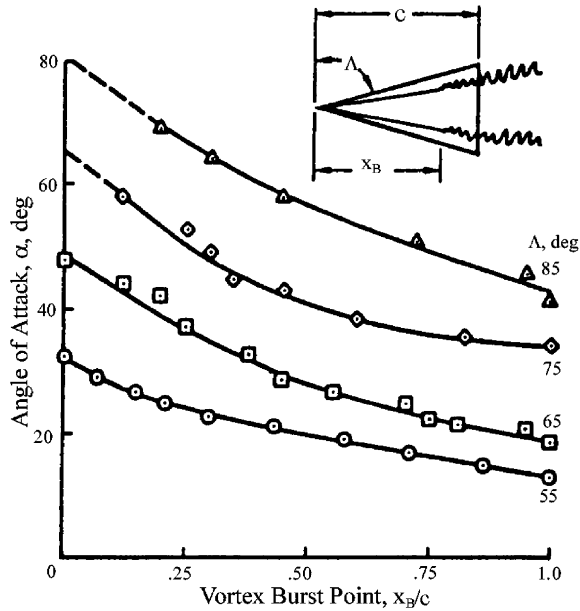


Fig. 18. Vortex breakdown position on delta wing models [88].

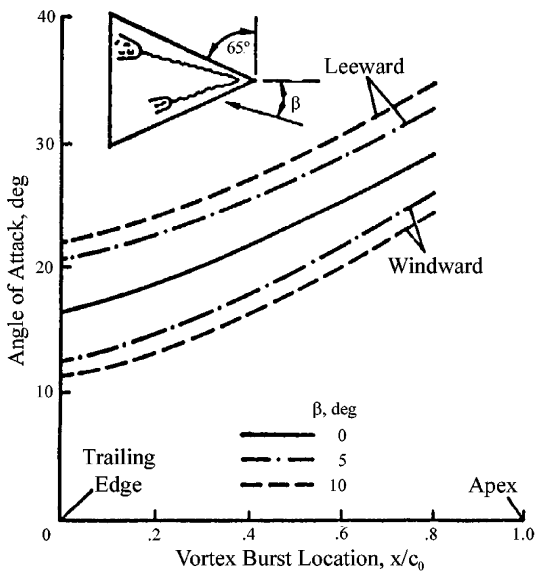


Fig. 19. Vortex breakdown for varying sideslip angles [88].

sweep angle while the downwind side has an effective increase in sweep. Because increasing sweep favors a delay in vortex breakdown, the influence of sideslip on vortex breakdown is as expected.

The position of breakdown is also affected by the thickness of the model, the leading-edge geometry [89,90], the trailing-edge geometry, the sting mounting, etc. Fig. 20 shows the effect of the leading-edge

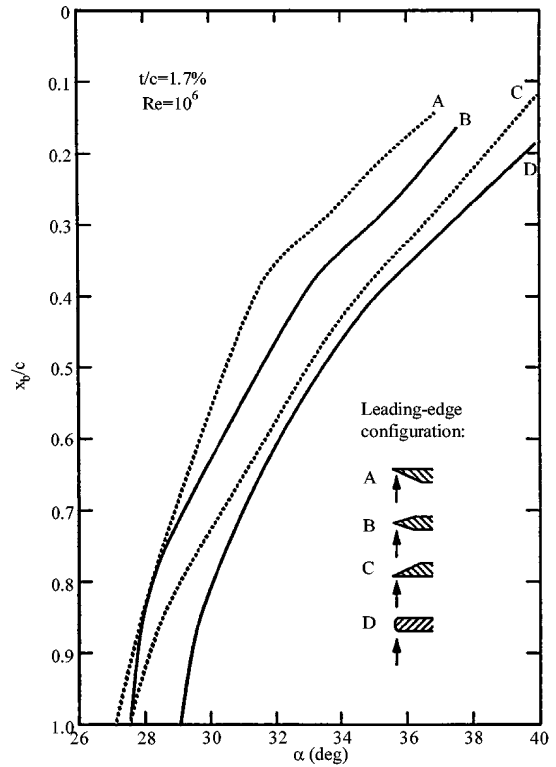


Fig. 20. Effect of leading-edge geometry on vortex breakdown [90].

geometry on vortex breakdown for a 70° swept delta wing. Jobe [91] looked at 38 sets of vortex breakdown data on a 65° delta wing and found a significant amount of scatter in the data. For instance, the angle of attack for the onset of vortex breakdown over the wing was shown to vary significantly for the different 65° swept models. The variation in the measurements is probably due to support and blockage effects. This large range of breakdown locations for a given sweep angle makes predictions even more difficult.

Since vortex breakdown affects the loads acting on a wing, its location on a wing must be known before making any load prediction. Huang and Hanff [92] presented an analytical model for breakdown location prediction based on empirical data. This analytical model was used to predict the normal force acting on a rolling delta wing at high angles of attack.

As discussed earlier, once vortex breakdown has occurred, the flow structure of the leading-edge vortices changes dramatically. Details of the flow before and after vortex breakdown were studied by Iwanski [93] and Ng et al. [94] on a sharp-edge delta wing having a leading-edge sweep of 70° for 30° angle of attack. Fig. 21 is a sketch showing the approximate positions of the survey planes relative to the vortex breakdown.

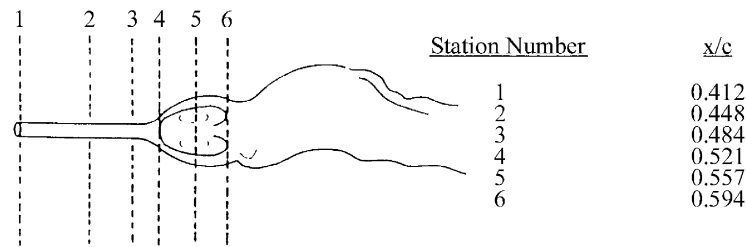


Fig. 21. Relative position of wake surveys to vortex breakdown position [93,94].

In interpreting these data, one should keep in mind the breakdown position is not stationary. The spanwise variation of the axial and tangential velocity components through the leading-edge vortex above a sharp-edge delta wing having a leading-edge sweep of 70° is shown in Fig. 22 for various chordwise positions along the wing. In Fig. 22a, upstream of the breakdown ($x/c = 0.412$ and 0.448), the axial velocity component within the vortex is similar to a jet-like flow discussed earlier. The peak axial velocity occurs at the center of the vortex and is approximately three times the freestream velocity. The jet-like region is approximately 0.5 semi-span wide. The first indication that vortex breakdown is about to be the deceleration of the core flow at $x/c = 0.484$. After breakdown ($x/c > 0.521$), a wake-like velocity defect appears in the axial velocity profile. The wake defect region is approximately 30% of the semi-span wide at $x/c = 0.521$ and broadens with increasing distance downstream.

The tangential velocity component (normal velocity) is shown in Fig. 22b. The peak tangential velocity prior to breakdown is approximately 1.5 times the freestream velocity and after breakdown it is approximately equal to the freestream. Before breakdown, the subcore region is small, as indicated by the steep velocity gradient. However, after breakdown, there is a reduction in the tangential velocity component and a rapid diffusion of the subcore. The subcore region expands from approximately 10% of the local semi-span before breakdown to nearly 50% of the local semi-span after breakdown ($x/c = 0.594$).

The axial vorticity was estimated from the velocity data and is shown in Fig. 23 for the different chordwise locations. The axial vorticity profile distribution is seen to increase in magnitude and narrow in width in the downstream direction, up to $x/c = 0.411$ (just prior to breakdown). The peak then broadens and a reduction in the maximum axial vorticity value is seen as the breakdown region is entered. This is consistent with the breakdown model proposed by Brown and Lopez [61]. From their analysis, they concluded that breakdown occurred due to the production of a negative azimuthal vorticity which is due to a tilting and stretching of the axial vorticity vector. Rockwell et al.

[95] have made detailed vorticity measurements through the leading-edge vortices of a delta wing. Their experimental findings are also consistent with the concept proposed by Brown and Lopez.

Jumper et al. [96] proposed a simple model to explain spiral vortex breakdown. Using an isolated line vortex that deforms into a spiral, they showed that the sense of the spiral had to be opposite that of the circulation in order to produce an induced flow in the upstream sense to sustain the breakdown. This simple model is consistent with experimental findings and the more comprehensive theory also proposed by Brown and Lopez [61].

2.1.4. Pressure gradient

The pressure gradient acting along the vortex axis is an essential factor in the promotion or delay of vortex breakdown. An adverse or positive pressure gradient tends to promote breakdown whereas the opposite effect occurs for a favorable pressure gradient. The pressure gradient imposed on the vortex core can come from a variety of sources. For example, the pressure rise over the rear portion of the delta wing or pressure gradients caused by the wind tunnel walls or obstacles (support systems) located downstream of the generating model but near the vortex wake.

To examine the influence of the pressure gradient on a vortex, various investigators have developed simple analytical expressions relating the pressure gradient to vortex parameters. The reader is referred to the papers by Raat [97], Krause and Althaus [98], and Hall [75].

The pressure gradient acting along the vortex axis can be derived from the radial momentum equation, which after the appropriate simplification reduces to

$$\rho \frac{V_\theta^2}{r} = \frac{\partial P}{\partial r}. \quad (5)$$

This equation represents the balance between the fluid particles centripetal acceleration and the restraining radial pressure force. If we differentiate this expression with respect to the axial distance, x , and integrate with respect to the radial distance, r , then the following

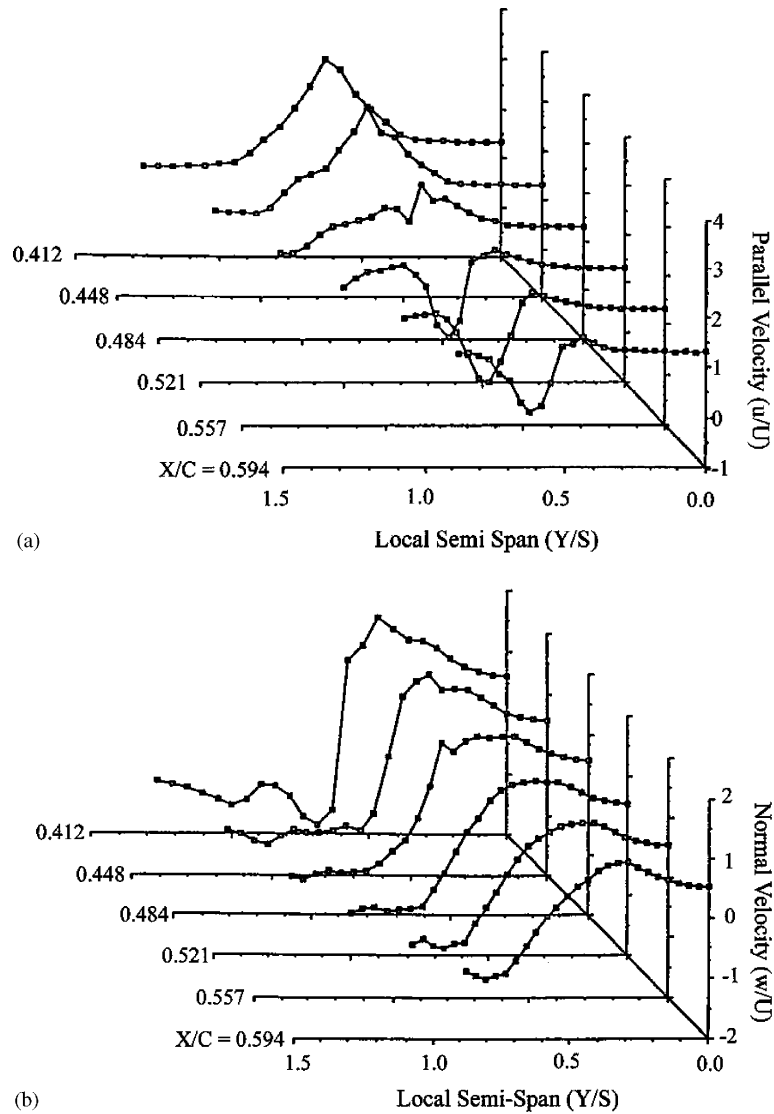


Fig. 22. Velocity field of the leading-edge vortices above a 70° swept delta wing [93,94]. (a) Axial velocity. (b) Normal velocity.

expression for the axial pressure gradient is obtained:

$$\frac{\partial P}{\partial x}\bigg|_0 = \frac{\partial P}{\partial x}\bigg|_r + \frac{\partial}{\partial x} \left[\rho \int_0^\infty \frac{V_\theta^2}{r} dr \right]. \tag{6}$$

This expression shows us that the pressure gradient at large distances from the core center is imposed along the core axis.

The pressure gradient across the core can be shown to be as follows [60]:

$$\frac{\partial P}{\partial x}\bigg|_0 - \frac{\partial P}{\partial x}\bigg|_{r_c} \sim \rho \alpha_d \Gamma^2 / r_c^3, \tag{7}$$

where α_d is the angle of divergence of the vortex core. This expression shows that the pressure gradient along the vortex axis is greater than at the vortex core boundary, the vortex strength being a controlling parameter.

The importance of vortex strength on breakdown can be seen in Fig. 18. As this figure shows, the angle of attack, when breakdown reaches the trailing edge, increases as the sweep angle increases. However, as was shown earlier, the circulation on a delta wing at a given angle of attack decreases as the sweep angle is increased. Therefore, from Eq. (7) one would expect that

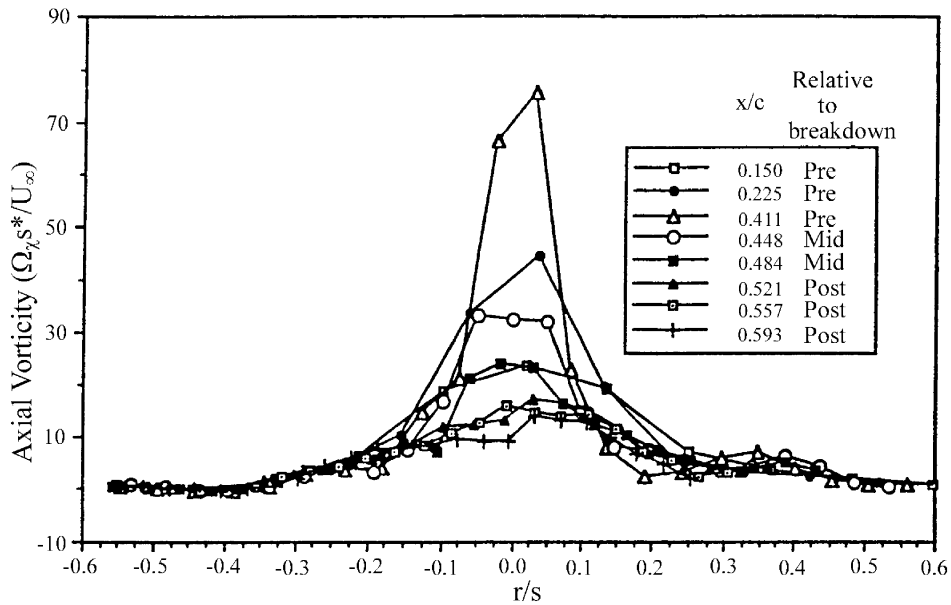


Fig. 23. Axial vorticity distribution [64].

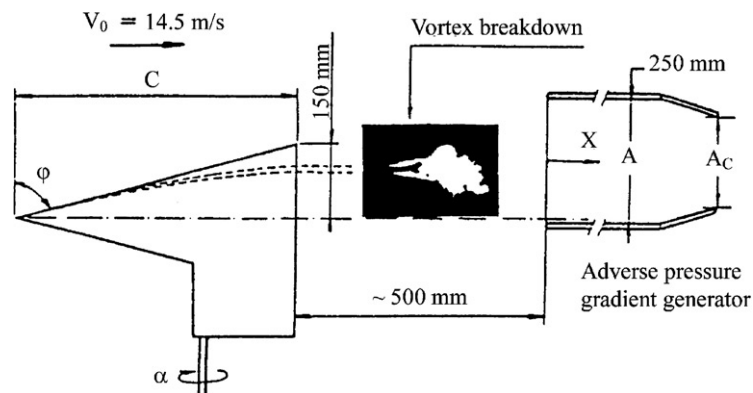


Fig. 24. Experimental setup used to study adverse pressure gradient on vortex breakdown [57].

as the wing sweep is increased vortex breakdown would be delayed to a higher angle of attack. This is exactly what is observed experimentally.

Experiments conducted by Délerly et al. [60] confirm the importance of both vortex strength and adverse pressure gradient on vortex breakdown. Their experimental setup consisted of a 75° delta wing and a two-dimensional air intake located downstream of the delta wing. The exit area of the intake could be varied to change the magnitude of the adverse pressure gradient. Fig. 24 is a sketch of their experimental setup. They measured flow characteristics at approximately $1/4$ chord length downstream of the wing trailing edge. Fig. 25 shows the axial and circumferential velocity distributions along the centerline of the vortex. These

data illustrate several key features of leading-edge vortices. Notice the large drop in the axial velocity and vorticity for the measurements made after breakdown. The influence of the pressure gradient on vortex breakdown was examined by varying the two-dimensional duct area. Fig. 26 shows the relationship between the pressure gradient and vortex strength as given by the local swirl velocity ratio. A limit to vortex strength was found, beyond which breakdown occurred even in the absence of an adverse pressure gradient.

2.1.5. Pressure fields after breakdown

The pressure distribution on the surface of a slender wing (aspect ratio of 1) at angle of attack is shown in Fig. 27. This data is for an angle of attack where

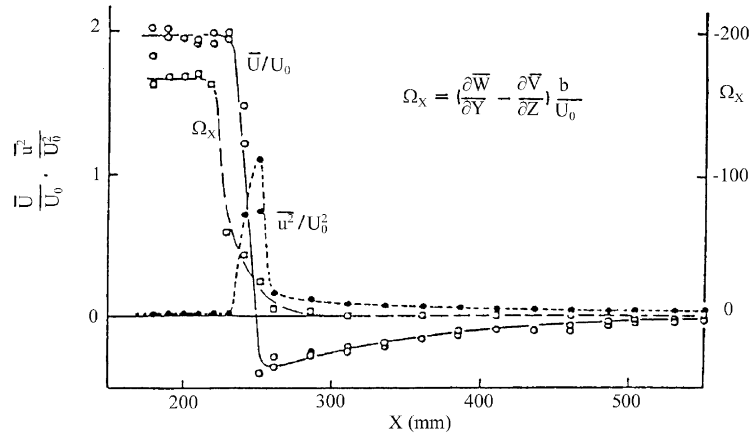


Fig. 25. Axial variation of vortex properties [57].

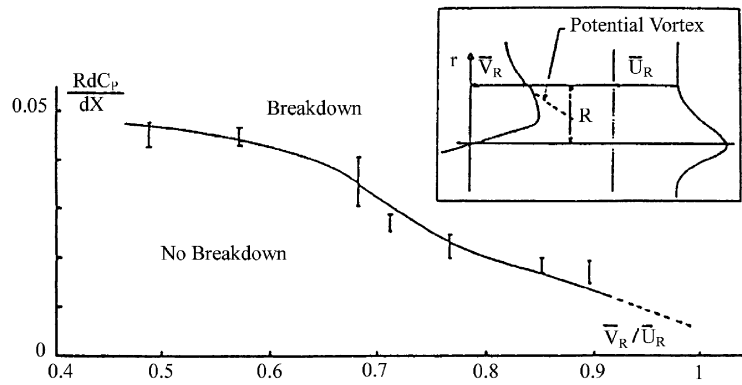


Fig. 26. Influence of adverse pressure gradient on breakdown limit [57].

breakdown has not reached the wing. The large suction peaks or low pressures occur directly beneath the primary vortices. This conclusion was reached by correlating the pressure data with above surface flow visualization data. It should be noted that in some experiments, evidence of secondary suction peaks have been observed. The maximum suction peaks decrease in the downstream direction, since the region of low pressure acts over a larger area. When vortex breakdown occurs, the pressure distribution is changed markedly. When breakdown occurs, the suction peak is reduced significantly but the footprint of the vortex acts over a wider region.

As noted earlier, the sideslip angle affects the position of the vortex breakdown. Vortex breakdown becomes asymmetric with sideslip angle, as indicated in Section 2.1.3. The vortex on the windward side of the wing (with respect to the sideslip) moves closer to the apex, the reverse is true of the leeward side vortex. The effect of sideslip angle on the surface pressure distribution is

shown in the data from Hummel [99], as presented in Fig. 28.

2.2. Aerodynamic characteristics

The aerodynamic characteristics of slender sharp-edge wings are nonlinear, as illustrated in Fig. 29. A significant portion of the lift generated by a slender wing is attributable to a low pressure region created on the wing surface by the leading-edge vortices. This region of low pressure is due to the flow field created by the vortices. As the wing sweep is increased, there is a reduction of the lift curve slope. As mentioned earlier, the circulation increases with angle of attack, but for a given angle of attack the circulation decreases with increasing sweep angle. Therefore, the reduction in the lift curve slope with sweep angle is to be expected. When vortex breakdown reaches the wing, the low pressure region created by the vortices is reduced. The reduction in the suction pressure results in a lowering in the lift

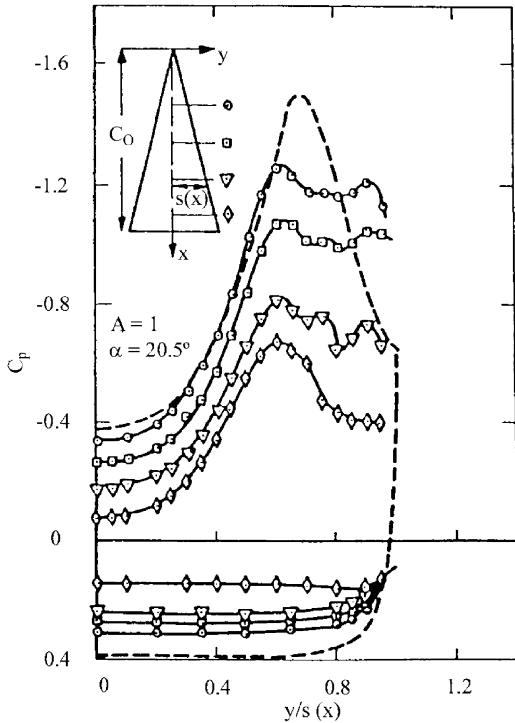


Fig. 27. Upper surface pressure distributions [41].

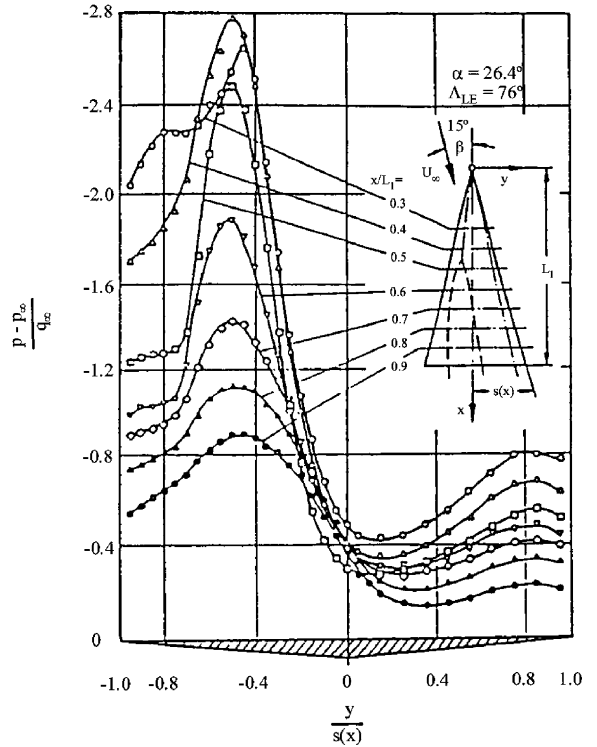


Fig. 28. Influence of sideslip angle on upper surface pressure distribution [99].

curve slope. Although the lift may still continue to increase (as is the case for wings with $\Lambda < 70^\circ$) [89], the lift curve is starting to bend over. As the breakdown progresses forward on the wing, the maximum lift coefficient is reached and the wing stalls. Fig. 30 shows the lift and pitching moment coefficient for delta wings of varying aspect ratio at low speeds. These data were obtained by Wentz and Kohlman [10]. At low angles of attack, the lift and pitching moment coefficients are linear. However, as the angle of attack is increased further, the lift produced by the leading-edge vortices produces the nonlinearity in the force and moment curves. Increasing the aspect ratio (lowering the sweep angle) results in higher normal force coefficients. This can be explained in the following manner. For a given angle of attack, the strength of the leading-edge vortices increases with increasing aspect ratio or lower leading-edge sweep. Therefore one would expect higher vortex lift at a given angle of attack for the higher aspect ratio delta wings.

The influence of vortex breakdown on the lift characteristics of a family of delta wings is shown in Fig. 31. Roos and Kegelman used the experimental measurements of Wentz and Kohlman to show how vortex breakdown was related to the maximum lift coefficient. For low sweep angles (i.e. higher aspect ratio), breakdown occurs over the wing well before the

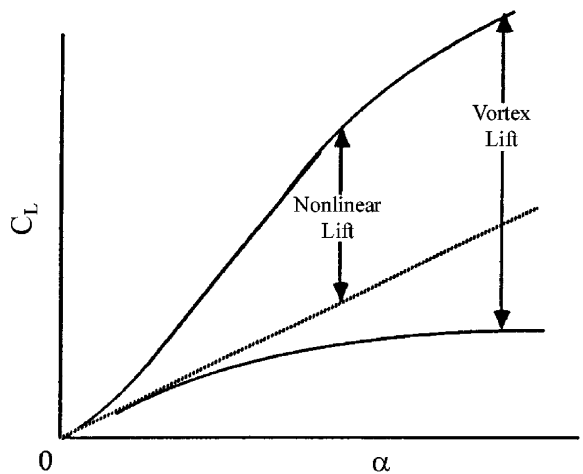


Fig. 29. Sketch of nonlinear lift.

maximum lift occurs. However, as the sweep angle increases, the angle of attack at which breakdown crosses the trailing edge (α_{BD}) moves closer to the angle of attack for maximum lift ($\alpha_{C_{Lmax}}$). For wings having sweep angles greater than or equal to 75° , $\alpha_{BD} \approx \alpha_{C_{Lmax}}$.

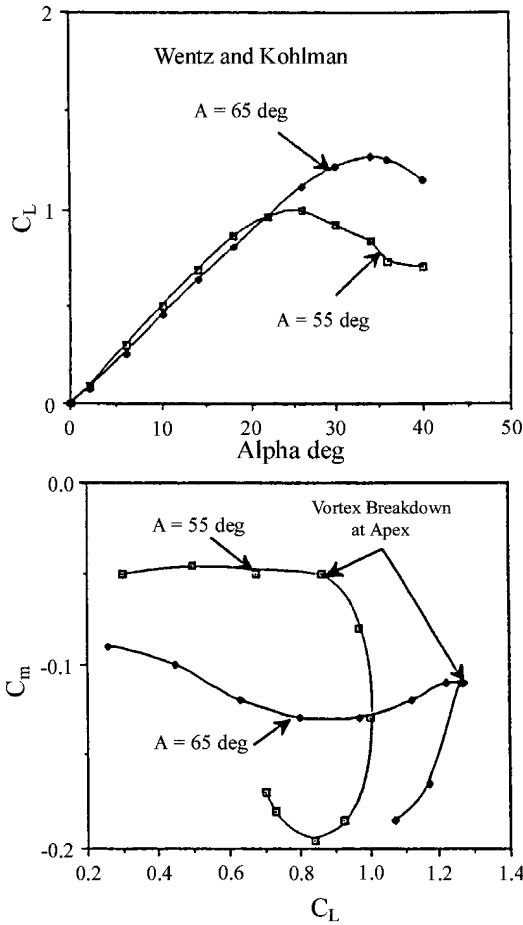


Fig. 30. Lift and pitching moment characteristics for two delta wings, $A = 55^\circ$ and $A = 65^\circ$ [10].

Ways to predict loads acting on a delta wing have been the subject of several investigations in the past decades. Polhamus [100,101] came up with a method, based on the leading-edge suction analogy, for predicting airloads on a delta wing at low angles of attack when vortex breakdown is not present on the wing. The technique is not valid in the presence of vortex breakdown. Purvis [102] used this technique with an assumed pressure distribution based on linear theory results to predict lift, induced drag and pitching moment for several wing geometries also in the absence of vortex breakdown. His predictions showed very good correlation with experiments.

In an effort to include the effects of vortex breakdown in numerical load predictions, Huang and Hanff [92] extended the leading-edge suction analogy by using the instantaneous location of vortex breakdown and by including motion-induced modifications to the vortex strength. They used a semi-empirical pressure model to predict airloads during large-amplitude rolling motions.

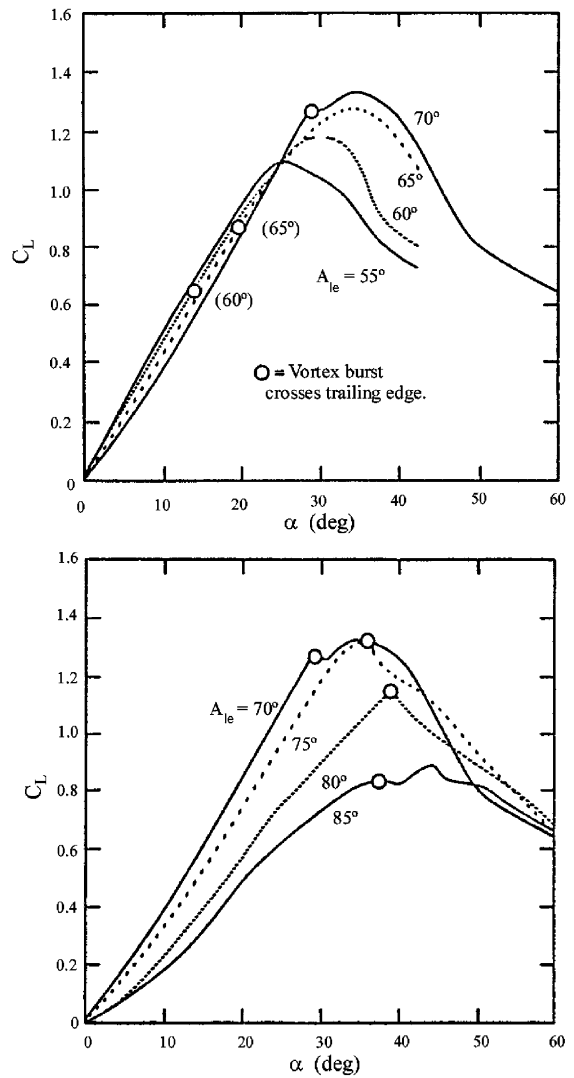


Fig. 31. Lift coefficient for a family of flat plate delta wings [89].

In order to include vortex breakdown effects into load predictions, the location of breakdown must be known which implies vortex breakdown prediction. Huang et al. [103] showed the importance of the dynamic response of the leading-edge vortex breakdown on the nonlinearities observed in airloads. Huang and Hanff [92,104] assumed in their vortex breakdown model that the instantaneous location of vortex breakdown can be represented by the sum of three terms: a static term, a second term representing quasi-steady effects and a third term for unsteady effects. Fig. 32 shows that their static vortex breakdown prediction gave very good agreement with experimental data. With their model for vortex breakdown, they were able to predict airloads for static and dynamically rolling delta wings, as shown in Figs. 33 and 34.

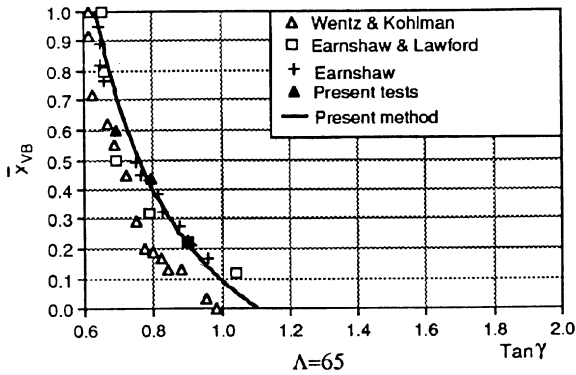


Fig. 32. Vortex breakdown location prediction on a 65° delta wing [92].

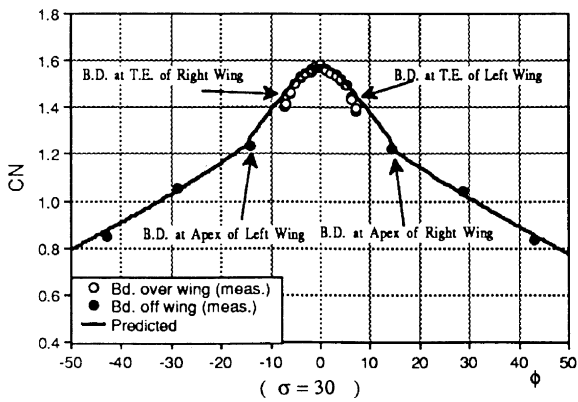


Fig. 33. Static normal force coefficient for rolled 65° delta wing [92].

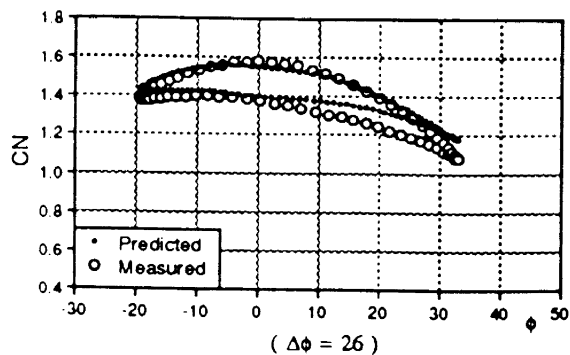


Fig. 34. Instantaneous normal force coefficient on a rolling 65° delta wing [92].

2.3. Reynolds number effects

There is evidence that the Reynolds number has an effect on the qualitative features of the flow in the

presence of leeside leading-edge bevels and centerbodies [105,106]. In the absence of centerbodies, most researchers agree that many of the qualitative features of the flow are usually independent of Reynolds number. This is particularly true for wings with sharp leading edges. For example, the position of vortex breakdown does not appear to have any strong Reynolds number sensitivity in these cases. Erickson has compared experimental measurements of vortex breakdown over a wide range of Reynolds numbers. The lack of Reynolds number sensitivity is due to the fact that the models have sharp leading edges, thereby fixing the point of separation. There are, however, differences in the flow structure that are attributable to Reynolds numbers. For instance, the position of the vortices is affected by the Reynolds number. Pressure distributions show the relative positions of the primary and secondary vortices by way of the suction peaks. The suction peak is higher for the turbulent flow case. As the Reynolds number increases, the primary vortex moves outboard due to the Reynolds number influence on the secondary vortical flow. The influence of Reynolds number on the other properties of the flow field such as circulation or vorticity is unknown.

2.4. Mach number effects

The flow above a delta wing at supersonic speeds can be very similar to that discussed so far provided that the flow at the leading edges is subsonic. When the leading edges are supersonic, shock waves can occur on the leeward surface. Fig. 35 is a sketch based upon the observations of Stanbrook and Squire [107] of two types of flow fields that may occur at supersonic speeds. When the flow normal to the leading edge is subsonic, the leeward flow pattern is identical to the flow patterns described earlier. At low angles of attack, the flow is completely attached on the leeward side; however, at higher angles of attack, the flow again separates at the leading edge to form the leading-edge vortices observed at low speeds. As the freestream Mach number is increased, the component of the flow normal to the leading edge may become supersonic. In this case, the leeward wake patterns are quite different, as shown in Fig. 35b. At low angles of attack, after the supersonic flow expands over the leading edge, it is turned downstream resulting in shock waves between the leading edges and the wing centerline. These shock waves run from the apex to the trailing edge. Because the shocks are weak, the boundary layer flow remains attached. At higher angles of attack, the shock waves are strong enough to cause the boundary layer flow to separate. Miller and Wood [108] presented a detailed classification of the leeside flow fields above thick delta wings at supersonic speeds.

Donehoe [109] conducted an extensive experimental investigation on a 65° delta wing at high subsonic Mach

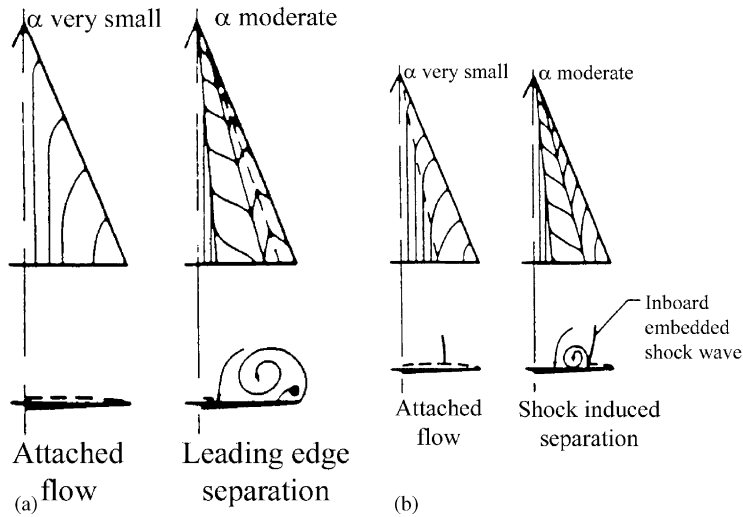


Fig. 35. Leeward flow models [107]: (a) subsonic leading edge, and (b) supersonic leading edge.

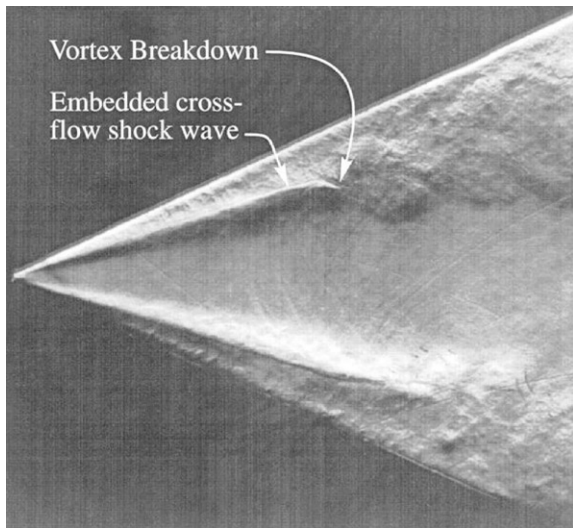


Fig. 36. Shadowgraph picture of the vortical structure above a 65° swept delta wing ($M_\infty = 0.6, \alpha = 20^\circ$) [109].

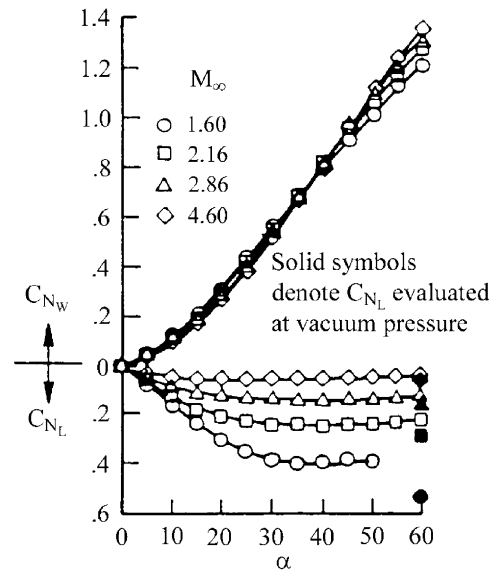


Fig. 37. Normal force coefficient, AR = 1.0 [110].

numbers in order to provide new insight into the complex flow fields acting over a delta wing at high subsonic speeds. The presence of shocks was shown to influence the mode of secondary separation. Furthermore, vortex breakdown and its associated surface pressure distribution were significantly affected by the terminating shock wave, or trailing-edge shock wave, which is typical on a delta wing in high subsonic flow regime.

Fig. 36 is a shadowgraph picture of the vortex flow above a 65° delta wing. The location of an embedded crossflow shock wave and vortex breakdown are noted

on the photograph. The flow image appears to indicate that vortex breakdown is of the spiral type.

The aerodynamic coefficients are affected by Mach number, as shown in Fig. 37. As the Mach number increases, the normal force coefficient decreases. The reason for the decrease in normal force coefficient is explained by Stallings [110] by examining the pressure data from which the force coefficients were obtained. The contribution to the normal force coefficient of the leeward and windward sides were obtained separately and are included in Fig. 37. The subscripts, W and L , refer to the windward and leeward contributions

respectively. As the Mach number is increased, the leeward side contribution to the normal force coefficient decreases, whereas the windward side contribution increases with Mach number for the higher angles of attack. There is a net decrease in the normal force with increasing Mach number since the increase on the windward side is much less than the decrease on the leeward side.

2.5. Summary

The leading-edge vortex structure above a delta wing and its influence on the delta wing aerodynamics has been reviewed in this section. A summary of the major features of the leading-edge vortex structure and their effect on the aerodynamics of the wing are summarized below.

The strength of the leading-edge vortices depends upon the angle of attack and the wing leading-edge sweep angle. For a given angle of attack, the strength decreases with increasing sweep angle. The circulation of slender delta wings can be scaled with the Hensch and Luckring correlation parameter developed from slender body theory.

The velocity field associated with a leading-edge vortex can be characterized as the superposition of a jet flow and vortical flow. The maximum axial velocity occurs at the vortex center and can be as much as two or more times the freestream velocity. The extent of the jet-like flow (i.e. velocity greater than the freestream) can be as much as 30% of the local semi-span. The maximum tangential velocity can reach approximately 1.5 times the freestream. The core (viscous subcore) defined by the distance between the peak tangential velocities is smaller than the jet core. The jet core increases in size with angle of attack while the subcore remains nearly constant in size over the wing.

The vorticity distribution through the leading-edge vortex is primarily in the axial direction prior to breakdown. Most of the axial vorticity is found within the viscous subcore. The radial and azimuthal vorticity components are small before breakdown. When spiral breakdown occurs, the core flow is deflected into a spiral geometry having the opposite sense of that of the circulation. The axial vorticity is reduced substantially and a large negative azimuthal vorticity is present after breakdown. The large negative azimuthal vorticity is consistent with the requirement to sustain the vortex breakdown.

The pressure gradient along the vortex axis is a major factor in causing breakdown. The pressure gradient can be thought of as being created by the external flow and by a self-imposed component that is a function of the vortex strength.

The leading-edge vortices contribute a substantial portion of the lift generated by slender delta wings. The

primary vortices produce large suction peaks on the upper surface pressure distribution prior to breakdown. After breakdown reaches the wing, the suction pressure peaks are reduced aft of the breakdown location. The modification of the pressure field affects the lift and moment characteristics of slender delta wings.

3. Unsteady slender wing aerodynamics

An unsteady motion of a delta wing results in a modification of the flow field in response to the maneuver. As was mentioned earlier, this can result in delays of flow separation and vortex formation at low angles of attack, and changes in vortex location and the onset of breakdown at higher angles of attack. During oscillatory or periodic motions, a hysteresis develops in the positions of the vortex core and the vortex breakdown relative to the static locations. Due to this hysteresis in the flow field, there is a corresponding modification of the aerodynamic loads on the delta wing. The results presented in the following section are used to show the importance of flow field hysteresis in either vortex position or breakdown on the unsteady loads and surface pressure distributions of simple delta wing planforms. A detailed review of the flow physics of pitching delta wings is given by Rockwell [111]. Moreover, investigators have tried to explain the effect of wing motion on vortex breakdown by looking at an induced camber effect [112–117]. For instance, due to induced camber effect, the angle of attack at the apex of a delta wing during a pitching maneuver would be different than the angle of attack at the trailing edge. These different angles of attack would have an effect on the location of vortex breakdown over the wing. The reader is referred to the work by Ericsson [113–117] for more details on the induced camber effect.

Ashley et al. [118] have published a paper summarizing the current state of unsteady swept-wing aerodynamics research. Theoretical, computational and experimental research involving both flow field behavior and aerodynamic forces and moments are described and representative data are presented. Ashley et al. concluded that for unsteady maneuvers where vortex breakdown is not present, quasi-static behavior results. However, for ranges of motion where breakdown is present over the wing, hysteretic behavior is seen and transient effects can become important.

For a dynamically pitching wing, it is possible to delay the detrimental effects of breakdown. A substantial overshoot in the aerodynamic forces is typically seen for oscillatory or transient pitching maneuvers.

The next section will present a brief review of the current understanding of the effect of large angle-of-attack unsteady motions on the aerodynamic and vortical wake characteristics. The discussion will

emphasize the fluid mechanic mechanisms governing the nonlinear aerodynamic loads. The relationship between force and moment coefficients, surface pressures and the flow field structure will be emphasized.

3.1. Aerodynamics of a pitching delta wing

Unsteady force measurement on delta wings are a relatively new area of research, but the limited number of studies that are available have documented the hysteretic nature of the forces and moments. Bragg and Soltani [119] conducted an experiment using a 70° swept wing oscillating in pitch. Hysteretic behavior was noted in the dynamic loads, the amount of which was a function of the pitch rate. This was also seen by both Brandon and Shah [120] and Jarrah [121]. Brandon and Shah examined the effects of both sinusoidal and ramp pitching motions. They reported a large overshoot of the forces relative to the steady state values. They also suggested that this may be due to a lag in the separation and reattachment of the leading-edge vortices during the dynamic maneuver. Jarrah [121] utilized delta wings with aspect ratios of 1, 1.5, and 2, and angle of attack ranges of 0–30° and 0–60°. He saw a large overshoot in the aerodynamic coefficients for the 0–60° motion, and noted that this overshoot was a function of the aspect ratio as well as the pitch rate. Fig. 38 is an example of Jarrah's data that clearly shows the large aerodynamic hysteresis for a reduced (nondimensional) frequency $k = 2fc/U_\infty = 0.03$.

Unsteady delta wing research has shown the force and moment coefficients to overshoot or undershoot the static values depending on both the type of unsteady maneuver and the motion history. For example, if the model pitches from 0° to 45°, the peak overshoot in C_N will be higher than if the model pitches from 25° to 45° [120]. An example of the dynamic normal force

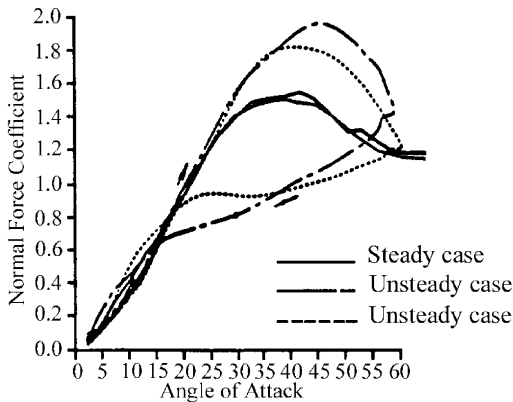


Fig. 38. Unsteady aerodynamic coefficients for a slender delta wing. Aspect ratio = 1.0. $k = 0.03$, $Re = 635,000$. Pitch amplitude = 0–60° [121].

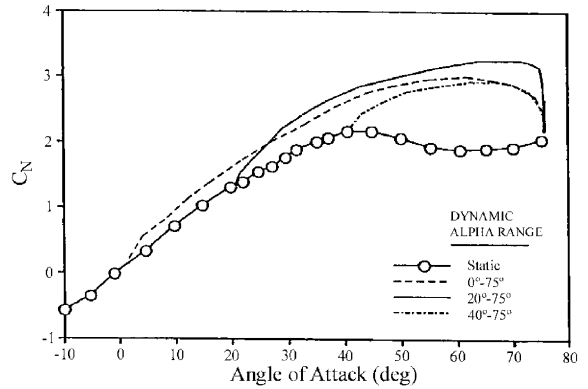


Fig. 39. Dynamic lift overshoot of a slender delta wing. Leading-edge sweep angle = 70° [120].

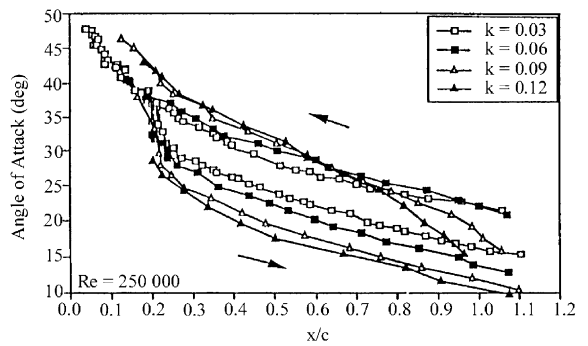


Fig. 40. Breakdown location for 2–60° oscillation. Four pitch frequencies are shown [122].

coefficient for a pitching delta wing is shown in Fig. 39 along with the static curve. This data was obtained by Brandon and Shah [120] using a force and moment balance to measure the dynamic loads on a pitching delta wing.

3.1.1. Vortex breakdown

Additional insight into the mechanisms causing the dynamic loads can be obtained by examining the dynamic characteristics of vortex breakdown and the unsteady pressure acting on the wing in a dynamic motion [123–127,122]. Thompson [127] studied the unsteady aerodynamics of a delta wing undergoing a large amplitude motion. Fig. 40 shows unsteady breakdown location data obtained from a flow visualization experiment of a 70° swept delta wing undergoing large amplitude pitching motions. The wing was pitched from 0° to 60° angle of attack in a sinusoidal manner. The breakdown location is shown as a function of instantaneous angle of attack for four nondimensional pitching frequencies. The arrows in Fig. 40 indicate the direction of motion (angle of attack increasing or decreasing). The

steady breakdown location data has not been shown in order to maintain clarity. However, it should be noted that the unsteady data bracketed the steady state breakdown location. The hysteresis, which is characteristic of unsteady high angle-of-attack delta wing aerodynamics, can be seen in Fig. 40. At a given instantaneous angle of attack, the difference in breakdown location is as much as $0.45c$, depending on the direction of motion. The size of the hysteresis loop increases with increasing reduced frequency. At very high angles of attack, over 50° , the flow over the wing becomes fully separated, similar to a bluff-body flow. Thus, breakdown does not exist. As the wing pitches down, the leading-edge vortex system reforms with breakdown near the apex. Breakdown then moves aft as the angle of attack continues to decrease.

These data illustrate the lags that develop for the unsteady case. For the upward motion, there is a lag in the development of the vortex core and the upstream progression of vortex breakdown. For the downward motion, there is a lag in reformation of the vortex system (from fully separated flow conditions) and thus in the downstream progression of vortex breakdown. These lags give rise to the large unsteady effects seen in the aerodynamic loads on the wing.

Fig. 41 shows an example of the unsteady pressure data as a function of instantaneous angle of attack, along with the steady data. This data is for a single surface pressure tap located at $x/c = 25\%$ and located beneath the primary vortex. The location of vortex breakdown has been noted at specific points along the

curve. As the angle of attack increases, the pressures uniformly decrease. With the occurrence of breakdown on the wing the pressure gradient begins to decrease. Further increase in angle of attack moves the breakdown to the apex. This precedes the total separation of the leeward side, and, as a result, the pressures begin increasing due to the lack of an organized flow structure over the wing. However, before the pressure field can become relatively uniform (as for the steady high angles of attack case), the wing pitches down again, until the point is reached at which the leading-edge vortex structure reforms (with breakdown near the apex). Thus a pressure recovery begins and the pressures begin decreasing. Breakdown then moves down the length of the wing and into the wake. Concurrent with this behavior of the vortex is a partial recovery of the suction pressures. Further decrease in angle of attack results in a collapse of the vortex system and the vortex-induced pressure field.

The pitching tests conducted over an angle of attack range of $0\text{--}30^\circ$ showed very little hysteretic behavior. The surface pressures oscillated in phase with the model motion, and reached minimum values as the wing reached its maximum angle of attack. The pressures showed little deviation from the static values during the unsteady motion. These trends were apparent for both the reduced frequencies tested, and no apparent difference existed due to the change in pitch rate. The pressure data was seen to have similar general characteristics as normal force data obtained from the literature.

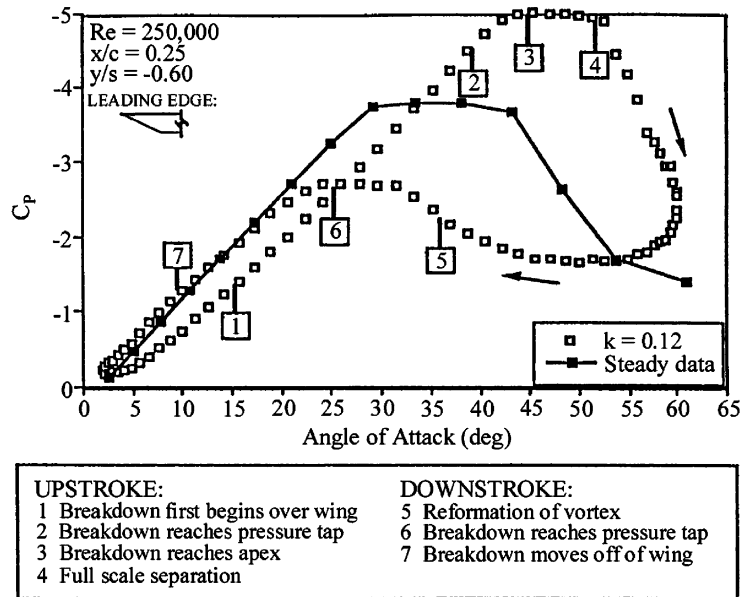


Fig. 41. Unsteady surface pressure data for $2\text{--}60^\circ$ oscillation. Chordwise progress of vortex breakdown (from flow visualization tests) also noted [122].

For the larger pitching range of 2–60°, large overshoots in the unsteady pressure coefficient were seen. The unsteady pressures follow the steady pressures on the upstroke, then continue to decrease as angle of attack increases for an additional 10–15°. On the downstroke, the upper surface continues to show full separation to an angle of attack where, for the steady case, coherent leading edge vortices exist. This results in an undershoot of the downstroke pressures relative to the steady pressures. When this is considered along with the large overshoot on the upstroke, a significant hysteresis is observed for the unsteady pressures, with upstroke pressure coefficients being as high as 2.5 times the downstroke values. This data was also seen to qualitatively compare with the normal force data for a wing of similar aspect ratio.

The constant chord data showed similar trends as the constant span data. Large hysteresis loops were seen at span locations at or near the suction peak. The static data showed this suction peak to exist from 60% to 70% of the local semi-span, depending on the angle of attack. This was also the case for the dynamic motion, where a hysteresis was seen in the suction peak; the location of the peak was seen to be a function of the direction of instantaneous model motion.

3.1.2. Summary

For large amplitude pitching motions, the aerodynamic characteristics of delta wings are quite different from what would be predicted from static measurements. The unsteady lift or normal force curves are similar to the dynamic stall curves observed on pitching airfoils. As the delta wing pitches up, vortex breakdown lags behind the motion of the wing allowing the wing to achieve a higher lift coefficient than the static case. Eventually vortex breakdown reaches the apex of the model resulting in a completely separated flow field. As the model begins to pitch down, there is a delay in the reestablishment of the leading edge vortices and vortex breakdown. Again, the flow field lags behind the motion of the wing and a hysteresis loop in the aerodynamic load occurs. The magnitude of the hysteresis loop depends on the reduced frequency of the motion and the magnitude of the oscillation amplitude. If the model is oscillated over an angle of attack range in which vortex breakdown does not occur, the aerodynamic characteristics are quasi-static.

3.2. Wing rock motion of slender delta wings

As noted in the introduction, wing rock can severely limit the pilot's ability to perform a tracking task. The pilot senses wing rock as a rolling oscillation. However, in most cases, the motion is more complicated than just a pure rolling motion. The wing rock motion may result in a combined rolling and yawing motion or a Dutch roll

motion. The flow mechanisms that cause wing rock are thought to be due to unsteady interactions of the vortical flow field above the aircraft at high subsonic speeds and to unsteady shock induced separation at transonic Mach numbers.

3.2.1. Plain delta wing

To provide a background of the importance of unsteady aerodynamics to the wing rock motion, a review of the wing rock motion on simple flat plate delta wings is presented. The emphasis of this discussion will be on the flow mechanisms responsible for the wing rock motion. A more detailed review of wing rock is presented by Katz [128].

Arena [129,130] conducted a very thorough experimental study of the wing rock motion on a flat plate delta wing. This study provides an interesting example of the importance of unsteady aerodynamics on the wing rock motion. What makes the study unique is the measurement of the unsteady aerodynamics, surface pressures, and off-surface location of the leading-edge vortices in combination with a numerical simulation of the wing rock motion. Because of the completeness of this study, it will be used as an example of how the unsteady aerodynamic characteristics contribute to the wing rock motion of a simple wing planform such as a delta wing.

Slender flat plate delta wings having leading-edge sweep angles greater than 76° have been observed to exhibit a limit cycle roll oscillation at angle of attack. This limit cycle rolling oscillation is commonly called "wing rock". By definition, a limit cycle motion is one that reaches a steady state oscillation independent of the initial conditions. Fig. 42 is an example of the limit cycle rolling motion of an 80° delta wing measured on a free-to-roll system incorporating an air bearing by Arena [129]. The wing rock roll angle amplitude increases with increasing angle of attack, as illustrated in Fig. 43. When vortex breakdown starts occurring over the wing above $\alpha = 35^\circ$, the amplitude drops sharply.

The wing rock motion was analyzed by obtaining angular velocity and rolling moment information from the roll angle time histories. This information was very useful in studying the limit cycle behavior of the motion. The determination of $\dot{\phi}$ and $\ddot{\phi}$ involved a two step data reduction process. First, the roll angle time history data was low pass filtered. This was necessary to remove the digital "steps" in the data which would manifest itself as high frequency noise when differentiated. Central differencing schemes were then used to determine $\dot{\phi}$ and $\ddot{\phi}$. Validation of this method may be found in Ref. [129].

The calculation of C_l is made simple by the fact that the model is constrained to one degree of freedom. The equation of motion for the system is

$$I_x \ddot{\phi}(t) = \sum L_R(t), \quad (8)$$

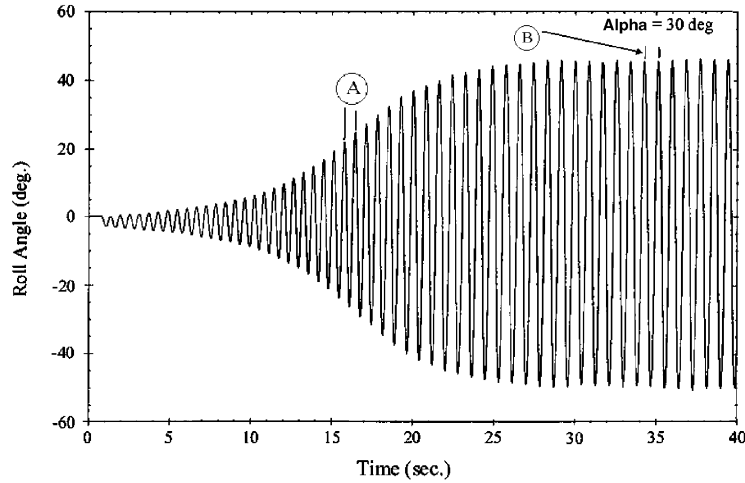


Fig. 42. Wing rock buildup, $\alpha = 30^\circ$ [129].

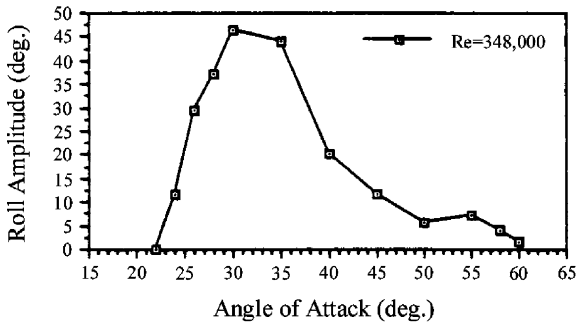


Fig. 43. Wing rock amplitude vs. angle of attack, $Re = 348,000$ [129].

where the sum of roll moments is $\sum L_R = L_{aero} + L_{bearing}$.

With the use of an air bearing apparatus, the torque due to the bearing friction may be neglected, effectively isolating the aerodynamic effects of the wing. In coefficient form, the equation may be written as follows:

$$C_l(t) = \frac{I_x \ddot{\phi}}{q_\infty S b} \tag{9}$$

Using a torsional pendulum technique, the rotational moment of inertia, I_x , was found. With this result, the aerodynamic rolling moment coefficient C_l could then be easily calculated.

With C_l known, the energy exchange technique used by Nguyen et al. [131] is helpful in analyzing the mechanisms driving the limit cycle oscillation. For the single degree-of-freedom motion, the energy is equal to the applied torque times the angular velocity. The energy added to or extracted from the system during the motion for a specific time interval can be

expressed as

$$\Delta E = q_\infty S b \int_{t_1}^{t_2} C_l(t) \dot{\phi} dt. \tag{10}$$

This expression for the energy exchange may be written in a more convenient form by rewriting the equation in terms of the instantaneous roll angle $\phi(t)$:

$$\Delta E = q_\infty S b \int_{C_\phi} C_l[\phi(t)] d\phi, \tag{11}$$

where C_ϕ is the curve obtained by plotting C_l as a function of the instantaneous roll angle $\phi(t)$ for a given time interval. The physical interpretation of Eq. (11) is that the energy exchanged in a cycle of motion is directly related to the area enclosed by the rolling moment curve. When the loop encloses an area in a clockwise sense, energy is being added to the system, whereas counter-clockwise loops indicate that energy is being dissipated from the system. Fig. 44 is a graphical representation of the energy for several different rolling motions.

Fig. 42 presents a time history of wing rock buildup for $\alpha = 30^\circ$. A buildup cycle and a steady state cycle were singled out for a more detailed analysis as cycle A and cycle B. The dynamic roll moment characteristics of the buildup cycle (cycle A) is seen in Fig. 45. Note the clockwise loop in the plot which indicates a dynamic instability, and that the restoring moment is roughly linear with roll angle. Energy is being fed to the system; therefore, the roll angle amplitude is increasing. The loop is very thin which accounts for the fact that the buildup happens very slowly. Fig. 46 is the analogous plot of the roll moment coefficient after the system has reached steady state (cycle B). The unstable region of the plot still exists between -20° and 20° , but two stable damping “lobes” have formed for the larger roll angles. The area of these lobes equals the area of the unstable

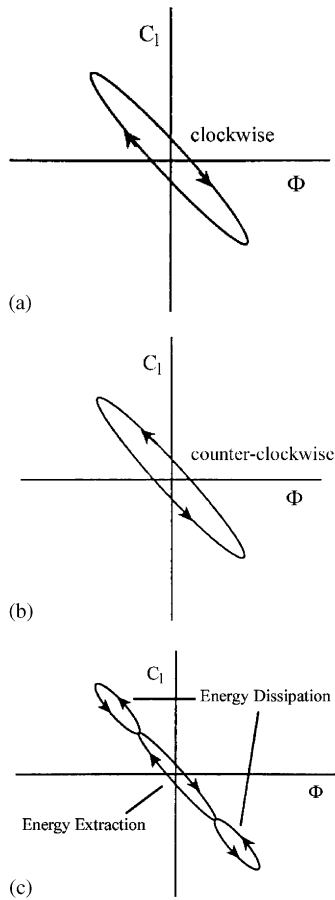


Fig. 44. Conceptual C_1 vs. ϕ curves showing energy exchange (arrows indicate direction in time) [129]. (a) Unstable cycle (energy extracted from free stream). (b) Stable cycle (energy dissipated from system). (c) Typical limit cycle (net energy exchange = 0).

portion of the plot such that the net energy exchange is zero. This condition is necessary for the limit cycle oscillation to be sustained.

As was mentioned earlier, vortex position above a delta wing is a function of roll angle (or sideslip). Jun and Nelson [132] have experimentally shown a dependence of vortex position vs. roll angle for an 80° sweep delta wing. The results indicate that the static and dynamic vortex trajectories differ greatly. The dynamic position of the vortices exhibits a time lag phenomenon which accounts for the appearance of hysteresis. Time lag in vortex position has also been seen in numerical simulations by Konstadinopoulos et al. [133] using an unsteady vortex lattice model coupled with a single degree-of-freedom equation of motion, and has been suggested with analytical arguments by Ericsson [134]. As mentioned before, the vortex position above a delta

wing greatly affects the pressure distribution and it is thought that the movement of the leading-edge vortices may be a driving mechanism in the wing rock motion. The purpose of Arena's experiments [130] was to correlate the position of the leading-edge vortices with the model motion during wing rock to determine the effect of dynamic vortex movement on the model motion. With the experimental apparatus developed for his study, the vortex position during wing rock could be related to time, roll angle, angular velocity, and rolling moment. The angle of attack chosen for these experiments was 30° . The reason for this choice is twofold. First, since wing rock is present even in the absence of vortex breakdown, the fundamental mechanisms causing the motion can be further isolated by operating at an angle of attack where breakdown is not seen. Secondly, $\alpha = 30^\circ$ yields the largest roll excursions, hence the motions of the vortices are large in amplitude which reduces the percentage of error when digitizing the video images of the vortices. Steady vortex experiments were conducted first for a comparison with the unsteady results. Left and right vortex position refers to a view from the trailing edge of the wing. The static results show that as one side of the wing moves downward, its associated vortex moves inward both spanwise and normally, and vice versa on the upward wing. When vortex position is analyzed during wing rock, the results differ greatly from the static case. Figs. 47a and b show the normal and spanwise static positions of the vortices and the position during two steady state cycles of wing rock. The normal dynamic position of the vortices exhibits a large hysteresis loop whereas none is discernible in the spanwise position of the vortices. Note that use of the word normal refers to a coordinate system that rotates with the wing; hence normal distance is the distance perpendicular to the plane of the wing surface.

Since asymmetry in vortex position is one of the factors that will contribute to the rolling moment, a method was developed for interpreting the data which quantifies the normal and spanwise vortex asymmetries. Fig. 48 is a sketch of asymmetric vortex position used to define asymmetry parameters Δy and Δz . The parameter Δz is a measure of the normal asymmetry between the two vortices and is defined such that a positive Δz will favor a positive rolling moment. Similarly, the parameter Δy is a measure of the spanwise asymmetry of the vortices and is defined such that a positive Δy will favor a positive roll moment (assuming y/s is not greater than 1). The asymmetry parameters are defined as follows:

$$\Delta z = z_r - z_l, \tag{12}$$

$$\Delta y = |y_l| - |y_r|. \tag{13}$$

While Δz and Δy indicate the direction of the contribution to rolling moment due to vortex position

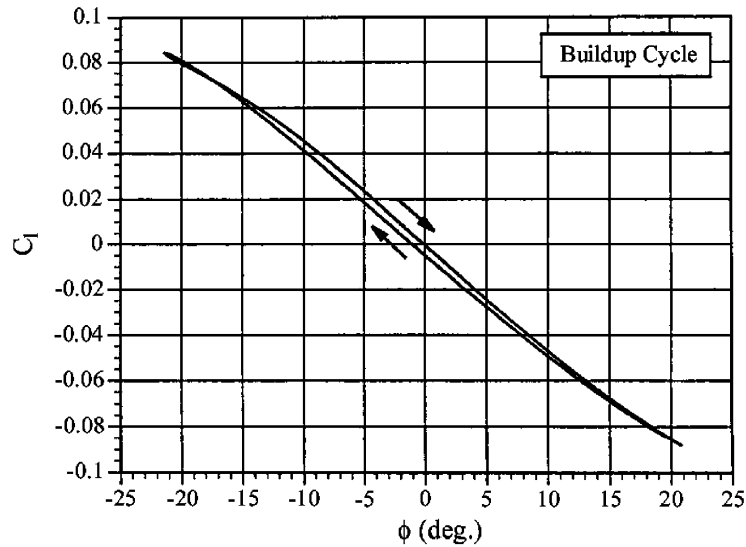


Fig. 45. Roll moment coefficient for a cycle of wing rock buildup [130].

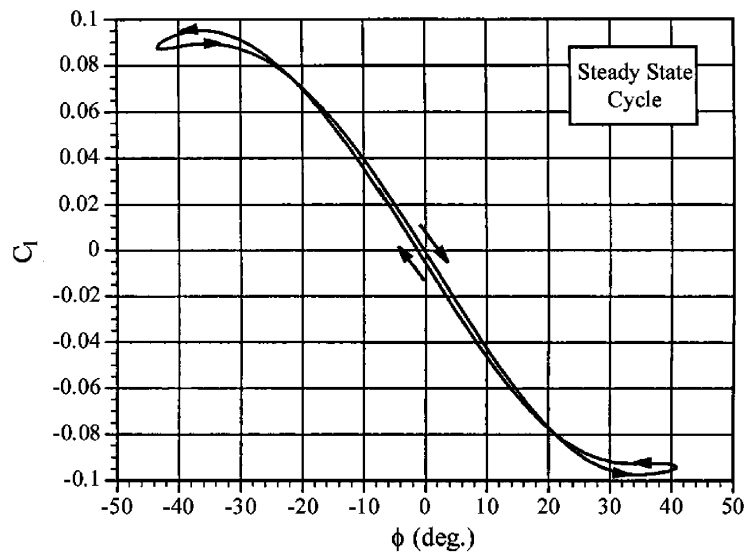


Fig. 46. Roll moment coefficient for a steady state cycle of wing rock [130].

asymmetry, the actual magnitude of their contributions is unknown.

Figs. 49a and b are plots of Δz and Δy for the static case and for the two steady state cycles of wing rock introduced earlier. The static normal asymmetry is seen to contribute to a restoring moment since the downward wing vortex is closer to the wing surface than the upward wing vortex. The static spanwise asymmetry can be seen to contribute to a roll moment in the opposite sense since the downward wing vortex moves closer to the root chord, and the upward wing vortex moves away

from the root chord. However, the contribution from spanwise asymmetry in vortex position to roll moment must be dominated by the contributions from normal asymmetry and vortex strength asymmetry for the static restoring moment to be produced. Also note that there is hysteresis in vortex position asymmetry confined to the direction normal to the wing, which is consistent with the fact that the time lag in vortex movement is confined to the normal direction.

If restoring and positive damping moments alone were present, the wing would damp out in time if

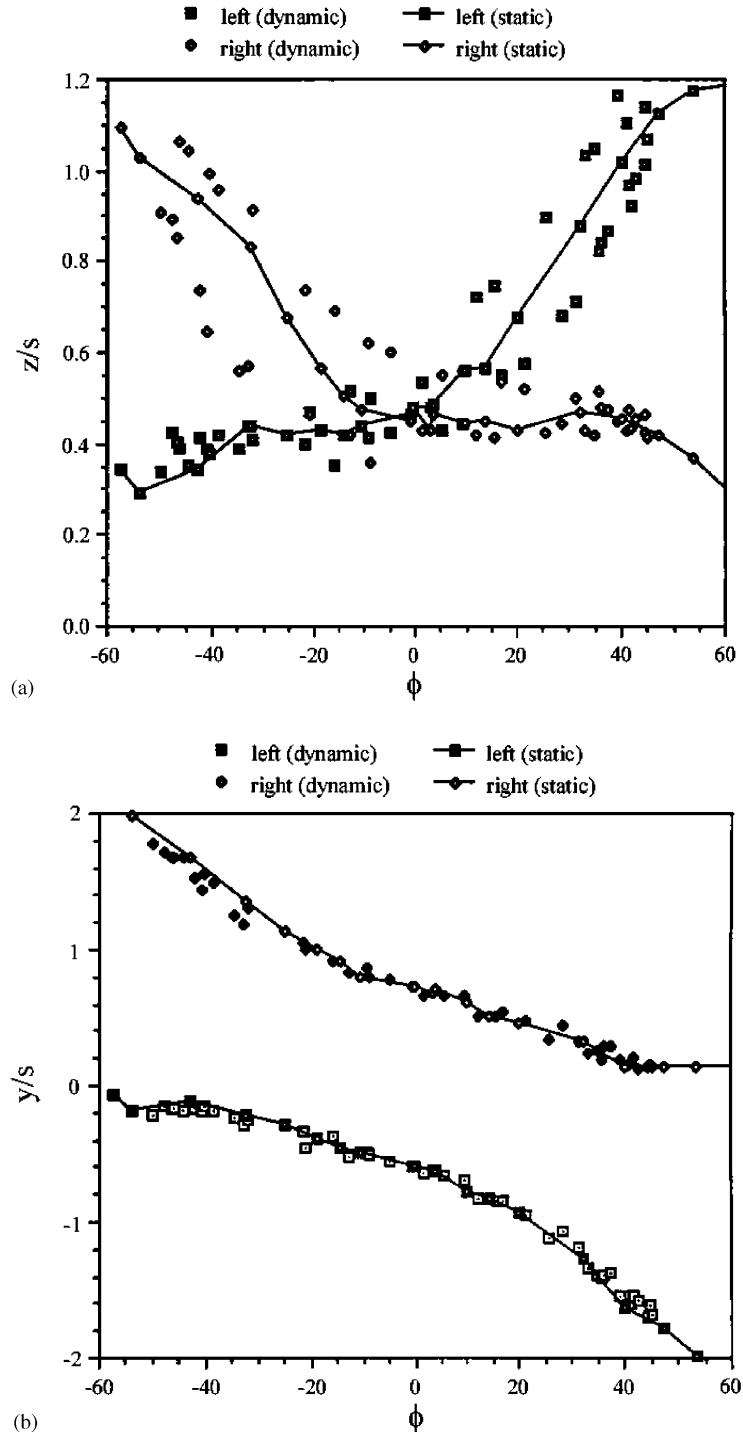


Fig. 47. Vertical and spanwise vortex position during wing rock [129]. (a) Vertical position. (b) Spanwise position.

perturbed. Therefore there must be an aerodynamic phenomenon that generates a destabilizing moment during wing rock. Likely candidates for the mechanisms responsible for the destabilizing moment include the

time lag in vortex position and/or a time lag in vortex strength. In Arena's experiments, only the *contribution* to roll moment from the lag in vortex position could be analyzed.

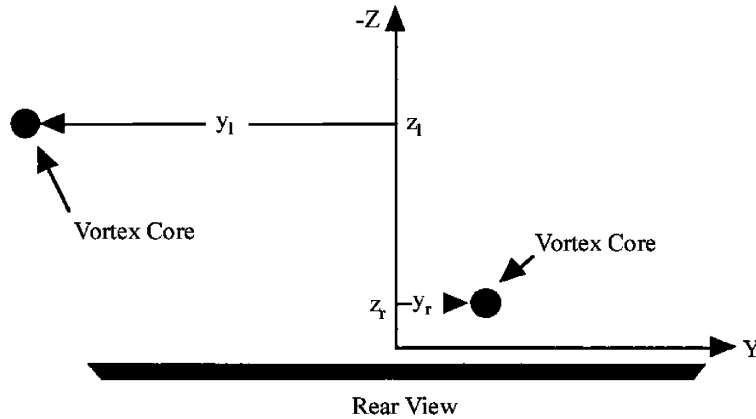


Fig. 48. Sketch of asymmetric vortex position [129].

The hysteresis phenomenon seen in Figs. 47 and 49a can alone provide the instability necessary to sustain the wing rock motion if a time lag in vortex strength is not present. With no significant time lag in vortex strength, vortex strength asymmetry will only contribute to a restoring moment and not the destabilizing moment necessary to sustain wing rock. In Fig. 47, the time lag on the upward going vortex is seen. Fig. 49a shows that due to the time lag of the upward going vortex, a switch to a restoring moment contribution from the normal vortex position asymmetry does not occur until approximately 20° for positive roll rates, and approximately -20° for negative roll rates. This result can be compared to the C_1 vs. ϕ result in Fig. 50 which corresponds to two steady state cycles of vortex motion. It can be seen that the unstable region of the plot lies between -20° and 20° . The lag in asymmetry must be great enough to overcome the roll damping moment which increases for small roll angles due to higher angular velocity. The leveling off of the C_1 vs. ϕ curve is most likely due to the leveling off of the vortex position time histories seen in Fig. 47 when the vortex approaches the wing. These results suggest that the time lag in normal vortex asymmetry due to the upward moving vortex may be a mechanism responsible for wing rock. These results motivated Arena to conduct a further study of the phenomenon by looking at the unsteady surface pressures on the model. The data may be correlated with the motion of the model and the vortices to gain a better understanding of the aerodynamic mechanisms at work. A detailed discussion of the unsteady pressure data on a wing undergoing a wing rock motion can be found in Refs. [130,135].

3.2.2. Vortex breakdown results

In Refs. [129,130], static and dynamic vortex breakdown characteristics during wing rock are presented. In Arena's study, the data is presented in a manner which

reveals the effect of vortex breakdown on the wing rock motion.

As with vortex position, vortex breakdown contributes to a rolling moment on the wing through asymmetry. For this reason, a vortex breakdown asymmetry parameter Δx was defined. If the distance of the breakdown from the apex is greater on the left side of the wing than that on the right, the asymmetry will contribute to a positive rolling moment. Δx was defined such that if the asymmetry favors a positive rolling moment then Δx is positive:

$$\Delta x = x_l - x_r, \quad (14)$$

where x_l and x_r are the chordwise vortex breakdown locations, as seen in Fig. 51, from the apex, of the left and right vortices respectively (as viewed from the trailing edge). Δx was plotted with roll angle to better show the effect of breakdown on the model motion. Fig. 52 shows static and dynamic vortex breakdown parameter Δx vs. roll angle for $\alpha = 40^\circ$. The effect of vortex breakdown on the model is very apparent in this plot. Since the slope of the Δx vs. ϕ curve is positive for all roll angles for the static case, the static data suggests that the effect of vortex breakdown on wing rock is to create a roll divergence. However, the results from the dynamic experiments suggest a very different effect. Due to the large time lag, the effect of dynamic breakdown on the wing is to have a damping effect on the motion. This is due to the fact that the parameter Δx always favors a rolling moment in the opposite direction to the rotation. This analysis cannot give the magnitude of the contribution to the rolling moment of the wing, but it does provide the qualitative insight on how the dynamic motion of the breakdown affects the wing.

As angle of attack increases, the loops in vortex breakdown position become smaller. For example, Fig. 53 is the Δx vs. ϕ plot for $\alpha = 45^\circ$. The static results favor roll divergence, but once again the dynamic

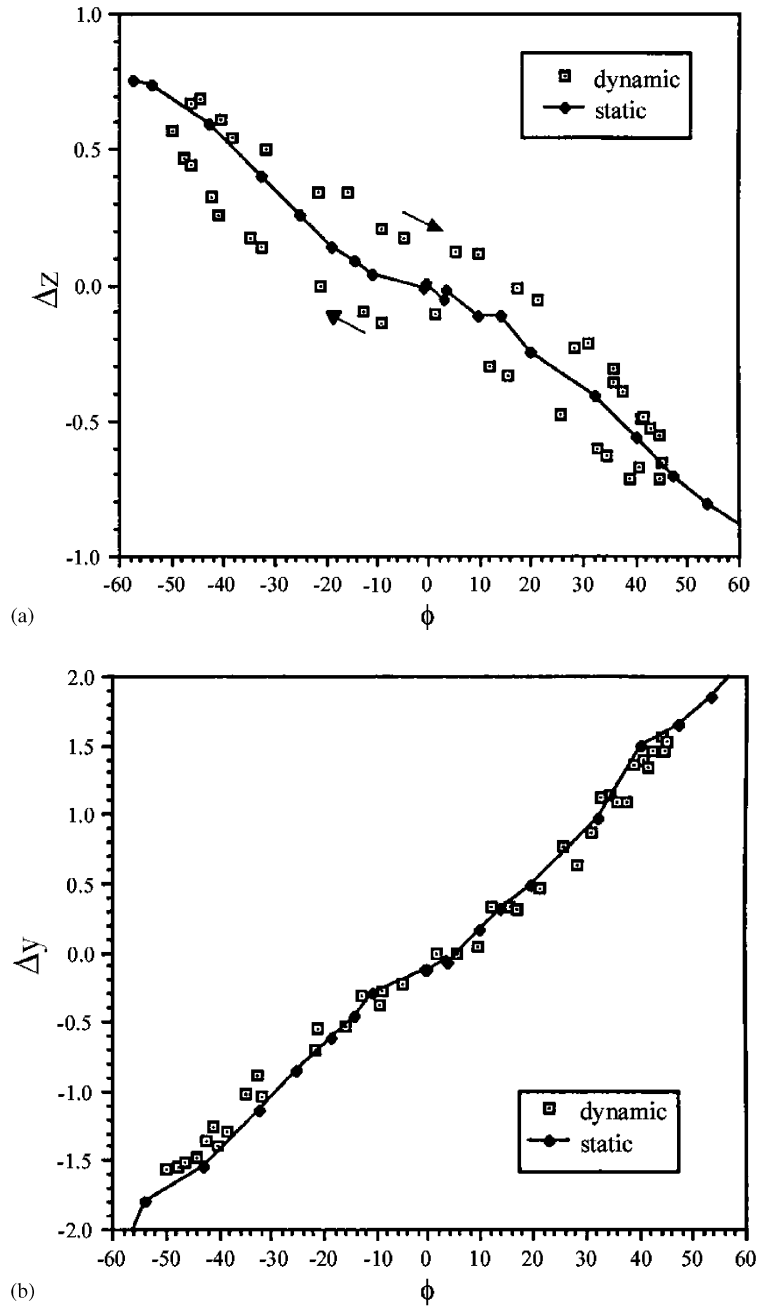


Fig. 49. Vortex asymmetry parameters during wing rock [129]. (a) Δz parameter. (b) Δy parameter.

results indicate damping. It can be seen for the larger roll amplitudes (approximately 8° to 10° and -10° to -12°) that the motion favors roll divergence. This is due again to the fact that as α increases, the time lag decreases, reducing the size of the hysteresis loop. The hysteresis may be better understood by analyzing the loop in section. Starting from point A, the position of the breakdown favors roll damping until point B. At point B the sign of Δx changes and the breakdown

asymmetry favors roll divergence until point C. At point C, the model reverses direction and the position of the breakdown once again favors roll damping until point D. From point D to point A, the breakdown once again favors roll divergence. However, the roll divergence is for just a small portion of the cycle and the majority of the time the breakdown position favors damping.

From Arena's results, it appears that the effect of vortex breakdown during wing rock is to provide

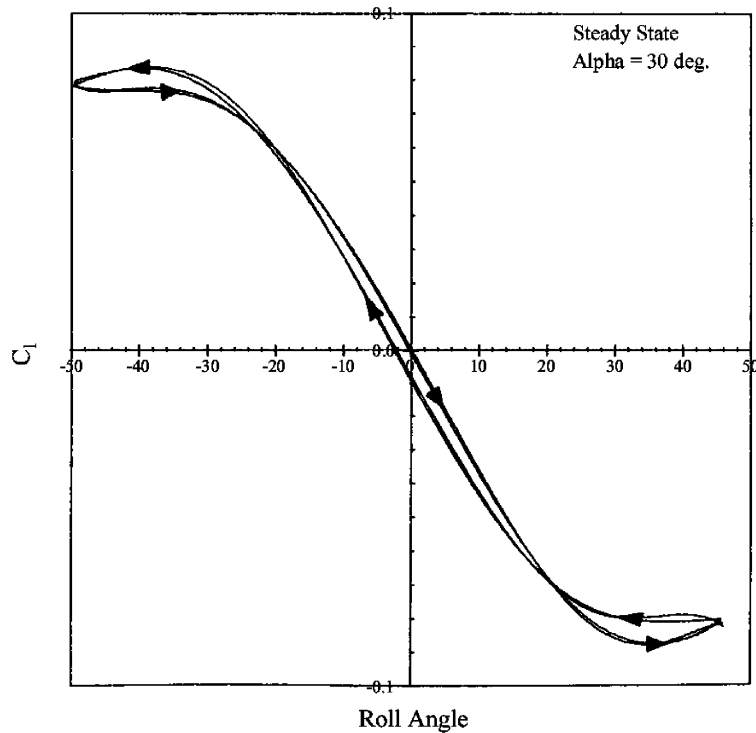


Fig. 50. Two cycles of C_l vs. ϕ for $\alpha = 30^\circ$ [129].

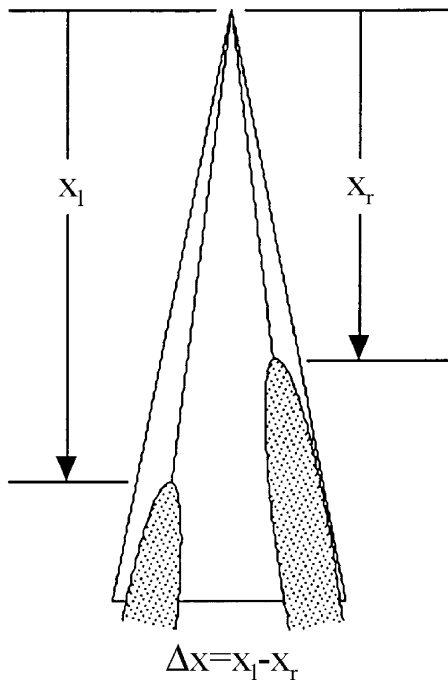


Fig. 51. Sketch of vortex asymmetry used to define Δx [129].

a damping moment. Vortex breakdown did not contribute to roll divergence in Arena’s experiments. It is also clear from the results that extrapolating static vortex breakdown results to the dynamic case may be very misleading.

3.3. Computational model of wing rock

Arena’s experimental study discussed in the previous section provided valuable information on the fluid mechanic mechanisms that cause the wing rock motion of slender flat-plate delta wings. However, Arena’s experimental study was unable to provide information to answer several key questions. The two questions that needed to be answered were as follows. First, what was the effect of the unsteady motion on the vortex strength, and second, what was the mechanism responsible for the damping lobes that are necessary for the limit cycle oscillation? Arena determined that further experimental study could not answer these questions therefore motivating the development of a computational model. The computational model was intended to capture the primary characteristics of the flow field as observed in experiment and to provide additional information on the fundamental flow physics of the problem.

There have been a number of computational studies of wing rock. For example, Konstadinopoulos,

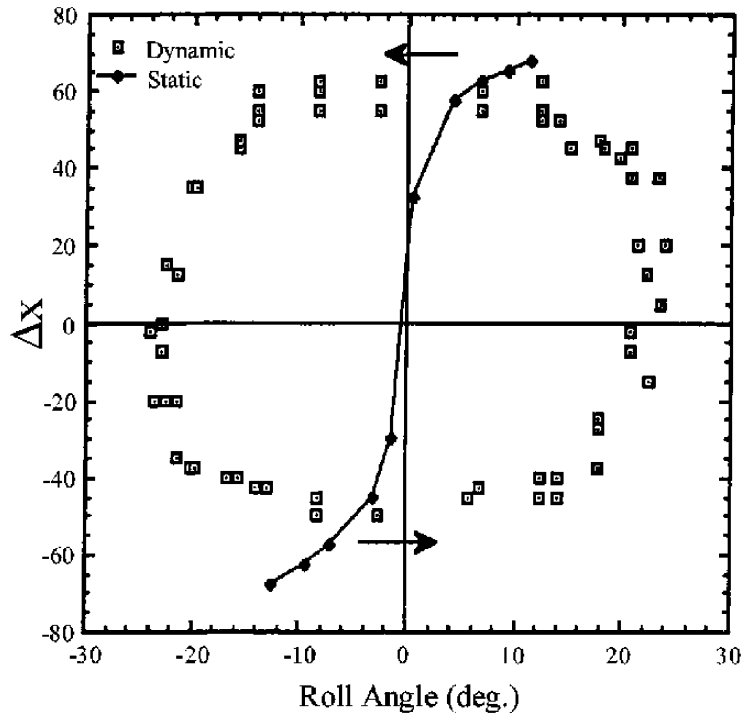


Fig. 52. Breakdown asymmetry parameter Δx vs. ϕ for $\alpha = 40^\circ$ [129].

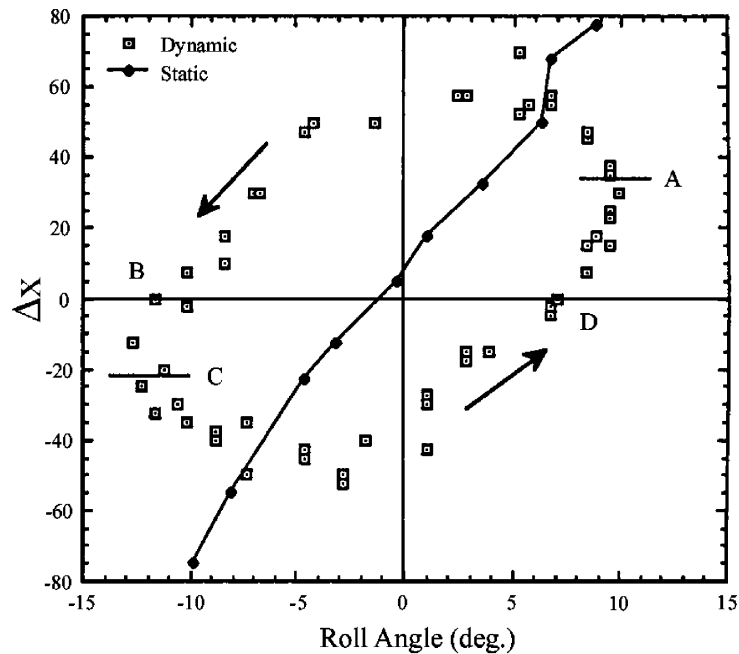


Fig. 53. Breakdown asymmetry parameter Δx vs. ϕ for $\alpha = 45^\circ$ [129].

Mook and Nayfeh [133] have simulated wing rock with the use of a three-dimensional unsteady vortex lattice model coupled with the roll equation of motion. The authors conclude that when angle of attack is

increased beyond a certain angle, the leading edge vortex system becomes unstable which causes a loss of damping in roll which allows the limit cycle motion to occur.

Lee and Batina [136] simulated wing rock of a 75° delta wing with the use of an Euler code. The simulation assumes an unsteady supersonic conical flow field in order to reduce the computational expense of solving the unsteady flow field. The results of the simulations show a definite limit cycle behavior similar to that observed in experiment. The study also provides further evidence that wing rock is an inviscid dominated problem.

These earlier computational studies have shown the feasibility of coupling the solution of the unsteady flow field to the equation of motion in order to capture self-induced oscillations. However, due to the complexity of the models, little additional information has been obtained over that provided by experiment with regard to the mechanisms responsible for wing rock.

The computational model developed by Arena [130] was formulated to provide information on the movement of the leading-edge vortices, vortex strength, and the unsteady surface pressures during a wing rock motion. The most fundamental assumption in the computational model is that of a potential flow field in which all vorticity is concentrated into the leading-edge vortices. It has been shown experimentally that the majority of axial vorticity in a leading-edge vortex is confined to a viscous subcore region having a diameter on the order of 5% of the local semi span. This

observation suggests that under certain circumstances, a potential vortex may be used to model leading-edge vortices. The model is therefore inviscid, where the only effect of viscosity is to fix the separation at the leading edge of the wing. Other researchers as mentioned previously have demonstrated the feasibility of using an inviscid assumption for unsteady delta wing flows below angles of attack where breakdown is present.

Legendre [137], Brown and Michael [138], and Mangler and Smith [139] have used potential vortex models of steady delta wing flow fields among others. These studies modeled the flow field on delta wings at zero roll angle. In order to simplify the computational model, slender wing theory was used, along with the assumption of a conical flow field. The primary difference of the models is the representation of the feeding sheet that emanates from the leading edge. In Arena's investigation, the Brown and Michael [138] branch cut representation of the feeding sheet was found to be more amenable for extension to the unsteady flow field. The Mangler and Smith model of a curved feeding sheet while more representative, was found to add no additional qualitative information while adding a great deal of complexity.

The actual and approximated flow fields can be seen in Fig. 54. The effect of the secondary vortices were

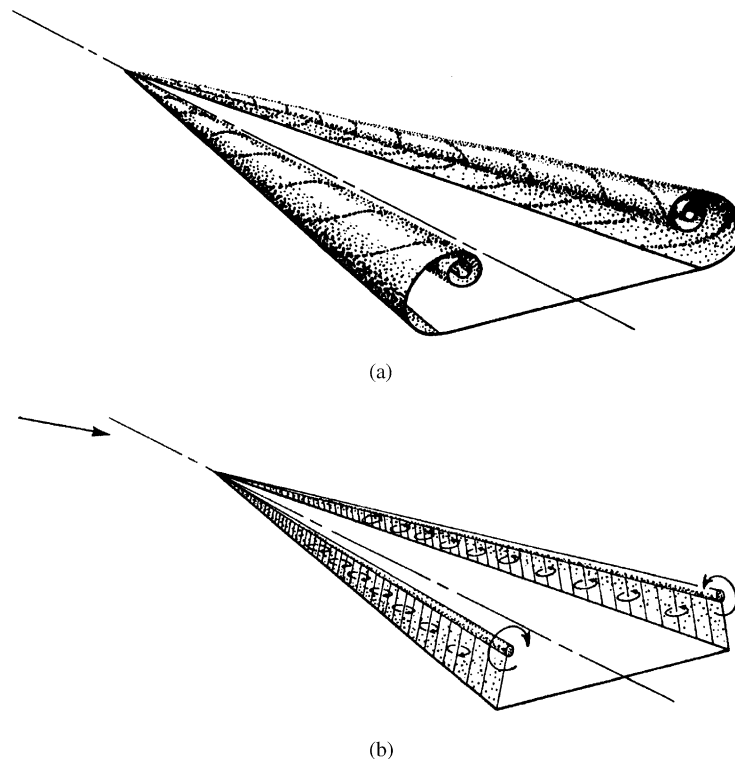


Fig. 54. Flow field approximation [138].

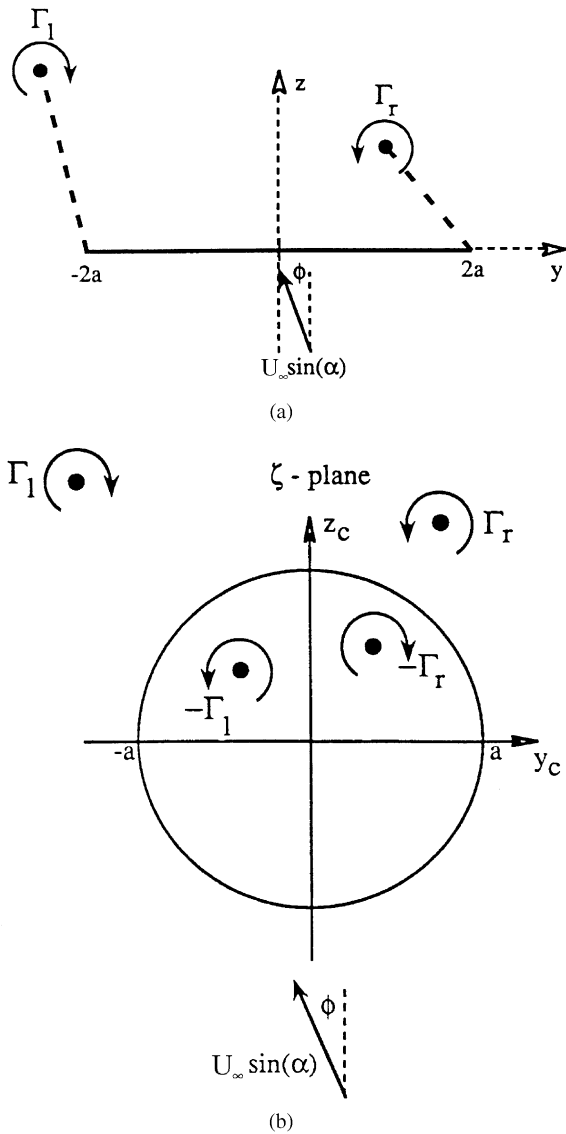


Fig. 55. Computational model of the flow field [130].

neglected by Arena. The flow field in the crossflow plane appears as shown in Fig. 55a. The branch cuts that feed the vortices are indicated as dashed lines in the sketch. In order to satisfy flow tangency, potential solutions are superimposed in the circle plane. The flow field in the circle plane is illustrated in Fig. 55b. The steady flow field flow tangency condition is satisfied with the superposition of image vortices, and a doublet with the rotated freestream as shown in the figure. The unsteady surface condition is satisfied with the addition of a source–sink sheet on the circle. This formulation chosen by Arena for his work significantly differs from that of Brown and Michael in that the wing is allowed to roll which creates six unknowns in vortex position and

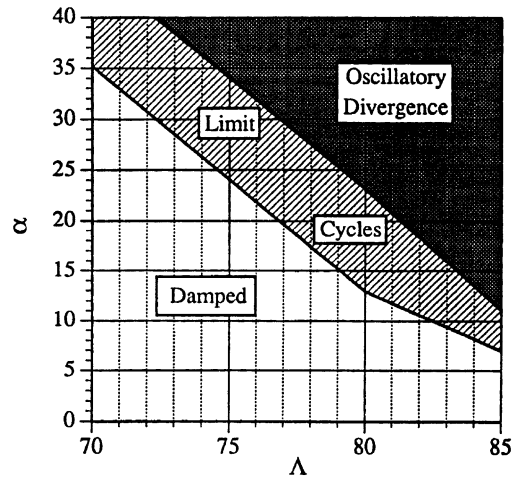


Fig. 56. Oscillatory motion envelope predicted by a computational model [140].

strength as opposed to three. Also, the formulation of the problem is accomplished in the circle plane and transformed back into the physical plane. This model developed by Arena [130] also differs from the Brown and Michael [138] model in that the wing is free to undergo unsteady rolling motions that require the solution of unsteady boundary and zero-force conditions, and the transfer of inertial coordinates into a body fixed frame. For additional details on Arena’s computational model the reader is referred to Arena [130] and Arena and Nelson [140].

Arena and Nelson [140] used the computational model to examine the rolling motion of wings of different sweep angle and angle of attack range. Three types of oscillatory behavior were captured with the model: damped oscillations, limit cycles and divergent oscillations. Fig. 56 is an oscillatory motion envelope which shows the predicted oscillation behavior for a given sweep angle and angle of attack. As seen in experiment, lower sweep angles and angles of attack reduce the wing’s susceptibility to self-induced oscillations. As angle of attack or sweep angle is increased, limit cycles and divergent oscillations are predicted. The region of oscillatory divergence is not seen in experiment since above a certain angle of attack, vortex breakdown appears on the wing that is not modeled in the simulation. It has been shown that over the range where vortex breakdown appears on the wing, it contributes a damping moment that reduces the steady state amplitude. Therefore, limit cycles are seen instead of divergence. There is however a large angle of attack range observed in experiment in which vortex breakdown is never seen on the wing. As mentioned in the experimental discussion, wing rock can occur without vortex breakdown occurring over the wing during

a wing rock oscillation. Again, when vortex breakdown occurs over the wing, its effect is generally to provide damping to the system thereby reducing the amplitude of the wing rock motion.

The spanwise pressure distribution at a given chordwise position was integrated to yield a sectional roll moment coefficient during the wing rock cycle. Fig. 57 shows the sectional rolling moment coefficient per unit chord as a function of roll angle for a wing rock cycle. The predicted rolling moment coefficient is consistent with Arena's experimental measurements discussed earlier. At low roll angles, the moment is adding energy to the system, but at large roll angles, the moment is providing damping or extracting energy from the

system. The leveling off of the roll moment coefficient for large roll angles is due to the decrease in the effective angle of attack.

Further insight into the mechanism causing the roll moment can be achieved by examining the contribution from the top and bottom surfaces. Fig. 58 is a plot of the separate contributions. Note that all of the instability in the motion is generated from the pressure distribution on the top portion of the wing. On the other hand, the bottom surface is providing damping. The origin of the damping loops from the upper surface pressure distribution will be discussed shortly.

Arena also used his computational model to study the flow field behavior during the wing rock motion. Since

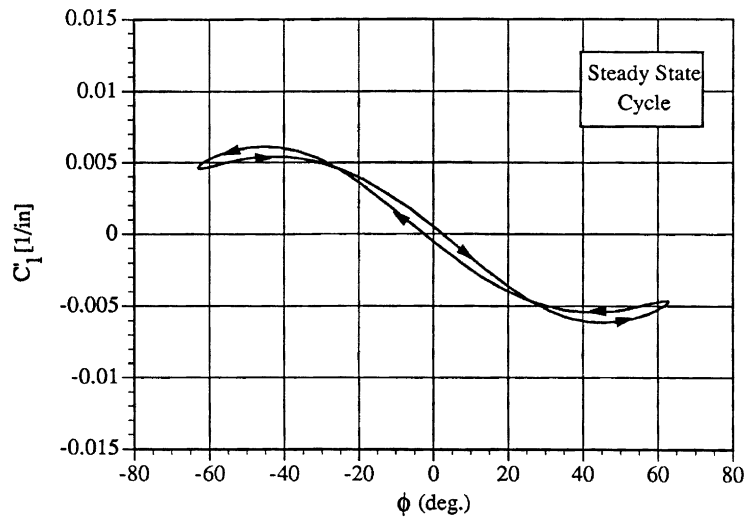


Fig. 57. Computed sectional roll moment coefficient for a steady state cycle of wing rock [130].

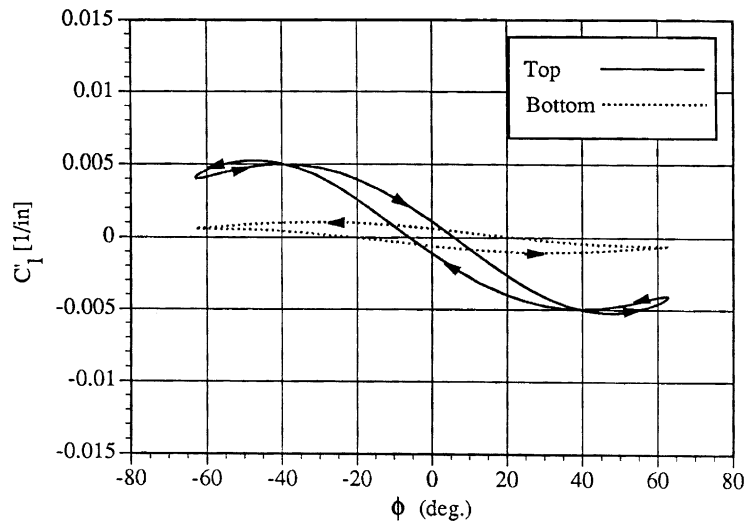


Fig. 58. Contribution to roll moment from top and bottom surfaces [130].

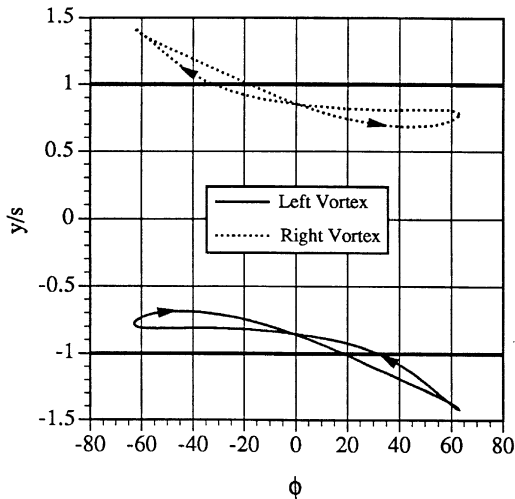


Fig. 59. Computed spanwise vortex position during wing rock [130].

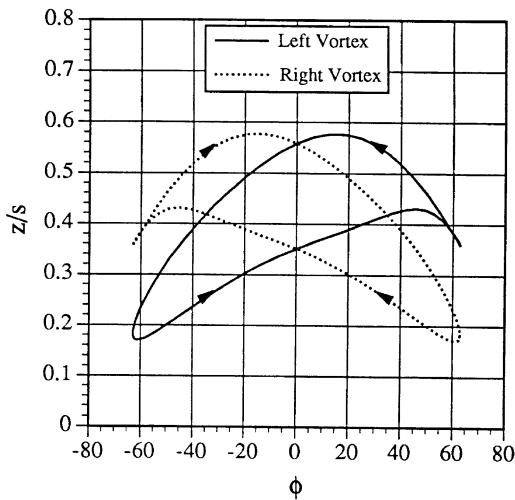


Fig. 60. Computed normal vortex position during wing rock [130].

the roll moment is responsible for driving the wing to the limit cycle, the computational model was used to identify physical mechanisms that would be consistent with the generation of the hysteresis in a roll moment. Figs. 59 and 60 are plots of computed spanwise and normal vortex position during a steady state cycle of wing rock. The spanwise motion of the vortices indicates some hysteresis during the cycle, however the maximum hysteresis is less than half of the maximum hysteresis seen in the normal direction. Hysteresis in the normal direction of the wing is seen to be dominant, especially in its effect on the roll moment. The arrows indicate that the normal position of the vortices lag behind the model

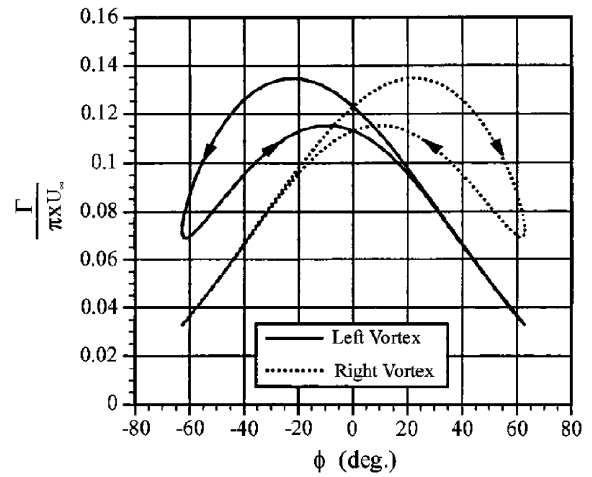


Fig. 61. Computed unsteady vortex strength during a wing rock cycle [130].

motion whereas the spanwise motion leads and lags depending on the part of the cycle.

Fig. 61 is a plot of computed left and right vortex strength during the steady-state cycle of wing rock. Relatively large hysteresis lobes for each vortex are apparent for only part of the cycle. If the vortex strength on the downward going wing is actually greater as $|\phi|$ is increasing, than when the wing is rolling in the other direction. It can therefore be reasoned that as the wing rolls to large angles, the unsteady change in vortex strength on the downward wing provides a damping contribution to roll moment. Also note that the hysteresis occurs only for the vortex which is closest to the wing. There is no hysteresis in the strength of the vortex which is on the upward side of the wing. Therefore the effect of the strength hysteresis occurs at a point where it will have the most effect on the roll moment. This is a very important observation since it indicates that the hysteresis in vortex strength actually provides damping at the large roll angles where the damping lobes are seen in the roll moment diagrams.

When Arena compared the computed flow field and motion characteristics with experimental measurements for a typical wing rock limit cycle, all of the major characteristics were consistent. This includes all the characteristics and nonlinearities in the time histories, phase plane, roll moment curves, and behavior of the unsteady vortex position. The top surface of the wing was responsible for all of the instability and for the damping lobes. The bottom surface of the wing provided a significant amount of damping. The computational model revealed that the hysteresis in vortex strength, which was greatest on the downward wing where the vortex is closest to the surface, is responsible for the

production of the damping lobes. The hysteresis in the vortex strength decreased with increasing angle of attack and increased with decreasing sweep angle. This discovery in addition to the other experimental and computational results led to a theory as to the cause of wing rock of slender wings.

By combining the results of the experimental and computational investigations, a theory for the cause of the wing rock of slender wings was developed and is broad enough to account for the variation in wing sweep and angle of attack. The theory applies to slender delta wings with sharp leading edges so that the separation points are fixed. Although the flow field of full aircraft configurations is more complicated, it is likely that analogous mechanisms are involved which are responsible for wing rock of these vehicles.

Some initial perturbation or imperfection in the wing initiates wing rock, *not* by an initial zero-roll angle asymmetry or “lift-off”. The experimental and computational results show that the zero roll angle flow field is symmetrical about the root chord when the wing is at rest. The amplitude of the motion grows in time due to the instability created by the lag in the position of the vortices, until the damping contributions from the top and bottom surfaces of the wing balance the instability and result in an equilibrium oscillation. The greater the damping contribution to roll moment, the lower the oscillation amplitude and vice versa. The conventional rate dependent roll damping provides damping from the bottom surface of the wing. The damping contribution from the top surface of the wing creates the damping lobes necessary to keep the motion from diverging. The damping lobes are created by the unsteady behavior of leading edge vortex strength. The hysteresis in vortex strength is only seen on the downward side of the wing where the vortex is closest to the surface. This is why the damping lobes appear at the large roll angles. The effect of the strength hysteresis contributes a roll moment that opposes the direction of rotation.

3.3.1. Summary

From the results obtained by Arena [130], a mechanism contributing to the destabilizing moment necessary to sustain the wing rock motion appears to be the time lag in the normal vortex position on the upward going wing. The destabilizing moment must be great enough to overcome the stabilizing effect of roll damping, for the oscillation to grow in amplitude. While the lag in the normal position of the vortices provides a mechanism for the growth in roll amplitude, it is the time lag in the vortex strength that provides the damping lobes at the high roll angles. When vortex breakdown occurs over the model, additional damping is added which results in an overall reduction in the wing rock amplitude.

3.4. Double-delta wing

A more complicated rolling motion is observed on a double-delta wing. Pelletier [141–143] studied the rolling motion and leeward surface vortical structure over an 80/65° double-delta wing. In his work, Pelletier identified various types of rolling motions, roll attractors and critical states associated with the various motions exhibited by the double-delta wing model.

Pelletier found that the wing rock motion can be centered around several roll attractors. Hanff and Ericsson [144] also indicated the existence of several roll attractors, on both single delta wings (like the 65° delta wing) and double-delta wings (an 80/65° double-delta wing used in their study).

Pelletier [141] found that the 80/65° double-delta wing would wing rock for angles of attack greater than 25°. This range of angles of attack corresponded to vortex breakdown being present over the wing. Different dynamic regimes were observed to occur with this wing as a function of angle of attack. There were damped oscillations, limit-cycle type of oscillations centered around zero or around non-zero roll angles and chaotic oscillations. Fig. 62 shows time histories for the double-delta wing at $Re_c = 300,000$. For low angles of attack ($\alpha \leq 25^\circ$), the wing was highly damped and there was no oscillation, as shown in Fig. 62a. As the angle was increased from $\alpha = 25^\circ$, wing rock started to occur, as shown in Figs. 62b and d. For angles of attack between $\alpha = 34^\circ$ and 39° , a chaotic oscillation was obtained, as seen in Fig. 62c. In this chaotic region, the wing behavior was random and the wing oscillated between positive and negative equilibrium points. Finally, for larger roll angles ($\alpha \geq 45^\circ$), there was a small oscillation around $\phi = 0^\circ$.

The different dynamic regimes encountered were associated with changes in the flow topology over the wing. For angles of attack $\alpha \leq 25^\circ$, there was no oscillation and vortex breakdown was not present on the wing. As mentioned earlier, the oscillations started when vortex breakdown moved over the wing at an angle of attack $\alpha > 25^\circ$. With vortex breakdown over the 65° section of the double-delta wing, the wing oscillated around roll angles different than 0°. The amplitude of oscillation increased after $\alpha = 27^\circ$. The amplitude started to decrease after $\alpha = 40^\circ$ and the oscillation was back around $\phi = 0^\circ$. This corresponded to the strake vortex breakdown reaching the wing/strake juncture of the double-delta wing. Contrary to the 80° delta wing where breakdown had a damping effect as soon as it moved over the wing, it only had a damping effect when it moved over the 80° section of the double-delta wing. For angles of attack in the range $34^\circ \leq \alpha \leq 39^\circ$, flow visualization indicated vortex lift-off at $\phi = 0^\circ$. This vortex lift-off was a sudden displacement of the vortex cores in the direction normal to the wing.

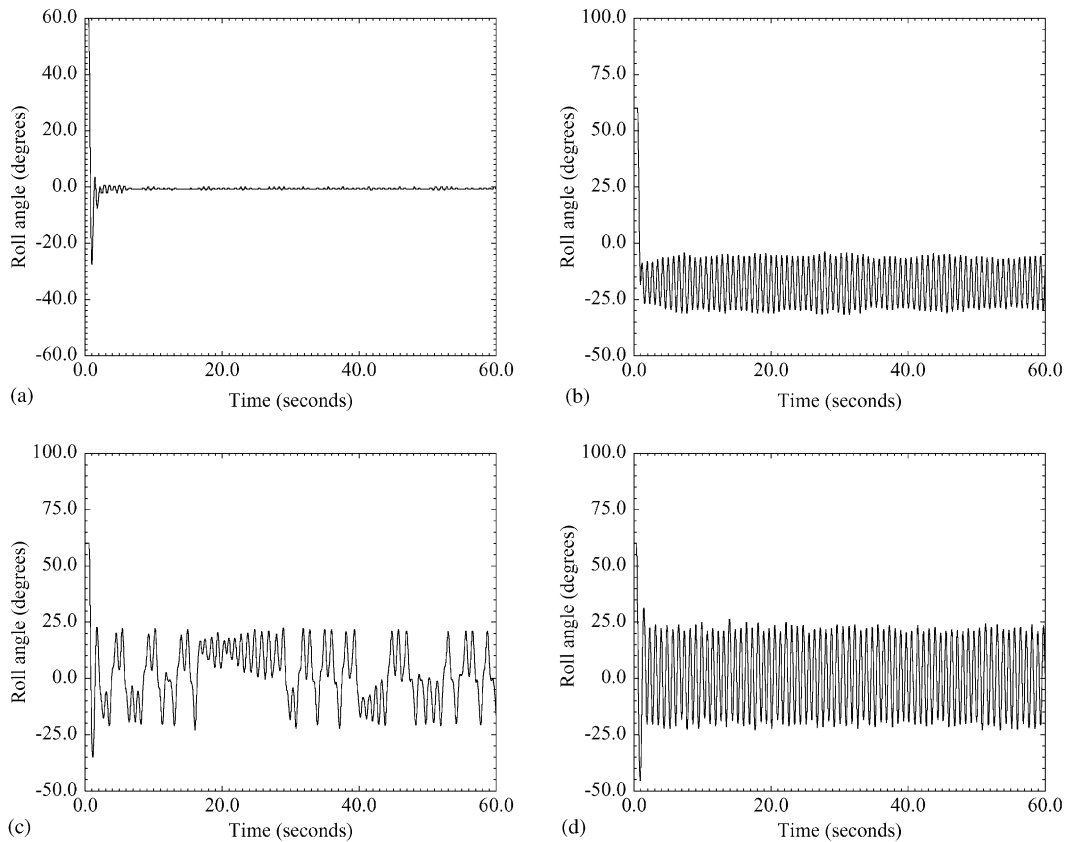


Fig. 62. Time histories for $\phi_0 = 60^\circ$ [141] (a) $\sigma = 25^\circ$ (b) $\sigma = 30^\circ$ (c) $\sigma = 35^\circ$ (d) $\sigma = 40^\circ$.

This led to a drop in the normal force in force balance data at $\alpha \approx 34^\circ$. As the wing was rolled to a small roll angle, the windward vortex core reattached to the wing, or moved closer to the wing, while the leeward vortex did not. These changes in the flow topology affected the behavior of the wing and are also believed to have given rise to critical states.

A critical state is defined as the value of the motion variable (e.g. the angle of attack or roll angle) where there is a discontinuity in the aerodynamic coefficient or its derivative. Fig. 63 is a sketch of a hypothetical rolling moment coefficient vs. the roll angle that illustrates various critical states. Mathematically, the critical state is defined as the value of the motion variable where the aerodynamic coefficient or derivative is not analytic. This is indicated in the figure as points A and B. Since at the critical state the aerodynamic characteristics change abruptly, it is reasonable to assume that there is also a corresponding change in the flow field. The flow bifurcates from one stable regime to another. Some examples of flow regimes that change abruptly and cause a discontinuity in the aerodynamic characteristics are the flow over a slender nose shape or a delta wing. In the

case of a slender nose shape at angle of attack, the flow separates symmetrically to form two symmetric vortices above the body as shown in Fig. 4. As the angle of attack increases, a critical angle of attack is reached where the forebody vortices suddenly become asymmetric creating both a side force and yawing moment on the nose. The critical state is the angle of attack where the lateral forces develop and the flow becomes asymmetric. Crossing this critical state can result in a rapid departure of the aircraft, the so-called nose slice discussed in Section 1.1.4. In this case, there would be a discontinuity in the derivative of the side force and yawing moment coefficient and would be similar to the critical state labeled A in Fig. 63. Another example of a critical state is observed on delta wings. As the angle of attack increases, vortex breakdown of the leading-edge vortices approaches the trailing edge. When a critical angle attack is reached, vortex breakdown jumps from a position behind the wing trailing edge to a position upstream of the trailing edge. This bifurcation in the position of vortex position can result in a jump or discontinuity in the aerodynamic characteristics of the delta wing. The discontinuity would look similar to that

labeled as critical state B in Fig. 63. In Fig. 63 the point labeled C may also be a potential critical state. Although the function is continuous near point C, it may actually be a multi-valued function. For example, consider the static lift curve of a typical airfoil section. If the airfoil is thin, then as the stall angle is approached, the lift curve will have a sudden drop in the lift curve or a discontinuous value of the derivative. On the other hand, a thick airfoil section will have a more gradual change in slope, the slope will change from positive to a negative value as the angle is increased beyond stall. The

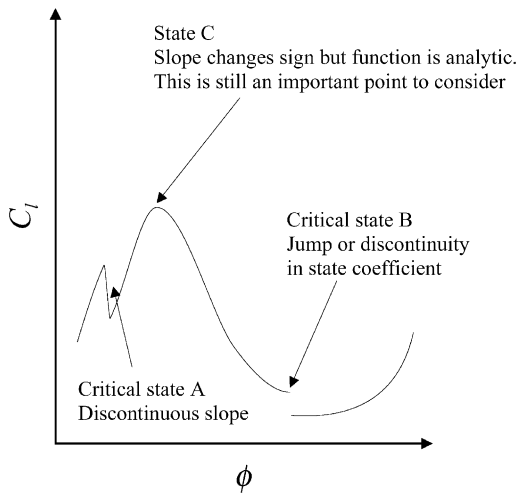


Fig. 63. Possible critical states from static roll moment coefficient data [141].

lift coefficient near and beyond the stall angle is actually a multi-valued function that is consistent with the concept of a critical state. The static lift coefficient depends upon whether the angle of attack is increasing or decreasing through the stall angle. It is well known that the lift curve of a two dimensional airfoil will exhibit static hysteresis in the stall region. When static hysteresis occurs, the aerodynamic function is multi-valued. Measurement of vortex lift-off, vortex breakdown and the aerodynamic coefficients on a delta wing can exhibit static hysteresis under certain conditions. Therefore it is reasonable to assume that the point labeled as C in Fig. 63 could be a potential critical state.

In reference to the double-delta wing measurements, a critical state is believed to exist at a roll angle where there is vortex lift-off (which also occurs on the leeward side of the wing as it is rolled), vortex reattachment to the surface, and vortex breakdown moving onto the wing. At a critical state, there is transition from one equilibrium state to another due to some flow instability [145].

The presence of critical states can have a strong influence on the dynamic airloads and the dynamic behavior of a wing. Data at $\sigma = 30^\circ$ from a cooperative effort between the Canadian Institute for Aerospace Research and the United States Air Force Wright Laboratory on an $80/65^\circ$ swept double-delta wing was used by Pelletier [141] to illustrate how critical states affect the behavior of a wing when they are encountered. Fig. 64 shows two typical forced oscillation motions that were used to obtain dynamic roll moments on the IAR/WL $80/65^\circ$ double-delta wing. Table 3 summarizes

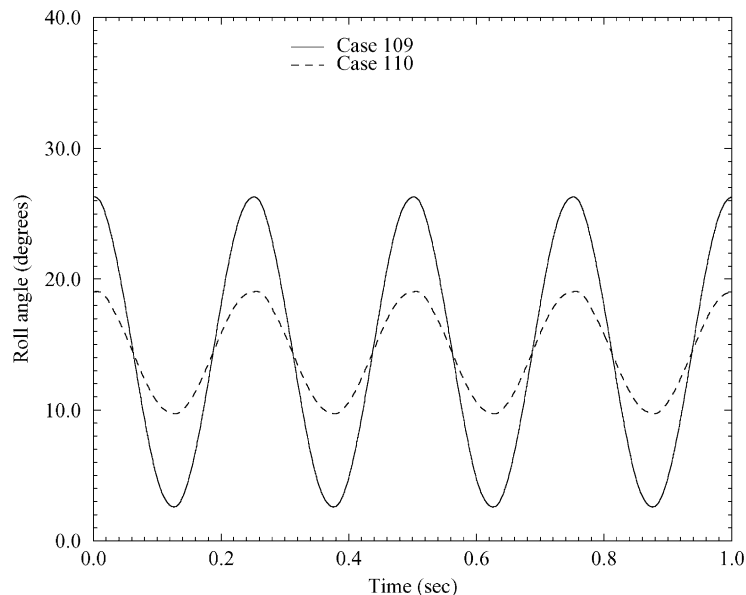


Fig. 64. Time histories for dynamic oscillations with $f_{osc} = 4$ Hz [141].

several dynamic cases for different amplitudes ($\Delta\phi$) and mean roll angles (ϕ_c).

Fig. 65 indicates the major critical angles observed at $\sigma = 30^\circ$ [141] and the flow topology changes associated with them. With these critical angles in mind, dynamic IAR data was analyzed. When the wing passed through an angle associated with a critical state, lags in C_l occurred: the dynamic values of C_l were not always equivalent to the static values of C_l for a given instantaneous roll angle. The magnitude of this lag depended upon the angular velocity of the force oscillation: in general, the larger the average angular velocity $\dot{\phi}$, the larger the lag [56].

3.4.1. No critical state encounter

When none of the previously mentioned major critical states was encountered during the motion, the dynamic roll moment usually tended to be quasi-steady, as was observed by Ericsson [146]. This means that the dynamic

roll moment and static roll moment were almost identical for instantaneous roll angles. In other words, when there was no critical state encounter, the instantaneous value of the roll moment was independent of $\dot{\phi}$, $\ddot{\phi}$ and past motion history, and only depended on the instantaneous value of ϕ . Fig. 66 shows the IAR dynamic data for an oscillation frequency of 4 Hz and $\Delta\phi = 4.7^\circ$ around $\phi_c \approx 14^\circ$ (case 110). Since no critical state was believed to be encountered, the dynamic roll moment coefficient exhibited a quasi-steady behavior and any dynamic contribution to the roll moment was small.

3.4.2. Critical state encounters

When a critical state was encountered, a time lag appeared in the roll moment response as the roll angle was varied. Fig. 67 shows the dynamic roll moment response for a 4 Hz forced oscillation around 14° and $\Delta\phi = 11.8^\circ$ (case 109). For this oscillation, the motion went through $\phi \approx 5^\circ$, which was believed to be a critical state. As the wing was rolling towards the critical state, the roll moment variation was quasi-steady until the critical state was encountered. After the encounter, the wing motion was reversed and a time lag, or hysteresis loop, appeared. This lasted until the effect of the critical state encounter had time to disappear at around $\phi = 22^\circ$, where the roll moment variation once again became quasi-steady.

When more than one critical state were encountered, the size of the hysteresis loop was larger. The size was

Table 3
IAR dynamic cases for $f_{osc} = 4$ Hz and $\sigma = 30^\circ$

Case #	$\phi_c(^\circ)$	$\Delta\phi(^\circ)$
100	0	26.1
106	0	4.7
109	14	11.8
110	14	4.7
516	42.5	32.7
1415	7	26.5

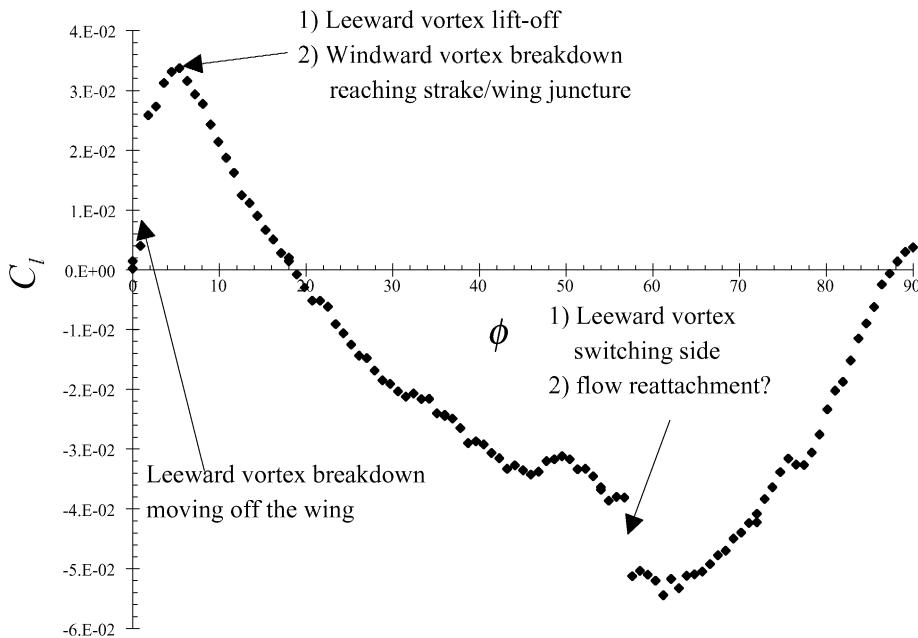


Fig. 65. Topology changes at dominant states for $\sigma = 30^\circ$ on an 80/65° double-delta wing [141].

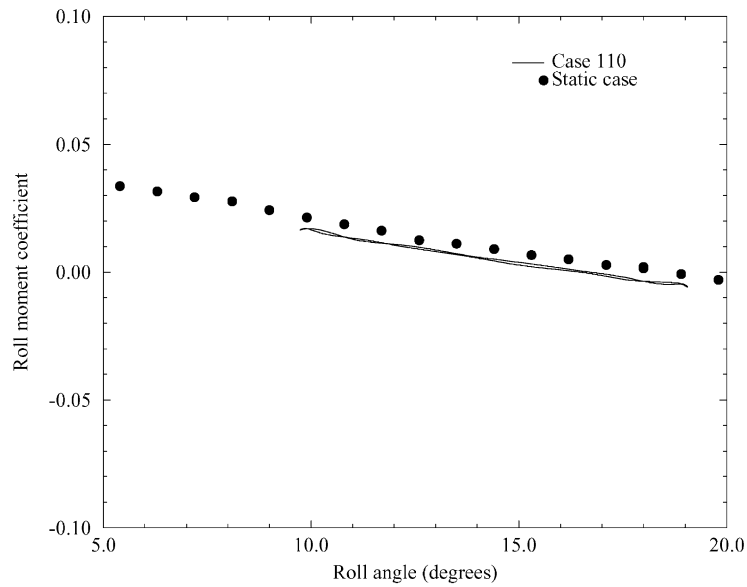


Fig. 66. Dynamic roll moment for $f_{osc} = 4$ Hz, $\Delta\phi = 4.7^\circ$ around $\phi_c \approx 14^\circ$ [141].

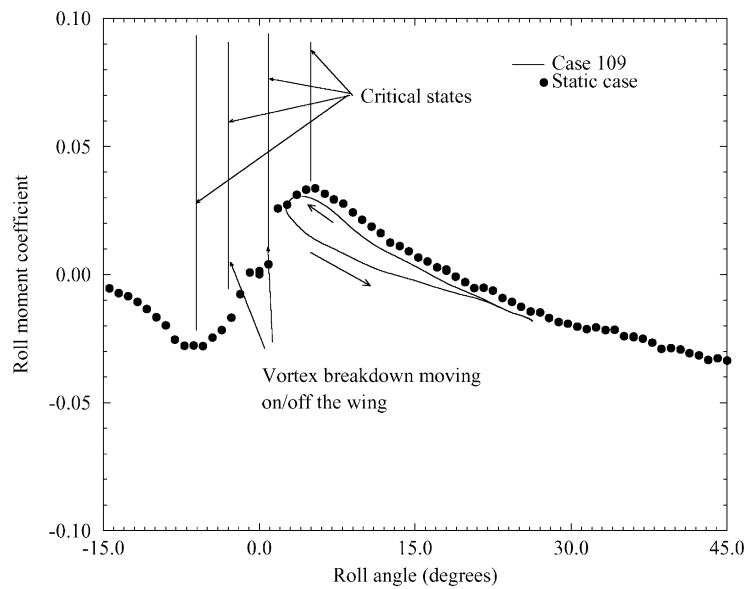


Fig. 67. Dynamic roll moment for $f_{osc} = 4$ Hz, $\Delta\phi = 11.8^\circ$ around $\phi_c \approx 14^\circ$ with location of major critical states marked [141].

also a function of the amplitude of the forced oscillation: smaller amplitudes yielded smaller loops because the average angular velocity $\dot{\phi}$ was smaller. Fig. 67 showed the existence of a critical state near $\phi \approx 5^\circ$. By symmetry, another critical state was observed near $\phi \approx -6^\circ$. Fig. 68 shows that another critical state, or two due to symmetry, probably existed near $\phi = 0^\circ$, since a 4 Hz

forced oscillation around $\phi_c = 0^\circ$ with $\Delta\phi = 4.7^\circ$ (case 106) did not yield a quasi-steady variation for C_l , even though the $\phi \approx \pm(5-6^\circ)$ critical states were not encountered. Critical states were then discovered to exist near $\phi = 0^\circ$, as mentioned earlier, and they appeared to correspond to the leeward vortex breakdown moving off the wing into the wake (at $\phi \approx +1^\circ$ and $\phi \approx -3^\circ$). For

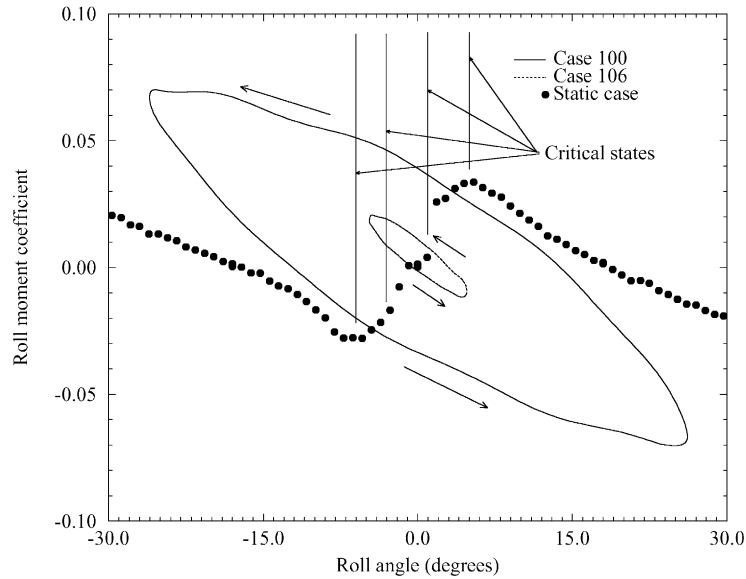


Fig. 68. Dynamic roll moment for $f_{\text{osc}} = 4$ Hz, around $\phi_c = 0^\circ$ with location of major critical states marked [141].

a similar wing motion around $\phi_c = 0^\circ$ with a larger $\Delta\phi = 26.1^\circ$ (case 100), several critical states were encountered (at least 4) and the roll moment variation never had time to become quasi-steady, as is also shown in Fig. 68. A larger amplitude of oscillation would probably be required in order to reach a quasi-steady behavior during the forced oscillation. It was not believed that several critical state encounters was synonymous with the roll moment behavior never becoming quasi-steady. Fig. 69 shows that for a 4 Hz oscillation centered about $\phi_c \approx 7^\circ$ with $\Delta\phi = 26.5^\circ$ (case 1415), several critical states were encountered, but a quasi-steady C_l variation was obtained as the wing rolled from a large positive roll angle (away from any apparent critical state) towards the $\phi \approx 5^\circ$ critical state. A quasi-steady behavior for some segment of a cycle could then be obtained, even in the presence of several critical state encounters.

Finally, Fig. 70 indicates the existence of another critical state near $\phi \approx 57^\circ$ for a 4 Hz oscillation centered about $\phi_c = 42.5^\circ$ with an amplitude of 32.7° (plus its counterpart near $\phi \approx -57^\circ$) (case 516). The roll moment variation was quasi-steady (starting from $\phi \approx 10^\circ$) until the critical state was encountered. After the critical state encounter, the dynamic value of the roll moment departed from its static counterpart until the wing motion was reversed. It was then quasi-steady until the critical state was once again reached. The roll moment became quasi-steady at $\phi \approx 25^\circ$ after a time delay. As was indicated in Fig. 65, these critical states were believed to be associated with flow reattachment on the windward side of the wing as the effective angle of attack was decreased. Flow visualization also showed

that the discontinuities at $|\phi| \approx 57^\circ$ could also be related to the leeward vortex switching side on the wing.

3.4.3. Summary

Several critical states were believed to be present in the flow field over the 80/65° double-delta wing used in the investigation reviewed herein. These critical states appeared to be related to changes in the vortex flow and flow topology over the wing and yielded dynamic roll moment hysteresis when encountered during the wing motion.

It was observed that if no critical state, as the ones defined in this review article, was encountered during the wing motion, the dynamic roll moment was quasi-steady. This was often the behavior observed during free-to-roll studies at $\sigma < 34^\circ$: the wing appeared to stay away from critical states during self-induced oscillations. Therefore, for these free-to-roll cases, the instantaneous roll moment acting on the wing at any time could probably be estimated by the static roll moment.

3.5. Remarks

The unsteady aerodynamic characteristics of slender flat plate delta wings at large angles of attack is affected by the lag in the development of the leading-edge vortical structure. As illustrated by the pitching delta wing example, the lag in the movement of vortex breakdown can cause significant overshoot or undershoot in the measured aerodynamic loads. When the model is pitched through a range of angle of attack where breakdown does not occur over the wing, the

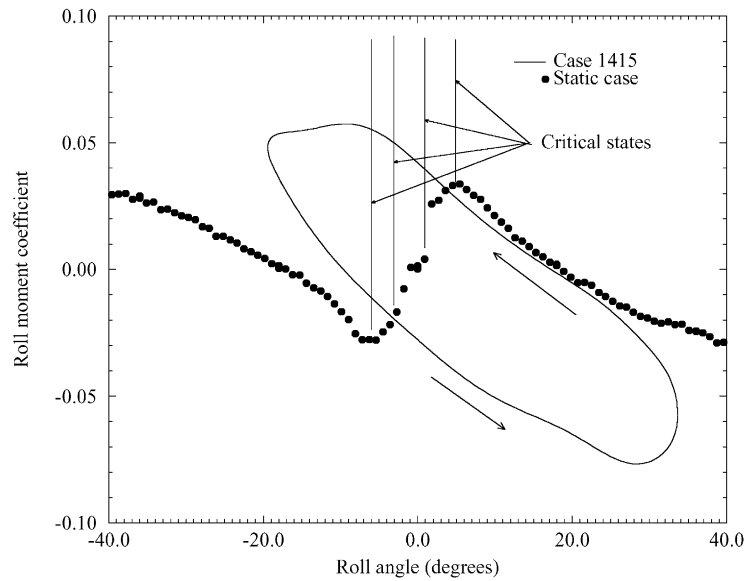


Fig. 69. Dynamic roll moment for $f_{osc} = 4$ Hz, $\Delta\phi = 26.5^\circ$ around $\phi_c \approx 7^\circ$ with location of major critical states marked [141].

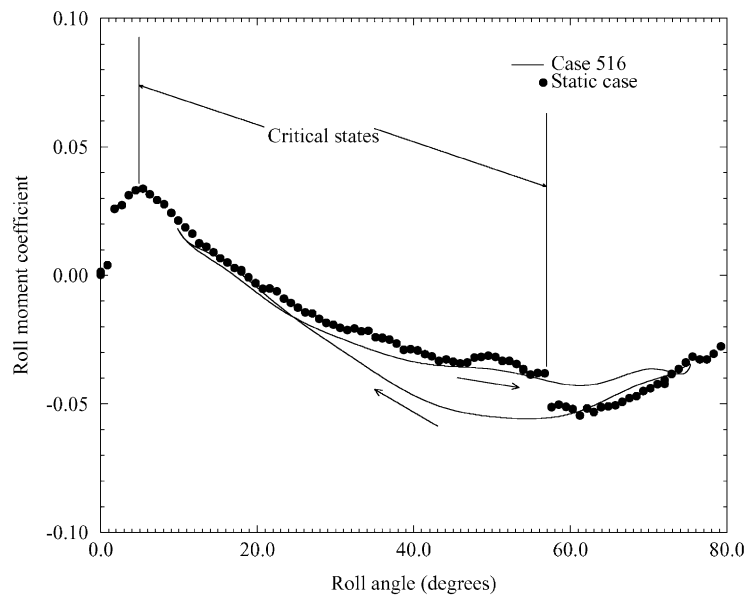


Fig. 70. Dynamic roll moment for $f_{osc} = 4$ Hz, $\Delta\phi = 32.7^\circ$ around $\phi_c = 42.5^\circ$ with location of major critical states marked [141].

aerodynamic characteristics were found to be quasi-static. On the other hand, for motion ranges that encompass vortex breakdown, the aerodynamic loads were found to be a function of reduced frequency and motion amplitude range. The lag or hysteresis behavior in vortex breakdown location exhibited similar trends. The fluid dynamic mechanism causing the unsteady

aerodynamic load changes is a result of the flow field lag associated with vortex breakdown.

For the case of a rolling delta wing the position of the leading-edge vortices relative to the model surface as well as vortex breakdown play an important role in the unsteady rolling moment characteristics acting on the wing.

4. Aircraft dynamic characteristics and unsteady aerodynamics

As stated in the introduction to this article, flight dynamic phenomena such as wing rock, wing drop, and buffet are flight dynamic problems that are caused by unsteady aerodynamics. In this section the rolling characteristics of two aircraft are examined. The aircraft selected were NASA's High Angle-of-Attack Research Vehicle HARV, a modified F-18, and the X-31 research aircraft. Both flight test and wind tunnel experiments are reviewed. The discussion will emphasize the relationship between the unsteady aerodynamics and the aircraft's rolling characteristics.

4.1. F-18 HARV

The National Aeronautics and Space Administration, NASA, conducted a research program in the early 1990s called the "High Alpha Technology Program" (HATP). This research program was designed to evaluate advanced aerodynamic and propulsion technologies for highly maneuverable aircraft. A modified F-18 aircraft was used as a flight demonstration vehicle. The research program included wind tunnel, flight test and computational fluid dynamic experiments. Full scale wind tunnel experiments were conducted in the 80 × 120 ft National Full Scale Aerodynamics Complex at the NASA Ames Research Center as well as subscale experiments in smaller NASA tunnels. In addition, computational fluid dynamics (CFD) codes were used to compute component and complete aircraft aerodynamic characteristics. The goals of the study included evaluation of vortex control and thrust vectoring technologies to improve aircraft maneuverability. Another goal was to compare and evaluate the results from the flight, ground based and computational experiments so that improvements in testing techniques and computational modeling could be achieved. More details about the accomplishments of the HATP program can be found in Refs. [147–153].

The HARV aircraft was equipped with a variety of sensors and flow visualization equipment to measure the surface and off-surface flow characteristics. Some of the sensors used on the flight vehicle were pressure sensors to measure the pressure distribution over the forebody, wing and vertical tail surfaces and a rotating rake with multiple five hole probes to measure the flow field throughout the vortex over the leading-edge extension. In addition, the flow was visualized on the surface of the aircraft by using tufts and surface flow marking techniques and the off-surface flow was made visible with smoke.

The surface flow visualization was used to identify the surface flow patterns over the forebody and leading-edge extension (LEX). Off-surface visualization of the fore-

body and LEX vortices was accomplished by introducing smoke through ports on the forebody and near the leading-edge extension. The smoke was entrained primarily in the core of the forebody and the LEX vortices. The smoke tracer clearly marked the trajectories of the vortices over the aircraft. Vortex breakdown and the interaction of the forebody and LEX vortices were recorded for steady and dynamic flight conditions.

Surface flow visualization utilized both an emitted fluid technique and nylon tufts attached to the aircraft surface. The surface streaklines were made visible using a mixture of propylene glycol monomethyl mixed with red dye. Small quantities of this mixture were allowed to flow from circumferential rings of flush mounted orifices on the forebody and spanwise rows of flush mounted orifices located on the upper surface of the LEX. The surface flow patterns were obtained by first placing the aircraft into the desired flight condition. Once this was accomplished the fluid mixture was allowed to flow from the ports to mark the surface streaklines. The flight test condition was held for 75–90 s to allow the visualization mixture to evaporate. The flow pattern was then photographed after the aircraft landed. Figs. 71 and 72 show the surface flow pattern on the forebody and leading edge extension for an angle of attack of 26°. The surface flow patterns on the forebody are annotated to show the location of the primary and secondary separation lines as well as the attachment lines. Included with the photographs are sketches of the surface and off-surface flow in the crossflow plane. In Fig. 72, the separation line of the primary vortex is fixed by the sharp leading edge of the LEX. The surface flow patterns show the secondary and tertiary vortex separation lines.

Off-surface flow visualization was accomplished using smoke to mark the forebody and LEX vortices. Smoke was introduced through flush mounted ports on the nose and near the LEX apex. In the picture shown in Fig. 73, the smoke is entrained along the vortex core of the LEX. The trajectory of the vortex core is clearly marked by the smoke. At a location just forward and outboard of the vertical tail, vortex breakdown is observed to occur. The smoke pattern at the breakdown location appears to indicate a spiral form of breakdown. The tufts on the inboard section of the wing show the influence of the LEX vortex in maintaining attached flow in this region. The tufts are directed outward and aft indicating attached flow.

Quantitative data on vortex breakdown location and trajectory information was determined from the photographic data. Fig. 74 shows a comparison of wind tunnel and flight test measurements of the location of the LEX vortex breakdown location as a function of angle of attack. Vortex breakdown location was found to be insensitive to Reynolds number. The flight test

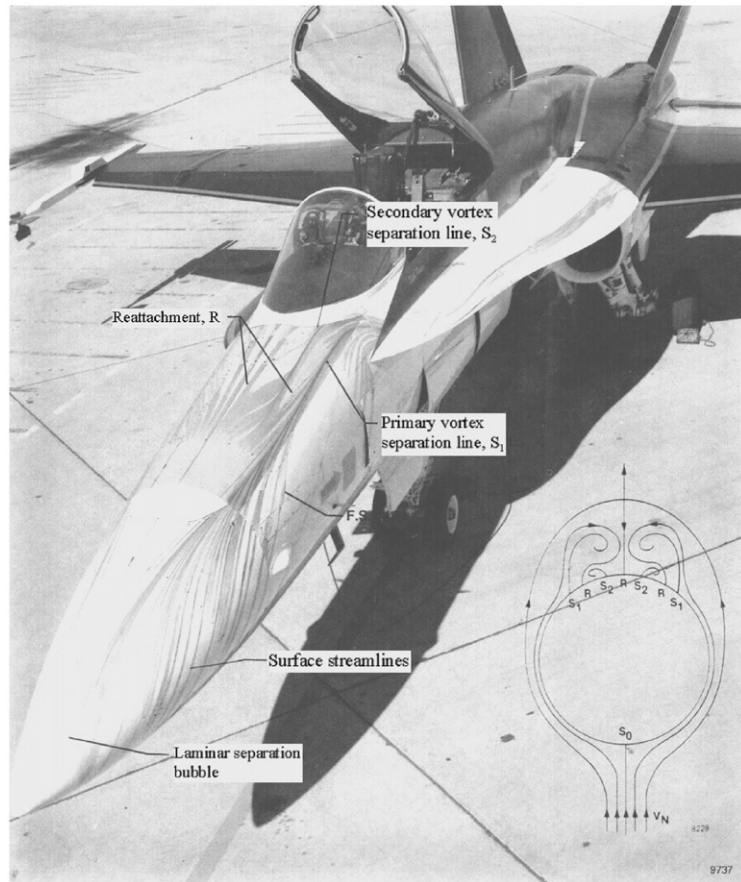


Fig. 71. Surface flow visualization on the nose section of the HARV, $\alpha = 26^\circ$ [147].

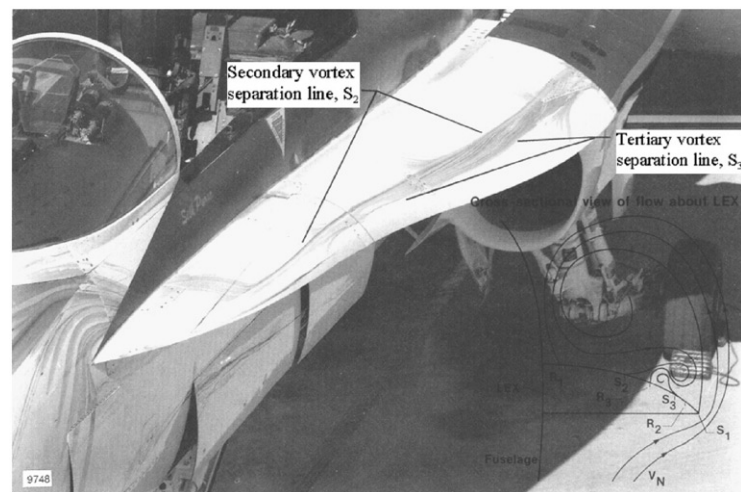


Fig. 72. Surface flow visualization on the LEX section of the HARV, $\alpha = 26^\circ$ [147].

measurements of vortex breakdown location are in good agreement with the wind and water tunnel measurements even though there is an order of magnitude

variation in the Reynolds number. This is consistent with the observations made on sharp-edge delta wing models.

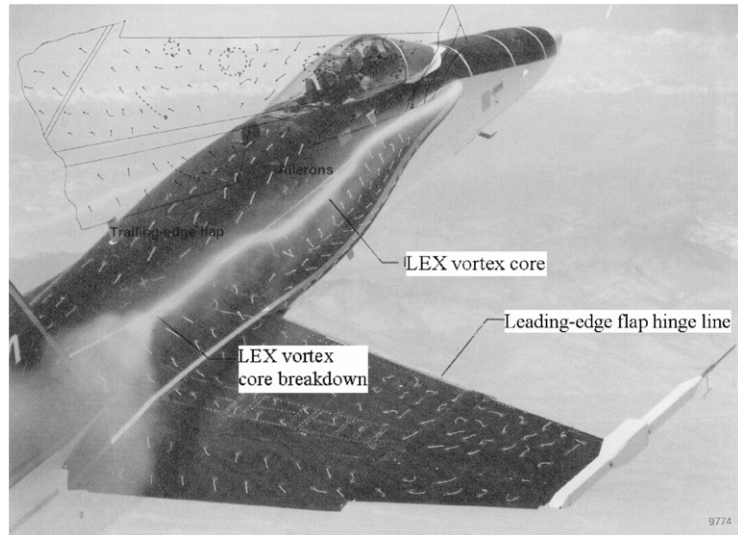


Fig. 73. Off-surface smoke visualization of the leading edge vortex, $\alpha = 20^\circ$ [149].

	$Re_{\bar{c}}$	Model scale, percent	Fluid medium	Ref.
● Flight	8 to 13 x 10 ⁶	—	Air	18
□ DTRC	1.75 x 10 ⁶	6	Air	4,18
◇ BART	1.60 x 10 ⁵	3	Air	18
△ LSWT	3.60 x 10 ⁵	12	Air	18
▽ FVF	1.26 x 10 ⁴	3	Water	18

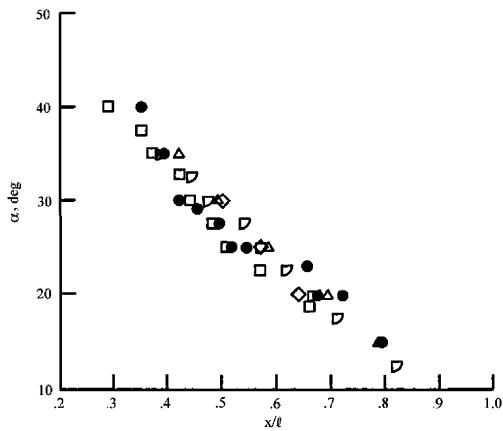


Fig. 74. Comparison of F-18 LEX core breakdown location from ground and flight test experiments [150].

An example of the flight test, wing rock data is shown in Fig. 75. The data was acquired at a flight Reynolds number of 11 million and at an angle of attack of 45° . This figure includes both roll (ϕ) and sideslip (β) angle

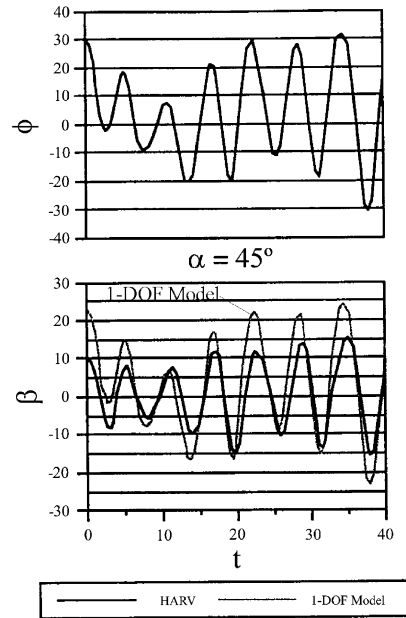


Fig. 75. HARV time histories (ϕ and β in time) [152].

for the entire wing rock test. In addition, a computed sideslip angle for a one degree-of-freedom rolling motion has been overlaid in the sideslip angle time history plot. The roll angle time history shows a strong presence of wing rock, as can be seen in the oscillatory cycles ranging in amplitude from 30° to -30° . It is also noted from the sideslip time histories that the HARV's motion is very close to what would be expected for a single degree-of-freedom rolling motion. The sideslip

angle is primarily due to the roll angle. In conducting the wing rock flight test experiments, the flight control system that would normally suppress the wing rock motion was disengaged. The pilot attempted to maintain the angle of attack; however, the pilot was instructed not to use the rudder or lateral stick input during the wing rock motion.

In addition to determining the wing rock time history, flow visualization experiments were performed during flight tests to examine the change in the flow field while the aircraft experienced a wing rock motion. Fig. 76 shows the position of the forebody vortices during a wing rock cycle for the flight test. The trajectory of the forebody vortices changes dramatically as the aircraft undergoes a wing rock motion. As the aircraft rolls, the forebody vortices interact with the LEX vortices. One forebody vortex is pulled down into the LEX vortex while the remaining forebody vortex moves over to the other side of the canopy.

Quast [154] and Quast et al. [155] studied the rolling motion of an F-18 model using the free-to-roll apparatus developed by Arena [130]. A 2% scale model of the F-18 was mounted on the free-to-roll apparatus and the motions were recorded as a function of angle of attack. The model was found to exhibit wing rock over a wide range of angles of attack. Fig. 77 is a typical time history of the rolling motion. The model was released with an initial roll angle of 0° and the motion built up to a steady state wing rock motion.

Fig. 78 presents the comparison of wind tunnel and flight test data for the amplitude envelope. The data shows good agreement in several areas. The first area of agreement is the general trend of the envelope. Both

flight test and wind tunnel data show a rising trend in the wing rock amplitude between $\alpha = 30^\circ$ and 40° . The peak motion occurs at $\alpha = 45^\circ$, after which there is a sharp drop-off in the wing rock motion. Along with the comparable envelope shape, the amplitudes of the data compare reasonably well within the uncertainty of estimating the HARV wing rock amplitudes. This plot helps to identify one area of subscale utility, that being the ability to identify regions in which a particular phenomenon will occur. In this case, it is obvious that there is a range of angle of attack ($40\text{--}47^\circ$) where robust wing rock motion occurs. Additionally, it is possible to predict the magnitude of this motion, as can be seen from the close correlation in the data.

Through the use of flow visualization experiments, a strong interaction between the forebody and LEX vortices during the wing rock motion has been observed. The trends in the vortical flow behavior observed in the wind tunnel are qualitatively the same as those observed in the flight test flow visualization study. The wing rock motion is believed to be caused by the interaction of the forebody and LEX vortices. This can be seen by the forebody and LEX vortex core positions during a wing rock cycle in Fig. 79. During the wing rock, the forebody vortex core on the side of the 2% subscale model where the wing is moving downward moves toward the LEX vortex on the same side. The forebody vortex core on the side of the upward moving wing vortex moves to a position over the top of the canopy. Near the largest roll angle, the forebody and LEX vortices intertwine around each other until the model reverses its motion. The process is reversed as the model rotates in the opposite direction. A simple experiment was conducted to test the

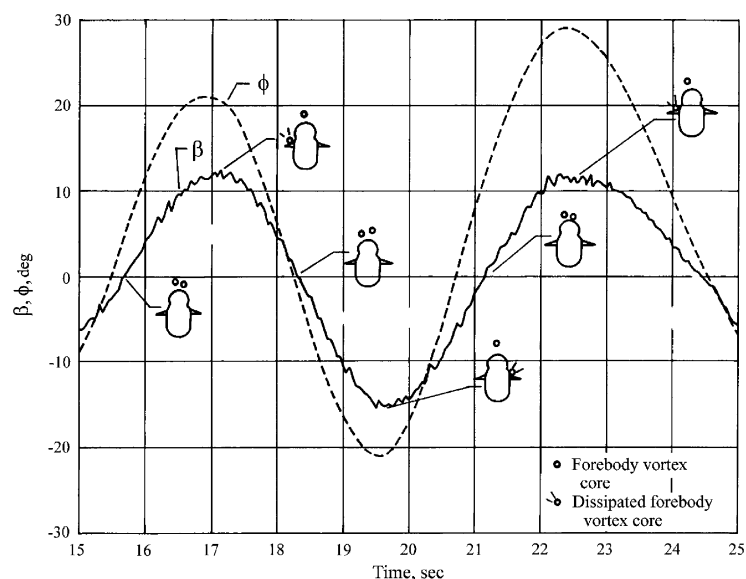


Fig. 76. Visualization data on the movement of the forebody vortices during a flight test wing rock motion, $\alpha = 45^\circ$ [152].

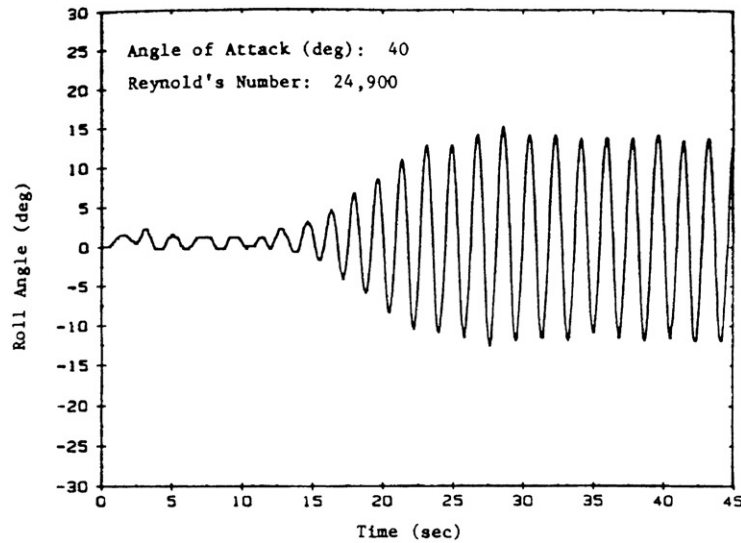


Fig. 77. Typical wing rock motion for the 2% scale model F-18 [154,155].

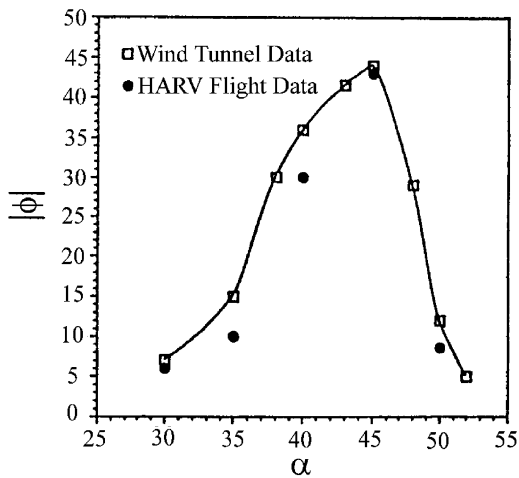


Fig. 78. Comparison of HARV and subscale model wing rock envelopes [154,155].

forebody vortex–LEX vortex interaction hypothesis. The model forebody was removed and a hemispherical cap was added to the model just before the canopy juncture. This configuration did not exhibit the wing rock motion since the forebody vortices were not present. This points to the vortex interaction mechanism as a driving cause of the wing rock motion.

The remarkable agreement of the subscale dynamic experiments with the flight vehicle results was examined by Williams et al. [156]. The flow characteristics over the F-18 subscale model were found to be similar except for the location of the primary separation lines on the forebody. The difference in the forebody flow separation

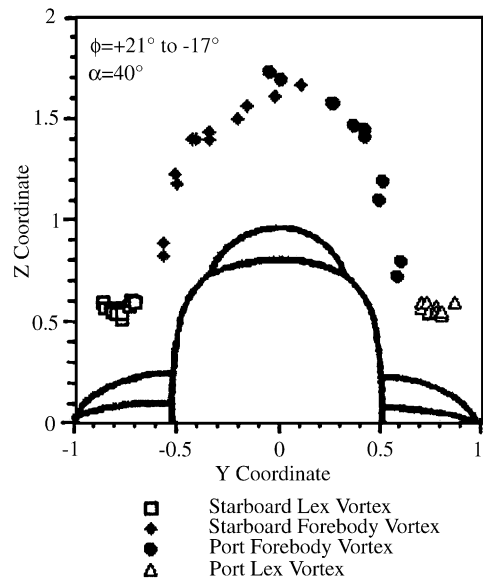


Fig. 79. F-18 model forebody and LEX vortex core positions during wing rock at $\alpha = 40^\circ$ [154,155].

lines was the result of laminar vs. turbulent flow forward of the separation line. Although the separation points are different, the forebody vortices are similar. This was confirmed by off-surface flow visualization.

From the experiments of Williams et al. [156] and their analysis, the following conclusion was reached: the use of subscale models can be used to predict high angle-of-attack dynamic behavior such as wing rock provided proper precautions are taken. The major issue that

must be addressed is the Reynolds number effect on the forebody. As observed in experiments (both wind tunnel and flight), there was a significant interaction of the forebody and LEX vortices. It appears that this interaction is a major contribution to the wing rock motion of the F-18 aircraft. Therefore, to simulate the wing rock motion using a subscale dynamics test, it is essential that the forebody vortices exist. This means that testing at Reynolds numbers where the forebody flow may be in the transitional regime should be avoided.

4.2. X-31 Aircraft

The goal of the X-31 program was to exploit advanced aerodynamic, propulsive and flight control technologies to provide aircraft with enhanced maneuverability. Fig. 80 shows a picture of the X-31 in flight. A detailed review of the X-31 program is provided by Alcorn et al. [157]. During spin tunnel and drop model tests of subscale models of the X-31, an unexpected roll departure was observed. The models were observed to rapidly roll up to a high roll rate. This unexpected rolling motion was called high incidence kinematic roll (HIKR). Wind tunnel experiments revealed that at large angles of attack, there was a strong interaction between the fuselage forebody vortices and the wing. The forebody vortices were asymmetric at large angles of attack. One of the forebody vortices was observed to impinge on the upper surface of the wing, thus creating a propelling rolling moment. Nose strakes were found to delay the onset of HIKR by disrupting the asymmetric

shedding of the forebody vortices. Modifications suggested from the wind tunnel experiments were incorporated on the flight vehicle to eliminate this problem.

Williams et al. [158] examined the rolling characteristics of a 2% scale model of the X-31. The experiments were conducted at a low Reynolds number so that the crossflow Reynolds number on the nose was subcritical. This ensured that forebody vortices were present during all the experiments. The model was mounted on Arena's previously described free-to-roll apparatus and the rolling motion was recorded. The canard deflection angle was set as a function of the angle of attack. Two different canard schedules were used. One was based on that used in the flight simulator and the other was based upon a predicted schedule for level flight. For each individual case, the model was released from a stationary position of 0° roll angle at each α and the resulting model motion recorded. The results of these tests showed some very interesting aerodynamic phenomenon occurring with the model. The results of the model motion experiments for the two canard schedules are presented in Fig. 81.

As can be noted from the graphs in Fig. 81, a variety of rolling motions occur in the α range of $30\text{--}55^\circ$ for both canard schedules. As the angle of attack is increased, the first phenomenon encountered is wing rock. As with other aircraft, the wing rock encountered on the X-31 is not very smooth during its limit-cycle build-up or its maximum roll angle oscillations, as shown in Fig. 82. In addition, it should be noted that the values of peak-to-peak wing rock amplitude, $|\phi|$, are different for both canard scheduling cases at $\alpha = 32^\circ$ in



Fig. 80. X-31 aircraft (www.allstar.fiu.edu/aero/gallery2.htm).

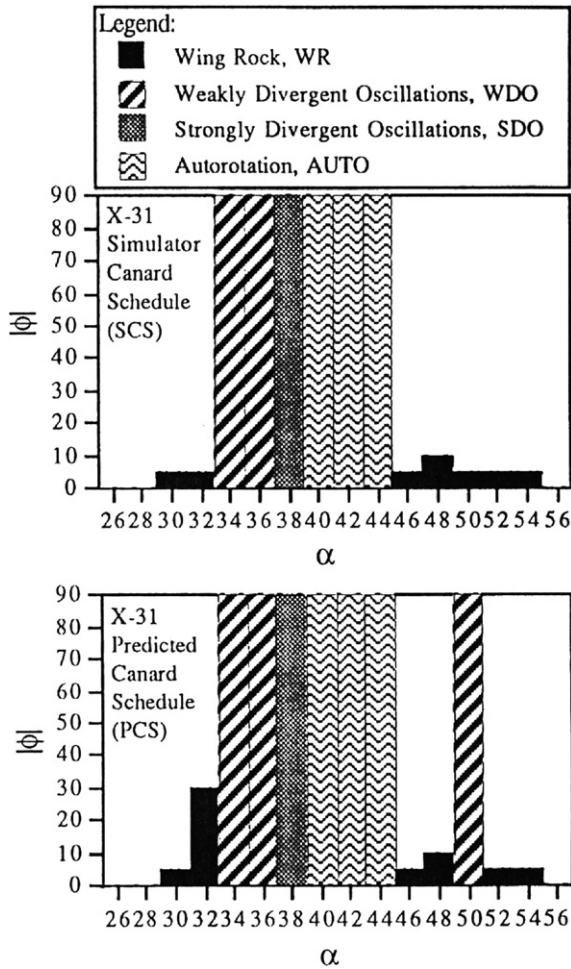


Fig. 81. Self-induced oscillation type and maximum amplitude vs. angle of attack for X-31 subscale model free-to-roll tests for both canard schedules [158].

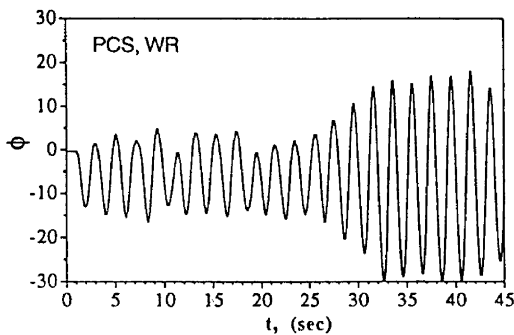


Fig. 82. Wing rock motion of subscale X-31 model for $\alpha = 32^\circ$ and $\theta_c = -39^\circ$ [158].

Fig. 81. At this angle of attack, the wing rock amplitude values differ by 25° ; however, the only difference between the two tests was a 7° difference in canard

stetting. It would appear that the canard position is an important factor in the aircraft’s behavior. Another unusual behavior found in X-31 wing rock is observed in Fig. 82. For some cases of wing rock, the model does not oscillate about a 0° roll angle. An offset bias of the wing rock motion is observed in these cases. Both positive and negative offsets were recorded, as was seen with double-delta wings.

As the angle of attack continues to increase, three new types of motion occur. Additionally, each of these motions lead to a roll divergence of the aircraft. Between α of 34° and 36° , a motion occurs that has been termed a weakly divergent oscillation. This motion is characterized by a long, slow oscillation build-up period that eventually leads to a roll divergence of the aircraft, as illustrated in Fig. 83. In examining Fig. 83, the long gradual build-up can be observed from 0 to approximately 11.5 s. Near 11.5 s, the model diverges near $\phi = -60^\circ$, and the aircraft continues its rolling motion into an inverted hung stall.

As α continues to increase, a motion termed a strongly divergent oscillation occurs near $\alpha = 38^\circ$. As opposed to the weakly divergent oscillation, this motion is characterized by a quick and violent oscillation build-up which rapidly leads to a roll divergence of the aircraft into an inverted hung stall. From Fig. 84, this quick roll divergence motion can be observed as the model’s oscillations quickly build between 0 and 4.5 s and diverges afterward into an inverted flight condition. The strongly divergent oscillation buildup to divergence occurs in most cases more than twice as fast as similar weakly divergent oscillation cases. In addition, this flight condition is not Reynolds number related since the stabilization of the X-31 configuration into an inverted hung stall has been reported from previous subscale drop model tests reported by Croom et al. [159].

The last type of divergent motion encountered, as α continues to increase, is a high incidence kinetic roll (HIKR) divergence motion, see Fig. 85. This motion is found in the α range of $40\text{--}44^\circ$ for both canard

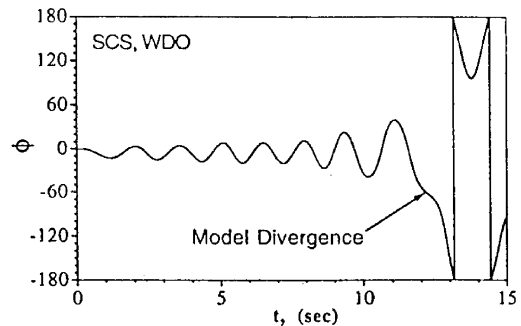


Fig. 83. Weakly divergent oscillations, WDO, on a subscale X-31 model for $\alpha = 34^\circ$ and $\theta_c = -34^\circ$ [158].

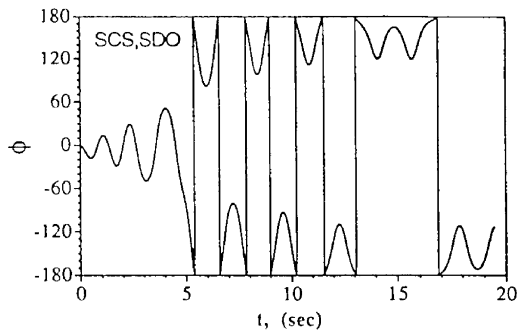


Fig. 84. Strongly divergent oscillations for the sub-scale X-31 model for $\alpha = 38^\circ$ and $\theta_c = 38^\circ$ [158].

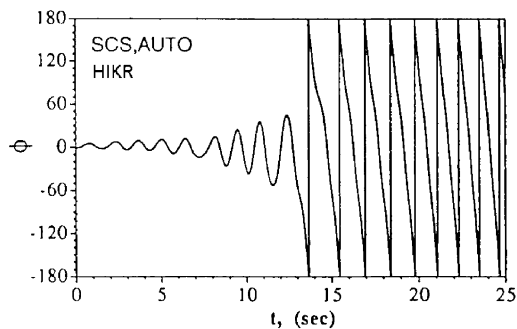


Fig. 85. HIKR autorotation of the sub-scale X-31 model for $\alpha = 44^\circ$ and $\theta_c = -44^\circ$ [158].

schedules. It is characterized by a roll oscillation build-up that diverges into an autorotating motion. Once in the autorotation mode, the vehicle continues to spin, in one roll direction only, while the angular velocity increases to some limiting value. This type of behavior has also been reported during the X-31 drop model tests reported by Croom et al. and a wind tunnel study by Villeta [160].

As α increases past 44° , the divergent motion ceases and small amplitude wing rock motions occur again. At 50° , a sole case of weakly divergent oscillation is found for the predicted canard schedule case. This is the greatest visible difference between the two oscillation envelopes presented in Fig. 81. Finally as α increases past 55° , the model becomes stable.

From this information several conclusions can be drawn. For the sub-scale X-31 model, a self-induced roll phenomenon envelope exists for the most part between 30° and 55° angle of attack with most of the activity being divergent motions. This is evident from Fig. 81 in which two different canard control settings produced somewhat similar activity over the same α range.

Within the range of 34 – 44° angle of attack, the motions of the model are all divergent. However, the

envelope is very well organized into three main regions of activity. Fig. 81 clearly shows that the model encounters weak divergent oscillation near 34 – 36° , then strong divergent oscillation near 38° , followed by autorotation modes from 40° to 44° . In addition, wing rock activity exists on either sides of this divergence envelope.

In an attempt to understand the flow mechanisms causing the different rolling motions, Williams and Nelson conducted a series of flow visualization tests to determine the vortical flow associated with each distinct dynamic phenomenon. To examine the flow field surrounding the forebody during each of the dynamic phenomena, smoke was introduced into the flow using either internal smoke ports in the model or by introducing smoke upstream of the model. The smoke helped in identifying two major flow structures in the forebody flow field. These were the primary forebody vortices, emanating from the primary separation lines, and vortices located at the canard–fuselage junction. The secondary vortices were identified; however, they were very minute and had no real effect on the forebody flow field.

Once the major flow structures were identified, the model was driven through a recorded free-to-roll time history using a motion control simulator [129]. In this experimental setup, the air bearing was replaced by a servo motor and computer control system. The free-to-roll time history data was downloaded to the motion control computer. The motion control system would then drive the servo motor to recreate the free to roll motion.

Additionally, off-surface flow visualization was used in conjunction with a laser light-sheet to examine the vortices at a particular fuselage position during the dynamic testing. This method was employed to identify the action of the vortices during each of the different roll phenomena. The laser light-sheet flow visualization experiments were videotaped; and later, the video tape was digitized, using software, to find the position of each vortex during the motion. Several positions along the forebody were examined; however, the most enlightening position was just aft of the canards. The results of these dynamic, off-surface, flow visualization experiments can be seen in Figs. 86–89. When inspecting these figures, keep in mind that the vortex position sketches are from the front of the model looking aft, and the triangular protrusions from the fuselage are the deflected canards of the model. In addition, these sketches are qualitative.

Fig. 86 shows the position of the primary forebody vortices and canard–fuselage junction vortices during a small amplitude wing rock episode taken from Fig. 82. As can be observed, from the vortex position at ~ 15.5 s, the flow visualization shows an interaction of the forebody and canard–fuselage junction vortices. At this

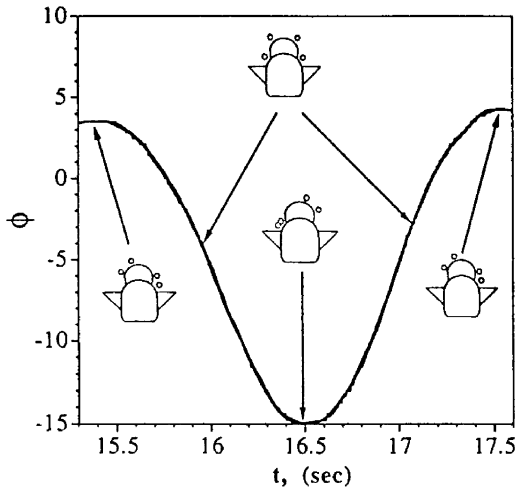


Fig. 86. Position of forebody and canard vortices through small wing rock motion, $\Delta\phi < 15^\circ$, ($\alpha = 32^\circ$, $\theta_c = -39^\circ$) [158].

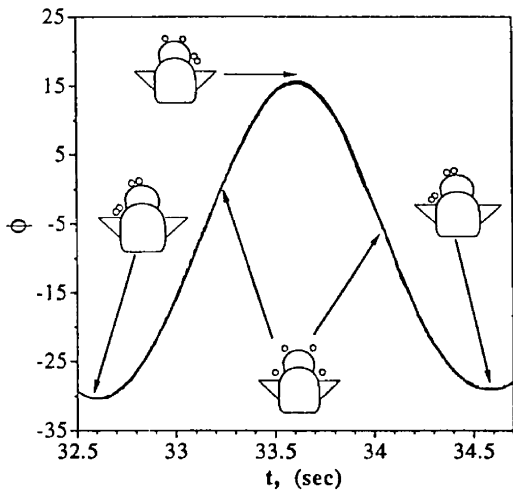


Fig. 87. Position of forebody and canard vortices through large wing rock motion, $\Delta\phi > 30^\circ$, ($\alpha = 32^\circ$, $\theta_c = -39^\circ$) [158].

roll angle, a pair of forebody and canard–fuselage junction vortices have joined and moved down toward their respective canard surface. At the same time, the other pair has moved up the canopy on the opposite side of the aircraft but stay separated.

As the model moves back to its neutral position ($\sim -5^\circ$), the vortices separate and become somewhat equally spaced around the canopy surface, ~ 16 s. As the motion continues, ~ 16.5 s, another forebody/canard–fuselage vortex interaction occurs on the opposite side of the canopy. As the model rolls back to its neutral position, ~ 17 s, the vortices separate and surround the canopy. This sequence of events repeats for each complete oscillation of the model. Thus, it

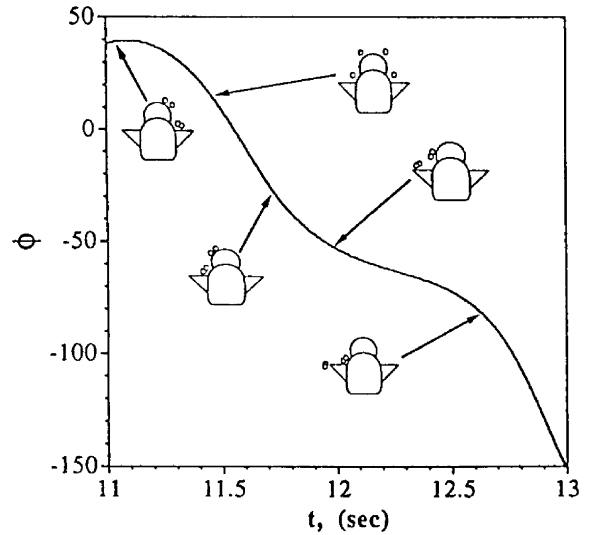


Fig. 88. Position of forebody and canard vortices into WDO motion, ($\alpha = 34^\circ$, $\theta_c = -34^\circ$) [158].

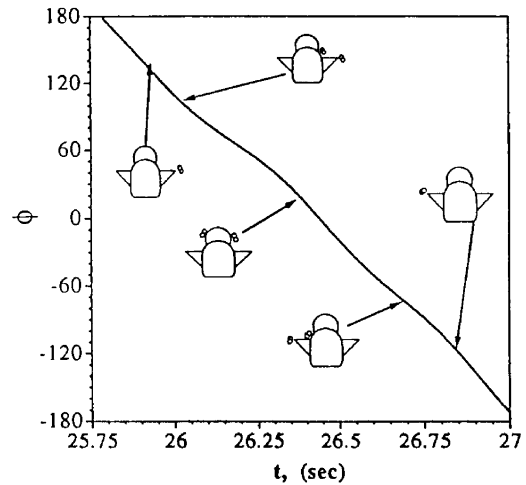


Fig. 89. Position of forebody and canard vortices for auto-rotation motion, ($\alpha = 44^\circ$, $\theta_c = -44^\circ$) [158].

seems that forebody vortex and canard–fuselage junction vortex interaction may be responsible for some of the oscillatory motion.

Fig. 87 shows the position of the primary forebody vortices and canard–fuselage junction vortices during a large amplitude wing rock episode taken from Fig. 82. The motion of the forebody and canard–fuselage junction vortices is very similar to that seen for the small amplitude wing rock case of Fig. 86, with one exception. For the large amplitude wing rock case, the opposite side vortices move over the canopy to interact with the other vortex pair. This can be seen in the

position of the vortices at ~ 32.5 s of Fig. 87 vs. the position of the vortices at ~ 16.5 s of Fig. 86. This movement of vortices across the top surface of the model is what separates large amplitude wing rock oscillations, $\Delta\phi > 30^\circ$, and small amplitude wing rock motions, $\Delta\phi \leq 15^\circ$.

Fig. 88 shows the position of the primary forebody vortices and canard–fuselage junction vortices during a weakly divergent oscillation episode, WDO, taken from Fig. 83. The vortex motion prior to the divergence is similar to that of Figs. 86 and 87. Once the model starts to diverge, however, there is a marked difference. From Fig. 88, the vortex position at ~ 11 s is similar to that of large wing rock motions. As the model rolls through its neutral position (0°), ~ 11.5 s, the vortices separate and move about the canopy. As the model rolls further, ~ 11.7 s, the vortices again pair and move over the top of the canopy. Instead of returning back to its neutral position, however, the model continues to roll and diverge. At ~ 12 s, one vortex pair has moved out behind the surface of the canard while the second pair has begun moving down toward the same canard surface. Thus, both pair are now acting solely on the same side of the model. As the model rolls further, ~ 12.6 s, one pair of vortices has moved behind the canard root.

In observing this interaction, it is not surprising that the model diverges. As the model rolls to $\phi = -60^\circ$, both sets of vortices move to one side of the aircraft. Thus they are both creating lift on one side of the model. This combined force may possibly be enough then to cause the model to diverge. This effect is increased as the model continues to roll since the vortex pairs move out further behind the surface of the canard, effectively changing the length of their respective moment arms. Thus when divergence occurs for the X-31 model, both sets of vortices move to the same side of the forebody.

Fig. 89 shows the position of the primary forebody vortices and canard–fuselage junction vortices during an autorotation episode taken from Fig. 85. At this point, the model has already diverged and is continuously rolling in one direction. As the model comes out of its inverted position, ~ 25.85 s, one vortex pair is visible behind the tip of the canard. The other vortex pair is hidden by the canard and does not appear until further rotation. At ~ 25.95 s, the first vortex pair has moved inboard behind the root of the canard, and the second pair has appeared behind the tip of the canard. As the model rolls to its neutral position (~ 0), the vortices have moved to either side of the canopy; but unlike the previous examples, the vortex pairs do not split apart into forebody and canard–fuselage junction vortices. Instead, they remain paired throughout the entire motion. As the model continues to roll, ~ 26.7 s, one vortex pair has moved behind the tip of the other canard, while the second pair has quickly slip across the

top of the canopy and moved behind the root of the same canard. The model continues to roll, ~ 26.8 s, while the first vortex pair moves under the canard surface and the second vortex pair moves from behind the tip of the canard. The model then again enters an inverted flight condition. It is interesting to note that as the vortices move across the aircraft, port side to the starboard side, the model continues to roll towards the left. This may be due to the poor roll damping characteristics of the aircraft coupled with both sets of vortices acting on the starboard side canard and/or wing at the largest negative roll angles.

From these observations, one common factor is found. That is the interaction of the primary forebody vortices and the canard–fuselage junction vortices. The interaction consists of the pairing of these vortices at the highest roll angles. In addition, the large scale wing rock and divergence occur when both sets of vortices move to one side of the aircraft. This is evident from the vortex motion in Figs. 87 and 88. Lastly, in the autorotation mode, the forebody and canard–fuselage junction vortices remain paired throughout the entire motion, and their action seems to help drive the motion. This indicates that the forebody and canard–fuselage junction vortices play principal roles in the self-induced oscillations of the subscale X-31 model.

4.3. Summary

For both the F-18 HARV and the X-31, the rolling characteristics were shown to be influenced by the interaction of the vortices created by the various airplane components. The interference of the forebody vortices and the leading-edge extensions LEX vortices appeared to be the driving mechanism for the F-18 HARV wing rock motion. When the wind tunnel nose section was removed, the wing rock motion stopped.

The X-31 drop model and wind tunnel free-to-roll experiments revealed some very interesting rolling dynamics. The HIKR motion first observed on the X-31 drop model was predicted by the subscale free-to-roll experiments. The subscale model experiments were found to predict wing rock for the F-18 HARV as well as the variety of rolling phenomena experienced on the X-31 drop model.

The difference in Reynolds numbers between the subscale model tests and the flight Reynolds numbers of the drop model or the aircraft were several orders of magnitude. The fact that the subscale test did so well is due to the fact that the motions were caused by the interaction of the separated vortical structure. As was shown earlier in this article, the leading-edge vortices created by highly swept wings are relatively insensitive to Reynolds number effects. However, this is not the case for forebody vortices. The separation line around the nose is definitely a function of the crossflow

Reynolds number. Although there are differences in the separation line between the subcritical and supercritical flows, the forebody vortices are very similar. If the tests were carried out in a facility where the crossflow Reynolds number for the forebody was in the transitional region, then the results would not have agreed. This is so because in the transition region, the forebody vortices would not exist in an organized manner as they are in both the sub and supercritical flow regimes. The point here is that subscale testing can provide insight into high angle-of-attack flight phenomena if care is taken to make sure the separated vortical flow field is similar to that which would occur at supercritical Reynolds numbers.

5. Nonlinear aerodynamic modeling

As was mentioned earlier, attempts have been made to predict the airloads acting on wings in the absence of vortex breakdown. With vortex breakdown present, predictions are more difficult. In the early 1960s, Tobak proposed a theoretical method for studying nonlinear problems in flight mechanics [161]. Tobak and his colleagues developed a nonlinear indicial response (NIR) method to represent the aerodynamic functions in the nonlinear regime [162,163]. The NIR method uses an aerodynamic response functional, based on the theory of functionals presented by Volterra [164], to describe the aerodynamic response to a step input of the motion variable. The response to an arbitrary motion is obtained by application of the convolution integral. Basically the method represents the aerodynamic response to an arbitrary input as a summation of responses to a series of step changes that approximate the input function.

5.1. Nonlinear indicial response model

The nonlinear indicial response method for the rolling moment response to an arbitrary input of the motion variable, the aircraft bank angle, is given below:

$$C_1(t) = C_1[\phi(\xi); t, 0] + \int_0^t C_{1\phi}[\phi(\xi); t, \tau] \frac{d\phi}{d\tau} d\tau, \quad (15)$$

where

$$C_{1\phi}[\phi(\xi); t, \tau] = \lim_{\Delta\phi \rightarrow 0} \frac{\Delta C_1[\phi(\xi); t, \tau]}{\Delta\phi} \quad (16)$$

is the indicial response functional. This form of the NIR method assumes that the rolling moment is differentiable for all possible motions. In other words, the indicial response must exist and be unique, which implies Fréchet differentiability [163]. Rennie and Jumper [165] used this method with relative success to evaluate

the unsteady lift on an airfoil under the influence of a moving trailing-edge flap.

Tobak and others have extended the NIR method to include aerodynamic bifurcations, or critical states. When an aerodynamic bifurcation occurs, the derivative ceases to exist. The modified NIR model is given below:

$$C_1(t) = C_1[\phi(\xi); t, 0] + \int_0^{t_{c.s.-\epsilon}} C_{1\phi}[\phi(\xi); t, \tau] \frac{d\phi}{d\tau} d\tau + \int_{t_{c.s.+\epsilon}}^t C_{1\phi}[\phi(\xi); t, \tau] \frac{d\phi}{d\tau} d\tau + \Delta C_1(t; \phi_{c.s.}), \quad (17)$$

where $\Delta C_1(t; \phi_{c.s.})$ is the aerodynamic transient that occurs when crossing a critical state. The major difficulty with the NIR method is in determining the aerodynamic response functionals and the transient aerodynamic term. This technique has been the subject of recent investigations [166,145,167]. Hsia and Jenkins [167] simplified Eq. (17) for the case of no critical state encounter during the motion. The model assumed that the motion $\phi(\xi)$ was analytic and could be represented by a Taylor series evaluated at τ , as was presented by Jenkins [168]. $C_{1\phi}[\phi(\xi); t, \tau]$ could then be replaced by $C_{1\phi}[\phi(\tau), \dot{\phi}(\tau), \ddot{\phi}(\tau), \dots, t, \tau]$. This led to

$$C_{1\phi} = C_{1\phi_{qs}} + A_0 + A_1\phi + A_2\phi^2 + \dots + B_1\phi\dot{\phi} + B_2\phi^2\dot{\phi} + B_3\phi\dot{\phi}^2 + \dots + C_1\phi\ddot{\phi} + C_2\phi^2\ddot{\phi} + C_3\phi\ddot{\phi}^2 + \dots + \dots, \quad (18)$$

where $C_{1\phi_{qs}}$ is the quasi-static rolling moment derivative with respect to roll angle. The coefficients in Eq. (18) are functions of the elapsed time $(t - \tau)$ and are evaluated using experimental roll data and performing a regression analysis to identify the dominant factors contributing to the response. Again, Eq. (18) is only valid when no critical states are encountered during the motion. If they are encountered, large transients show up in experimental data and the model fails to capture these transients. This comes from the fact that the dynamic rolling moment is not analytic in ϕ at critical states. When no critical states are encountered, the experimental results for C_1 and the NIR model are in good agreement. Figs. 90 and 91 show the dynamic roll moment predicted compared to experimental results with and without critical state encounter.

Myatt [169] and Reisenhel et al. [170] have successfully applied the NIR method to the study of simple delta wings undergoing a rolling motion. They were able to predict very complicated rolling motions using this method. Unfortunately, sophisticated dynamic wind tunnel experiments are required in order to determine the aerodynamic response functionals. This is because, at the present, there are no analytical methods available to provide the needed aerodynamic response functions. Dynamic wind tunnel experiments are generally

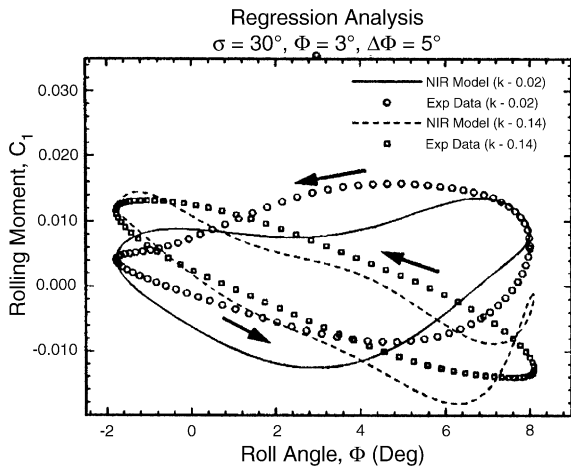


Fig. 90. Dynamic roll moment with critical state encounter [167].

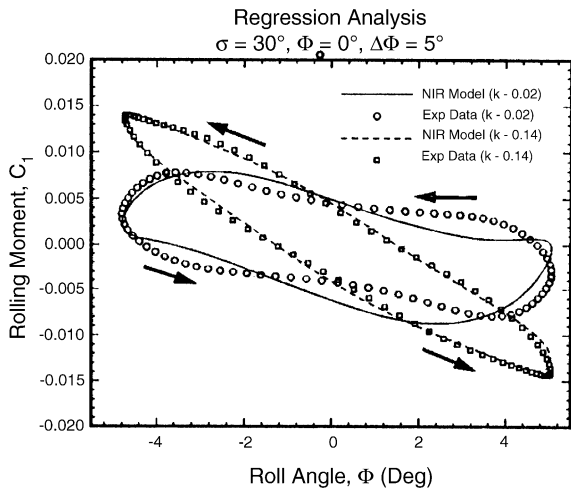


Fig. 91. Dynamic roll moment without critical state encounter [167].

impractical to perform in the development of new aircraft. The NIR method is an extremely powerful analytical tool, but it needs further development before it can be used effectively in the design of a new aircraft. Before any analytical predictions of the aerodynamic response can be made, a better understanding of the relationship between the aerodynamic functionals and the flow field is needed.

Although the NIR method is difficult to use, it does show the importance of critical states to nonlinear dynamics. The NIR method demonstrates that the source of complex nonlinear dynamic motions is related to the crossing of critical states, which cannot be taken into account with a locally linearized model [166]. The influence of critical state crossing was shown earlier. At

a critical state, it is believed that there is a change in the static flow topology over the model, which can create a change in the aerodynamics. During a dynamic maneuver, the flow field does not react fast enough to changes in the flow topology, which explains the lags and hysteresis in the dynamic data. It is obvious that the presence and location of critical states must be known in order to use the NIR method and be able to add transient terms when critical states are encountered.

5.2. Summary

The nonlinear indicial response technique is a promising tool in the study of nonlinear flight dynamics. Although it has been used successfully in the absence of critical state crossing, its application in the event of a critical state encounter is still under development, as it involves the determination of complicated response functions. This once again shows the importance of critical states in nonlinear aerodynamics.

6. Concluding remarks

In this review article, we have attempted to describe the flow structure above slender delta wings and highly swept-wing aircraft. A brief summary of the current understanding of leading-edge vortices and vortex breakdown is presented below.

The strength of the leading-edge vortices depends upon the angle of attack and the wing leading-edge sweep angle. For a given angle of attack, the strength decreases with increasing sweep angle. The circulation of slender delta wings can be scaled with the Hemsch and Luckring correlation parameter developed from slender body theory.

The velocity field associated with a leading-edge vortex can be characterized as the superposition of a jet flow and vortical flow. The maximum axial velocity occurs at the vortex center and can be as much as two or more times the freestream velocity. The extent of the jet-like flow (i.e., velocity greater than the freestream) can be as much as 30% of the local semi span. The maximum tangential velocity can reach approximately 1.5 times the freestream. The core (viscous subcore) defined by the distance between the peak tangential velocities is smaller than the jet core. The jet core increases in size with angle of attack while the subcore remains nearly constant in size over the wing.

The vorticity distribution through the leading-edge vortex is primarily in the axial direction prior to breakdown. Most of the axial vorticity is found within the viscous subcore. The radial and azimuthal vorticity components are small before breakdown. When spiral breakdown occurs, the core flow is deflected into a spiral geometry having the opposite sense of that of the

circulation. The axial vorticity is reduced substantially and a large negative azimuthal vorticity is present after breakdown. The large negative azimuthal vorticity is consistent with the requirement to sustain the vortex breakdown.

The pressure gradient along the vortex axis is a major factor in causing breakdown. The pressure gradient can be thought of as being created by the external flow and by a self-imposed component that is a function of the vortex strength.

The leading-edge vortices contribute a substantial portion of the lift generated by slender delta wings. The primary vortices produce large suction peaks on the upper surface pressure distribution prior to breakdown. After breakdown reaches the wing, the suction pressure peaks are reduced aft of the breakdown location. The modification of the pressure field affects the lift and moment characteristics of slender delta wings.

The aerodynamic characteristics of slender wings are modified during oscillatory or transient motions. For the large amplitude unsteady motions the aerodynamic forces and moments exhibit large overshoots and undershoots with respect to the static load measurements. The dynamic load measurements are functions of the reduced frequency and model motion. As the reduced frequency is increased, the aerodynamic hysteresis increases. The hysteretic behavior of the unsteady loads is a result of the lag in vortex breakdown due to the model's motion, or from a critical state encounter.

Although we have made much progress in understanding the flow structure of leading-edge vortices before and after breakdown, a comprehensive theory for breakdown still is unavailable. On the other hand, the experimental studies conducted during the past decade have provided details of the flow that may allow for the development of a new theoretical model or an improvement of one of the existing theories.

As illustrated in the review of the F-18 HARV and X-31 programs, the unsteady interaction of the separated vortical wake can create a variety of rolling motions. The interaction of the forebody and LEX vortices was the fluid mechanic mechanism causing the wing rock motion of the F-18 HARV at subsonic speeds. Similar interactions were also observed for the X-31 airplane. It is clear from these examples that a thorough understanding of the separated vortical flow is essential to predicting whether an aircraft might experience adverse rolling dynamics. As shown here, the use of scale model testing at subcritical Reynolds numbers can provide insight into the flows interactions that might occur at supercritical Reynolds numbers in high angle-of-attack testing.

Finally, we have briefly commented on the use of the nonlinear indicial response method to predict high angle-of-attack aerodynamic loads. Although a very promising approach, it is still very difficult to use; this is

particularly true for motions in which the aircraft crosses a critical state. The aerodynamic transient associated with crossing a critical state is at this time very difficult to model. However, with further research, the NIR method could become a valuable analysis tool for predicting high angle-of-attack dynamic phenomena.

Acknowledgements

Professor Nelson wishes to acknowledge the contributions to this article from the research work of Frank Payne, Ken Visser, Ken Iwanski, Scott Thompson, Andrew Arena Jr., Thomas Quast, Deborah Grismer, David Williams, Gregory Addington and his co-author Alain Pelletier. Their research and the many lively discussions we had on the topics of leading-edge vortices, breakdown and unsteady aerodynamics provided the foundation of this article.

References

- [1] Herbst WB. Future fighter technologies. *J Aircr* 1980; 17(8):561–6.
- [2] Orlik-Rückemann KJ. Aerodynamics of manoeuvring aircraft. *Can Aeronaut Space J* 1992;38(3):106–15.
- [3] Kalviste J. Aircraft stability characteristics at high angles of attack. AGARD-CP-235, Paper #29, 1978.
- [4] Evans C. An investigation of large amplitude wing-rock. *Aeronaut J* 1984;88(873):51–7.
- [5] Orlik-Rückemann KJ. Aerodynamic aspects of aircraft dynamics at high angles of attack. *J Aircr* 1983;20(9): 737–52.
- [6] Orlik-Rückemann KJ. Dynamic stability testing of aircraft—needs versus capabilities. *Prog Aerosp Sci* 1975; 16(4):431–47.
- [7] Brown CE, Michael Jr. WH. Effect of leading-edge separation on the lift of a delta wing. *J R Aeronaut Sci* 1954;21:690–706.
- [8] Hummel D, Srinivasan PS. Vortex breakdown effects on the low speed aerodynamic characteristics of slender delta wings in symmetrical flow. *J R Aeronaut Soc* 1967;71: 319–22.
- [9] Wentz WH. Wind tunnel investigations of vortex breakdown on slender sharp-edged wings. PhD thesis, University of Kansas, June 1968.
- [10] Wentz WH, Kohlman DL. Vortex breakdown on slender sharp edged wings. *J Aircr* 1971;8(3):319–22 (AIAA Paper #69-778 July 14–16, 1969).
- [11] McKernan JF. An investigation of the breakdown of leading edge vortices on a delta wing at high angles of attack. Master's thesis, University of Notre Dame, January 1983.
- [12] McKernan JF, Nelson RC. An investigation of the breakdown of leading edge vortices on a delta wing at high angles of attack. AIAA Paper #83-2114, August 1983.

- [13] Lan CE, Hsu CH. Effects of vortex breakdown on longitudinal and lateral-directional aerodynamics of slender wings by the suction analogy. AIAA Paper #82-1385, August 1982.
- [14] Bradley RG, Wray WO. A conceptual study of leading-edge-vortex enhancement by blowing. *J Aircr* 1973;11(1): 33–8.
- [15] Campbell JF. Augmentation of vortex lift by spanwise blowing. *J Aircr* 1976;13(9):727–32.
- [16] Er-El J, Seginer A. Effects of spanwise blowing on pressure distribution and leading-edge vortex stability. ICAS-86-2.5.1, 15th Congress of the International Council of the Aeronautical Sciences, London, September 1986.
- [17] Visser KD, Iwanski KP, Nelson RC, Ng TT. Control of leading-edge vortex breakdown by blowing. AIAA Paper #88-0504, January 1988.
- [18] Iwanski KP, Ng TT, Nelson RC. An experimental investigation of delta wing vortex flow with and without external jet blowing. AIAA Paper #89-0084, January 1989.
- [19] Magness C, Robinson O, Rockwell D. Control of leading-edge vortices on a delta wing. AIAA Paper #89-0999, March 1989.
- [20] Gu W, Robinson O, Rockwell D. Control of vortices on a delta wing by leading-edge injection. AIAA J 1976; 31(7):1177–86.
- [21] Mitchell A, Barberis D, Délery J. Oscillation of vortex breakdown location and its control by tangential blowing. AIAA Paper #98-2914, June 1998.
- [22] Mitchell AM, Molton P, Barberis D, Délery J. Control of vortex breakdown location by symmetric and asymmetric blowing. AIAA Paper #99-3652, June–July 1999.
- [23] Mitchell AM, Molton P, Barberis D, Délery J. Control of vortex breakdown location by symmetric and asymmetric blowing. AIAA Paper #99-3652, 1999.
- [24] Malcolm GN. Forebody vortex control. *Prog Aerosp Sci* 1991;28:171–234.
- [25] Malcolm GN, Ng TT. Forebody vortex manipulation for aerodynamic control of aircraft at high angles of attack. SAE Paper #892220, 1989.
- [26] Murri DG, Rao DM. Exploratory studies of actuated forebody strakes for yaw control at high angles of attack. AIAA Paper #87-2557-CP, 1987.
- [27] Malcolm GN, Ng TT, Lewis LL, Murri DG. Development of non-conventional control methods for high angle of attack flight using vortex manipulation. AIAA Paper #89-2192, 1989.
- [28] Brandon JM, Simon JM, Owens DB, Kiddy JS. Free-flight investigation of forebody blowing for stability and control. AIAA Paper #96-3444, July 1996.
- [29] Fisher DF, Murri DG, Lanser WR. Effect of actuated forebody strakes on the forebody aerodynamics of the NASA F-18 HARV. NASA TM-4774, October 1996.
- [30] Thompson JS, Fail RA, Inglesby JV. Low-speed wind-tunnel measurements of oscillatory lateral stability derivatives for a model of a slender aircraft (HP 115) including the effects of frequency parameter. Aeronautical Research Council, C.P. No. 1097, February 1969.
- [31] Ross AJ. Investigation of nonlinear motion experienced on a slender-wing research aircraft. *J Aircr* 1972;9(9):625–31.
- [32] AGARD Advisory Report No. 155A. Maneuver limitations of combat aircraft, 1979.
- [33] Anderson SB, Ernst EA, Van Dyke RD. Flight measurements of the wing-dropping tendency of a straight-wing jet airplane at high subsonic Mach numbers. NACA RM A51B28, 1951.
- [34] Chambers JR, Anglin EL, Bowman Jr JS. Effects of a pointed nose on spin characteristics of a fighter airplane model including correlation with theoretical calculations. NASA TN D-5921, 1970.
- [35] Chambers JR, Gilbert WP, Grafton SB. Results of recent NASA studies on spin resistance. Stall/spin problems of military aircraft. AGARD-CP-199, June 1976.
- [36] Coe Jr PL, Chambers JR, Letko W. Asymmetric lateral-directional characteristics of pointed bodies of revolution at high angles of attack. NASA TN D-7095, 1972.
- [37] Critical review of methods to predict the buffet capability of aircraft. Advisory Group for Aerospace Research and Development, Paris, France. AGARD-R-623, September 1974.
- [38] The effects of buffeting and other transonic phenomena on maneuvering combat aircraft. AGARD-AR-82, 1975.
- [39] Peckham DH. Low speed wind tunnel tests on a series of uncambered slender pointed wings with sharp edges. A.R.C., R&M. No. 3186, December 1958.
- [40] Earnshaw PB, Lawford JA. Low-speed wind tunnel experiments on a series of sharp-edged delta wings. A.R.C., R&M. No. 3424, March 1964.
- [41] Hummel D. Untersuchungen über das Aufplatzen der Wu bei an Schlanken Deltaflügeln. *Z Flugwiss* 1965;13.
- [42] Elle BJ. On the breakdown at high incidences of the leading edge vortices on delta wings. *J R Aeronaut Soc* 1960;64:491–3.
- [43] Harvey JK. Some observations of the vortex breakdown phenomena. *J Fluid Mech* 1962;14:585–92.
- [44] Lowson MV. Some experiments with vortex breakdown. *J R Aeronaut Soc* 1964;68:343–6.
- [45] Lambourne NC, Bryer DW. The bursting of leading edge vortices—some observations and discussion of the phenomena. A.R.C., R&M. No. 3282, April 1961.
- [46] Earnshaw PB. An experimental investigation of the structure of a leading edge vortex. RAE Tech Note No. Aero. 2740, March 1961.
- [47] Peckham DH, Atkinson SA. Preliminary results of low speed wind tunnel tests on a gothic wing of aspect ratio 1.0. A.R.C., CP-508, April 1957.
- [48] Chu J, Luckring JM. Experimental surface pressure data obtained on 65° delta wing across Reynolds number and Mach number ranges. NASA TM-4645, February 1996.
- [49] Perry A, Chong M. A description of eddying motions and flow patterns using critical-point concepts. *Annu Rev Fluid Mech* 1987;19:125–55.
- [50] Peake DJ, Tobak M. Three dimensional interactions and vortical flows with emphasis on high speeds. NASA TM-81169, AGARDograph No. 252, March 1980.
- [51] Délery J. Physique des Écoulements Tourbillonnaires. AGARD Symposium on Vortex Flow Aerodynamics, Scheveningen, The Netherlands, October 1990.
- [52] Délery J. Physics of vortical flows. *J Aircr* 1992;29(5): 856–76.

- [53] Payne FM. The structure of leading edge vortex flows including vortex breakdown. PhD dissertation, University of Notre Dame, May 1987.
- [54] Payne FM, Ng TT, Nelson RC, Schiff LB. Visualization and wake surveys of vortical flow over a delta wing. *AIAA J* 1988;26(2):137–43.
- [55] Menke M, Yang H, Gursul I. Experiments on the unsteady nature of vortex breakdown over delta wings. *Exp Fluids* 1999;27:262–72.
- [56] Pelletier A. An experimental investigation of vortex breakdown on slender delta-wing planforms. Master's thesis, University of Notre Dame, April 1994.
- [57] Pagan D, Solignac JL. Experimental study of the breakdown of a vortex generated by a delta wing. *Rech Aérosp* 1986;3:197–219.
- [58] Erickson GE. Vortex flow correlation. Tech Report AFWAL-TR-80-3143, 1980.
- [59] Lee MJ, Ho CM. Vortex dynamics of delta wings. In: *Frontiers in experimental fluid mechanics, Lecture Notes in Engineering*, vol. 46. Berlin: Springer, 1989. p. 365–427.
- [60] Détery J, Pagan D, Solignac JL. On the breakdown of the vortex induced by a delta wing. *Colloquium on Vortex Control and Breakdown Behavior*, Baden, Switzerland, ONERA TP 1987-105, April 6–7, 1987.
- [61] Brown GL, Lopez JM. Axisymmetric vortex breakdown part II: physical mechanisms. *J Fluid Mech* 1990;221:553–76.
- [62] Visser KD. An experimental analysis of critical factors involved in the breakdown process of leading edge vortex flows. PhD dissertation, University of Notre Dame, May 1991.
- [63] Visser KD, Nelson RC. Measurements of circulation and vorticity in the leading edge vortex of a delta wing. *AIAA J* 1993;31(1):104–11.
- [64] Nelson RC, Visser KD. Breaking down the delta wing vortex: the role of vorticity in the breakdown process. *AGARD Symposium on Vortex Flow Aerodynamics*, Scheveningen, The Netherlands, October 1–4, 1990.
- [65] Hemsch M, Luckring J. Connection between leading-edge sweep, vortex lift, and vortex strength for delta wings. *J Aircr* 1990;7(5):473–5.
- [66] Sychev VV. Three dimensional hypersonic gas flow past slender bodies at high angles of attack. *Prikl Mat Mech* 1960;24:205–12.
- [67] Wentz WH, MacMahon MC. Further experimental investigations of delta and double delta flowfields at low speeds. NASA CR-714, February 1967.
- [68] Smith JHB. Calculations of the flow over thick, conical, slender wings with leading edge separation. *A.R.C., R&M*. No. 3694, March 1971.
- [69] Leibovich S. The structure of vortex breakdown. *Annu Rev Fluid Mech* 1978;10:221–46.
- [70] Leibovich S. Vortex stability and breakdown. *AGARD-CP-342*, No. 23, April 1983.
- [71] Leibovich S. Vortex stability and breakdown: survey and extension. *AIAA J* 1984;22(9):1192–206.
- [72] Wedemeyer E. Vortex breakdown. *AGARD-LS-121*, No. 9, December 1982.
- [73] Benjamin TB. Some developments in the theory of vortex breakdown. *J Fluid Mech* 1967;28:65–84.
- [74] Hall MG. A theory for the core of a leading-edge vortex. *J Fluid Mech* 1961;11:209–28.
- [75] Hall MG. The structure of concentrated vortex cores. *Prog Aeronaut Sci* 1966;7:53–110.
- [76] Ludwig H. Ergänzung zu der Arbeit: stabilität der stromung in einem Zylindrischen Ringraum. *Z Flugwiss* 1961;9:359–61.
- [77] Ludwig H. Zur Erklärung der Instabilität der überangestellten Deltaflügeln abtretenden freien Wirbelkerne. *Z Flugwiss* 1962;10.
- [78] Détery JM. Aspects of vortex breakdown. *Prog Aerosp Sci* 1994;30:1–59.
- [79] Escudier MP, Keller JJ. Vortex breakdown: a two stage transition. *AGARD-CP-342*, No. 25, April 1983.
- [80] Sarpkaya T. On stationary and travelling vortex breakdowns. *J Fluid Mech* 1971;45:545–59.
- [81] Sarpkaya T. Vortex breakdown in swirling conical flows. *AIAA J* 1971;9:1792–9.
- [82] Sarpkaya T. Effect of the adverse pressure gradient on vortex breakdown. *AIAA J* 1974;12:602–7.
- [83] Escudier MP, Zehnder N. Vortex flow regimes. *J Fluid Mech* 1982;115:105–21.
- [84] Escudier MP, Bornstein J, Maxworthy T. The dynamics of confined vortices. *Proc R Soc* 1982;A382:335–60.
- [85] Faler JH, Leibovich S. Disrupted states of vortex flow and vortex breakdown. *Phys Fluids* 1977;20(9):1385–400.
- [86] Faler JH, Leibovich S. An experimental map of the internal structure of a vortex breakdown. *J Fluid Mech* 1977;86:313–35.
- [87] Sarpkaya T. Vortex breakdown and turbulence. *AIAA Paper #95-0433*, January 1995.
- [88] Malcolm GN. Impact of high- α aerodynamics of dynamic stability parameters of aircraft and missiles. *AGARD Lecture Series No. 114, Dynamic Stability Parameters*, 1981.
- [89] Kegelman JT, Roos FW. Effects of leading-edge shape and vortex burst on the flowfield of a 70-degree-sweep delta wing. *AIAA Paper #89-0086*, January 1989.
- [90] O'Neil PJ, Roos FW, Kegelman JT, Barnett RM, Hawk JD. Investigation of flow characteristics of a developed vortex. *Naval Air Development Center, Report No. NADC-89114-60*, 1989.
- [91] Jobe CE. Vortex breakdown location over 65° delta wings empiricism and experiment. *AIAA Paper #98-2526*, 1998.
- [92] Huang XZ, Hanff ES. Prediction of normal forces on a delta wing at high incidence. *AIAA Paper #93-3686*, August 1993.
- [93] Iwanski KP. An investigation of the vortex flow over a delta wing with and without external jet blowing. Master's thesis, University of Notre Dame, April 1988.
- [94] Ng TT, Nelson RC, Payne FM. Flow field surveys of leading edge vortex flows. *AGARD Symposium on Validation of Computational Fluid Dynamics*, Lisbon, Portugal, May 2–5, 1988.
- [95] Rockwell D, Özgoren M, Sahin B. Vortex-structure on a delta wing at angle-of-attack. *AIAA J* (in press).
- [96] Jumper EJ, Nelson RC, Cheung K. A simple criterion for vortex breakdown. *AIAA paper #93-0866*, January 1993.
- [97] Raat J. Vortex development and breakdown. *Technical Report AFFDL-TR-75-69*, Wright-Patterson AFB, OH, 1975.

- [98] Krause E, Althaus W. Vortex breakdown: mechanism of initiation and change of mode. IUTAM Symposium on Fluid Dynamics of High Angle of Attack, September 1992.
- [99] Hummel D. On the vortex formation over a slender wing at large angles of incidence. AGARD-CP-247, October 1978.
- [100] Polhamus EC. A concept of the vortex lift of sharp-edge delta wings based on a leading-edge suction analogy. NASA TN D-3767, December 1966.
- [101] Polhamus EC. Predictions of vortex-lift characteristics by a leading-edge suction analogy. *J Aircr* 1971;8(4):193–9.
- [102] Purvis JW. Analytical prediction of vortex lift. *J Aircr* 1981;18(4):225–30.
- [103] Huang XZ, Hanff ES, Jenkins JE, Addington G. Leading-edge vortex behavior on a 65° delta wing oscillating in roll. AIAA Paper #94-3507, 1994.
- [104] Huang XZ, Hanff ES. Prediction of leading-edge vortex breakdown on a delta wing oscillating in roll. AIAA Paper #92-2677, June 1992.
- [105] Huang XZ, Sun YZ, Hanff ES. Further investigations of leading-edge vortex breakdown over delta wings. AIAA Paper #97-2263, 1997.
- [106] Ericsson LE. Further analysis of fuselage effects on delta wing aerodynamics. AIAA Paper #2000-0981, 2000.
- [107] Stanbrook A, Squire LC. Possible types of flow at swept leading edges. *Aeronaut Q* 1964;15:72–82.
- [108] Miller DS, Wood RM. An investigation of wing leading edge vortices at supersonic speeds. AIAA Paper #83-1816, July 1983.
- [109] Donehoe SR. Vortex flow and vortex breakdown above a delta wing in high subsonic flow: an experimental investigation. PhD dissertation, Delft University of Technology, June 1996.
- [110] Stallings RL. Low aspect ratio wings at high angles of attack. In: *Progress in astronautics and aeronautics, tactical missile aerodynamics*, vol. 104. New York: AIAA, 1987 [chapter 3].
- [111] Rockwell D. Three dimensional flow structure on delta wings at high angle-of-attack: experimental concepts and issues. AIAA Paper #93-0550, January 1993.
- [112] Huang XZ, Hanff ES. Roll rate induced camber effect on delta wing leading-edge vortex breakdown. AIAA Paper #95-1793, June 1995.
- [113] Ericsson LE. Pitch rate effect on delta wing vortex breakdown. *J Aircr* 1996;33(3):639–42.
- [114] Ericsson LE. Difficulties in predicting vortex breakdown effects on a rolling delta wing. *J Aircr* 1996;33(3):477–84.
- [115] Ericsson LE. Effect of pitch rate on delta wing vortex characteristics AIAA Paper #96-3405, 1996.
- [116] Ericsson LE. Effect of angle of attack on roll characteristics of 65 deg delta wing. AIAA Paper #96-3443, 1996.
- [117] Ericsson LE. Nonlinear unsteady aerodynamics of pitching delta wings. AIAA Paper #98-2518, 1998.
- [118] Ashley H, Katz J, Jarrah MAM, Vaneck T. Unsteady aerodynamic loading of delta wings for low and high angles of attack. International Symposium on Nonsteady Fluid Dynamics, June 1990.
- [119] Bragg MB, Soltani MR. An experimental study of the effect of asymmetrical vortex bursting on a pitching delta wing. AIAA Paper #88-4334, August 1988.
- [120] Brandon JM, Shah GH. Effect of large amplitude pitching motions on the unsteady aerodynamic characteristics of flat-plate wings. AIAA Paper #88-4331, August 1988.
- [121] Jarrah M-AM. Unsteady aerodynamics of delta wings performing maneuvers to high angle of attack. PhD dissertation, Stanford University, December 1988.
- [122] Nelson RC, Thompson SA. Flow visualization of the leading edge vortices on slender wings undergoing large amplitude unsteady motions. Sixth International Symposium on Flow Visualization, Yokohama, Japan, October 1992.
- [123] LeMay SP, Batill SM, Nelson RC. Dynamics of leading edge vortices on pitching delta wing. *J Aircr* 1990; 27(2):131–8.
- [124] Thompson SA, Batill SM, Nelson RC. The separated flow field on a slender wing undergoing transient pitching motions. *J Aircr* 1991;28(8):489–95.
- [125] Thompson SA, Batill SM, Nelson RC. Unsteady surface pressure distributions on a delta wing undergoing large amplitude oscillations. AIAA Paper #90-0311, January 1990.
- [126] Thompson SA, Nelson RC, Batill SM. Delta wing surface pressures for high angle of attack maneuvers. AIAA Paper #90-2813, August 1990.
- [127] Thompson SA. The unsteady aerodynamics of a delta wing undergoing large amplitude motions. PhD dissertation, University of Notre Dame, May 1992.
- [128] Katz J. Wing/vortex interactions and wing rock. *Prog Aerosp Sci* 1999;35:727–50.
- [129] Arena Jr A. An experimental study of the nonlinear wing rock phenomenon. Master's thesis, University of Notre Dame, April 1990.
- [130] Arena Jr A. An experimental and computational investigation of slender wings undergoing wing rock. PhD dissertation, University of Notre Dame, April 1992.
- [131] Nguyen LT, Yip L, Chambers JR. Self-induced wing rock of slender delta wings. AIAA Paper #81-1883, August 1981.
- [132] Jun Y-W, Nelson RC. Leading-edge vortex dynamics on a slender oscillating wing. *J Aircr* 1988;25(9):815–9.
- [133] Konstadinopoulos P, Mook DT, Nayfeh AH. Subsonic wing rock of slender delta wings. *J Aircr* 1985;22(3): 223–8.
- [134] Ericsson LE. The fluid mechanics of slender wing rock. *J Aircr* 1984;21(5):322–8.
- [135] Arena Jr. AS, Nelson RC. Measurement of unsteady surface pressure on a slender wing undergoing a self-induced oscillation. *Exp Fluids* 1994;16(6):414–6.
- [136] Lee EM, Batina JT. Conical Euler methodology for unsteady vortical flows about rolling delta wings. AIAA Paper #91-0730, January 1991.
- [137] Legendre R. Écoulement au Voisinage de la Pointe Avant d'une Aile à Forte Flèche aux Incidences Moyennes. *Rech Aéronaut* 1952;(30):3–8.
- [138] Brown CE, Michael Jr WH. On slender delta wings with leading edge separation. NACA TN-3430, April 1955.
- [139] Mangler KW, Smith JHB. Calculation of the flow past slender delta wings with leading edge separation. RAE Report No. Aero. 2593, May 1957.

- [140] Arena Jr AS, Nelson RC. A discrete vortex model for predicting wing rock of slender wings. AIAA Paper #92-4497, August 1992.
- [141] Pelletier A. A study of the nonlinear aerodynamic characteristics of a slender double-delta wing in roll. PhD dissertation, University of Notre Dame, April 1998.
- [142] Pelletier A, Nelson RC. Dynamic behavior of an 80°/65° double-delta wing in roll. AIAA Paper #98-4353, August 1998.
- [143] Pelletier A, Nelson RC. The importance of critical states in nonlinear aerodynamics. AIAA Paper #2000-3909, August 2000.
- [144] Hanff ES, Ericsson LE. Multiple roll attractors of a delta wing at high incidence. AGARD-CP-494, 1990.
- [145] Myatt JH, Jenkins JE. A nonlinear indicial response model for the rolling 65-degree delta wing. AIAA Paper #96-3406-CP, 1996.
- [146] Ericsson LE. Flow physics of critical states for rolling delta wings. AIAA Paper #93-3683, 1993.
- [147] Fisher DF, Richwine DM, Banks DW. Surface flow visualization of separated flows on the forebody of an F-18 aircraft and wind-tunnel model. NASA TM-100436, 1988. Also published as AIAA #88-2112, 1988.
- [148] Fisher DF, Meyer Jr RR. Flow visualization techniques for flight research. NASA TM-100455, 1988. Also published in Flight Test Techniques, AGARD CP 452, Paper No. 20.
- [149] Fisher DF, Curry RE, Del Frate JH, Richwine DM. In-flight flow visualization techniques on a vortex-lift fighter aircraft. SAE 892222, Aerospace Technology Conference and Exhibition, 1989. Also published as NASA TM-4193, 1990.
- [150] Fisher DF, Del Frate JH, Richwine DM. In-flight flow visualization characteristics of the NASA F-18 High Alpha Research Vehicle at high angles of attack. Fifth International Symposium on Flow Visualization, Prague, Czechoslovakia, August 21–25, 1989.
- [151] Del Frate JH, Fisher DF, Zuniga FA. In-flight flow visualization with pressure measurements at low speeds on the NASA F-18 High Alpha Research Vehicle. AGARD Vortex Flow Aerodynamics Conference, Paper No. 13, October 1–4, 1990. Also published as NASA TM-101726, 1990.
- [152] Del Frate JH, Zuniga FA. In-flight flow field analysis on the NASA F-18 High Alpha Research Vehicle with comparisons to ground facility data. AIAA Paper #90-0231, 1990.
- [153] Fisher DF, Banks DW, Richwine DM. F-18 High Alpha Research Vehicle surface pressures: initial in-flight results and correlation with flow visualization and wind tunnel data. AIAA Paper # 90-3018, 1990. Also published as NASA TM-101724, 1990.
- [154] Quast T. A study of high alpha dynamics and flow visualization for a 2.5% model of the F-18 HARV undergoing wing rock. Master's thesis, University of Notre Dame, April 1991.
- [155] Quast T, Nelson RC, Fisher DF. A study of high alpha dynamics and flow visualization for a 2.5% model of the F-18 HARV undergoing wing rock. AIAA Paper #91-3267, September 1987.
- [156] Williams DL, Quast T, Nelson RC. Comparison of flight and sub-scale model wing rock characteristics of an F-18 aircraft. Final Report for NASA Grant NCA2-513, April, 1993.
- [157] Alcorn CW, Croom MA, Francis MS, Ross H. The X-31 aircraft: advances in aircraft agility and performance. Prog Aerosp Sci 1996;32:377–413.
- [158] Williams DL, Nelson RC, Fisher DF. An investigation of the X-31 roll characteristics at high angle-of-attack through subscale model testing. AIAA Paper #94-0806, January 1994.
- [159] Croon MA, Fratello DJ, Whipple RD, O'Rourke MJ, Trilling TW. Dynamic model testing of the X-31 configuration for high angle-of-attack flight dynamics research. AIAA Paper #93-3674, August 1993.
- [160] Viletta JR. Lateral-directional static and dynamic stability analysis at high angles-of-attack for the X-31 configuration. Master's thesis, The George Washington University, August 1992.
- [161] Tobak M, Pearson WE. A study of nonlinear longitudinal dynamic stability. NASA TR-R-209, September 1964.
- [162] Tobak M, Chapman GT. Nonlinear problems in flight dynamics involving aerodynamic bifurcations. AGARD CP 386, Paper 25, May 1985.
- [163] Tobak M, Chapman GT, nal A. Modeling aerodynamic discontinuities and onset of chaos in flight dynamical systems. *Extraits Ann Télécommun* 1987;42:300–14.
- [164] Volterra V. Theory of functionals and of integral and integro-differential equations. New York: Dover, 1959.
- [165] Rennie MR, Jumper EJ. Experimental measurements of dynamic control surface effectiveness. AIAA Paper #94-0504, January 1994.
- [166] Jenkins JE, Myatt JH, Hanff ES. Body-axis rolling motion critical states of a 65-degree delta wing. AIAA Paper #93-0621, January 1993.
- [167] Hsia AH, Jenkins JE. Simplified nonlinear indicial response models of a rolling 65 degree delta wing. AIAA Paper #94-3493, August 1994.
- [168] Jenkins JE. Simplification of nonlinear indicial response models: assessment for the two-dimensional airfoil case. *J Aircr* 1991;28(2):131–8.
- [169] Myatt JH. Modeling the roll moment on the 65-degree delta wing for rolling motions at high angles of attack. PhD dissertation, Stanford University, April 1997.
- [170] Reisenhelt P, Bettencourt M, Myatt J, Grismer D. A nonlinear indicial prediction for unsteady aerodynamic modelling. AIAA Paper #98-4350, August 1998.